



Durham E-Theses

Strontium isotope variations in the early solar system revealed by calcium-aluminium inclusions (CAIs) and ureilites

ROBINSON, LEWIS, WILLIAM

How to cite:

ROBINSON, LEWIS, WILLIAM (2023) *Strontium isotope variations in the early solar system revealed by calcium-aluminium inclusions (CAIs) and ureilites*, Durham theses, Durham University. Available at Durham E-Theses Online: <http://etheses.dur.ac.uk/14888/>

Use policy

The full-text may be used and/or reproduced, and given to third parties in any format or medium, without prior permission or charge, for personal research or study, educational, or not-for-profit purposes provided that:

- a full bibliographic reference is made to the original source
- a [link](#) is made to the metadata record in Durham E-Theses
- the full-text is not changed in any way

The full-text must not be sold in any format or medium without the formal permission of the copyright holders.

Please consult the [full Durham E-Theses policy](#) for further details.

**Strontium isotope variations in the early solar
system revealed by calcium-aluminium
inclusions (CAIs) and ureilites**

Lewis William Robinson

Department of Earth Sciences, Durham University

2022

This dissertation is submitted in fulfilment of the
requirements for the degree Masters by Research in
Geological Sciences.

Abstract

Isotope variations attributed to nucleosynthetic heterogeneities are preserved in different solar system materials (meteorites and planets) and provide insights into the origin of the elements, and the formation and evolution of the protoplanetary disk. Strontium isotopes are potentially highly sensitive to such nucleosynthetic variations. The three most abundant strontium isotopes ^{86}Sr , ^{87}Sr , and ^{88}Sr are produced by the s- and r-processes nucleosynthesis, in common stellar environments. In contrast, the lightest isotope, ^{84}Sr , is only produced by the p-process, and requires extreme conditions facilitating either proton-capture or photodisintegration. This study presents high-precision Sr isotope data for a range of early solar system materials, including twelve fine- and coarse-grained calcium-aluminium inclusions (CAIs) (considered the first solid material to have condensed in the solar system) separated from Allende (a CV3 meteorite), and fourteen ureilites (differentiated ultramafic meteorites, though to represent residual mantle material from which silicate and metallic melts have been removed).

Nearly all CAIs possess $\mu^{84}\text{Sr}$ excesses (measured $^{84}\text{Sr}/^{86}\text{Sr}$ relative to terrestrial standards), coarse-grained CAIs show variable $\mu^{84}\text{Sr}$, ranging from terrestrial values up to $+679 \pm 113\text{ppm}$, whereas fine-grained CAIs show a narrower range with a mean of $+68 \pm 43\text{ppm}$. Fine-grained CAIs possess relatively radiogenic $^{87}\text{Sr}/^{86}\text{Sr}$ isotope compositions suggesting that the initial $\mu^{84}\text{Sr}$ variability may have been lost due to open-system behaviour subsequent to their formation. Stable isotope $\delta^{84/86}\text{Sr}$ and $\delta^{88/86}\text{Sr}$ compositions largely lie to the right of the terrestrial Mass Dependent Fractionation Line (MDFL) consistent with previous studies, although the data here indicate that fine-grained CAIs generally possess light $\delta^{88/86}\text{Sr}$ and coarse-grained heavy $\delta^{88/86}\text{Sr}$. Overall, the $\mu^{84}\text{Sr}$ data taken with the $\delta^{84/86}\text{Sr}$ and $\delta^{88/86}\text{Sr}$ variations suggest the presence of excess ^{84}Sr , attributable to p-process nucleosynthesis.

In contrast, many ureilites (both main group and polymict ureilites) possess $\mu^{84}\text{Sr}$ deficits, with a mean value of $-101.6 \pm 69\text{ppm}$ (2.s.d, $n = 8$), while others possess terrestrial values. The $\delta^{84/86}\text{Sr}$ and $\delta^{88/86}\text{Sr}$ isotope compositions of the ureilites yield a slope of -1.206 ± 0.013 (2 s.e.), that is not easily explained by mass dependent fractionation, but rather by mixing between terrestrial like Sr and material with a low $\delta^{84/86}\text{Sr}$. Pre-solar SiC grains possess a low $\delta^{84/86}\text{Sr}$ composition consistent with such s-process enrichment. The broad covariation of $\delta^{88/86}\text{Sr}$ with Sr concentration may be due to stable isotope fractionation accompanying melt depletion, where in turn at low Sr concentrations the composition of refractory SiC grains dominates the bulk meteorite, yielding the observed variations in $\delta^{84/86}\text{Sr}$ - $\delta^{88/86}\text{Sr}$ space

Overall, the Sr isotope variations seen in CAIs are consistent with the Sr isotope compositions observed in many carbonaceous chondrites taken as a signature of material in the outer solar system (Charlier et al., 2017). Whereas the ureilites appear to possess a signature consistent with s-process enrichment, in accord with Nd, Mo and Os isotope anomalies (e.g., Burkhardt et al., 2019; Spitzer et al., 2020; Goderis et al., 2015) taken to indicate the presence of s-process enriched material in the inner solar system.

Table of Contents

<u>1. Introduction</u>	4
<u>2. Background on meteorites</u>	9
2.1 Meteorite classes.....	9
2.1.1 Non-carbonaceous meteorites.....	9
2.1.2 Carbonaceous meteorites.....	11
2.2 Principal meteorite components.....	13
2.2.1 CAIs.....	13
2.2.2 AOAs.....	14
2.2.3 Chondrules.....	14
2.2.4 Presolar SiC grains.....	15
2.2.5 Matrix.....	16
<u>3. Samples and analytical methods</u>	17
3.1 Samples.....	17
3.2 ICP-MS.....	17
3.3 Strontium isotope measurements.....	18
<u>4. Early solar system materials- CAIs and chondrules from the meteorite Allende</u>	20
4.1 Background on early solar system materials and Allende.....	20
4.1.1 The origins of CAIs.....	20
4.1.2 Allende.....	21
4.2 Sample preparations and methods.....	21
4.3 Results.....	22
4.3.1 Rare earth elements.....	22
4.3.2 Isotopic data.....	23
4.3.2.1 Internally normalised $\mu^{84}\text{Sr}$ data.....	23
4.3.2.2 Internally normalized $^{87}\text{Sr}/^{86}\text{Sr}$ and $^{87}\text{Rb}/^{86}\text{Sr}$ data.....	26
4.3.2.3 Stable Sr isotope data ($\delta^{88}\text{Sr}$ and $\delta^{84}\text{Sr}$).....	27
4.4 Discussion.....	28
4.4.1 Nucleosynthetic anomalies in ^{84}Sr	28
4.4.2 ^{87}Rb - ^{87}Sr isotope systematics.....	29
4.4.3 Stable Sr isotope variations.....	33
4.4.4 Ambiguity of p- versus r-/s-process anomalies in bulk CAIs.....	36
4.4.5 Fine-grained versus coarse-grained CAIs.....	36
4.5 Conclusions.....	37
<u>5. Ureilites and their Sr isotope evolution</u>	39
5.1 An introduction to Ureilites.....	39
5.1.1 Ureilite petrography.....	39

5.1.2 Ureilite chemistry.....	40
5.1.3 The ureilite parent body (UPB) and ureilite daughter bodies (UDBs).....	40
5.1.4 Nucleosynthetic variations in ureilites.....	42
5.2 Sample preparation and methods.....	43
5.2.1 Trace element and isotopic analyses.....	44
5.3 Results.....	44
5.3.1 Trace and rare earth elements.....	44
5.3.2 Isotopic data.....	46
5.3.2.1 Internally normalised $\mu^{84}\text{Sr}$ data.....	46
5.3.2.2 Stable Sr isotope data ($\delta^{88}\text{Sr}$ and $\delta^{84}\text{Sr}$).....	46
5.3.2.3 Internally normalized $^{87}\text{Sr}/^{86}\text{Sr}$ and $^{87}\text{Rb}/^{86}\text{Sr}$ data.....	49
5.4. Discussion.....	50
5.4.1 Rare earth element and trace element systematics in ureilites.....	50
5.4.2 Nucleosynthetic anomalies in ^{84}Sr	51
5.4.3 Stable Sr isotope variations.....	53
5.4.4 Ureilite Rb-Sr isotope systematics.....	56
5.4.5 Mineralogical controls on Sr isotope compositions in ureilites.....	58
5.4.6 s- or p-process origin for $\mu^{84}\text{Sr}$ distributions in ureilites.....	60
5.4.7 An updated model of the UPB and early protoplanetary disk dynamics.....	61
5.5. Conclusions.....	64
6. Summary	66
7. References	70

Acknowledgements

I would like to thank my supervisor Professor Kevin Burton for both for his invaluable insights with this project and all his continuing support during my early career, I would also like to thank Dr Geoffrey Nowell and Dr Chris Ottley for their assistance with laboratory work and data collection and Dr Ian Parkinson for his assistance in modelling and for valuable discussions on the project. Finally, I would like to thank Sam F, Rachel S and Joe C for keeping me sane over the unique times of the past year and a half and putting up with my own brand of uniqueness, Annabelle F for being a wonderful desk neighbour and Rob P for supporting me throughout my early schooling and encouraging me to pursue a career in science.

1. Introduction

The prevailing view for the origin of our solar system is that the gravitational collapse of a molecular cloud rich in gases and presolar dust, thought to originate from diverse stellar environments, including asymptotic giant-branch (AGB) stars and supernovae resulted in the formation of a protoplanetary disk. Though previously believed to be homogenous due to presolar grain mixing and destruction via various physical processes (e.g., Klessen, 2011), the prevailing canonical view that this molecular cloud was both spatially and chemically heterogenous (e.g., Kööp et al., 2016; Nanne et al., 2019; Burkhardt et al., 2019). Pre-existing heterogeneities in the cloud are important in developing chemically distinct reservoirs during early solar system formation and subsequent protoplanetary disk evolution. Indeed, mixing between at least two early reservoirs is believed to have resulted in the observed isotopic dichotomy between non-carbonaceous (NC) and carbonaceous (CC) meteorites (Warren, 2011; Kleine et al., 2020; Charlier et al., 2017; Fukai and Yokoyama, 2019; Budde et al., 2016). The NC-CC dichotomy encompasses most known meteorite classes as evidenced by isotopic variations in a number of elements including Ti, Cr (Warren, 2011; Trinquier et al. 2009), Ni (Nanne et al., 2019; Tang and Dauphas, 2012), Nd (Saji et al., 2020), Mo (Budde et al., 2016) and Sr (Charlier et al., 2017).

The NC and CC reservoirs were previously believed to have developed through thermal processing of the protoplanetary disk (e.g., Paton et al., 2013; Poole et al., 2017). However, to explain the observed isotopic and geochemical diversity in known meteorites, labile presolar component removal from the disk would have to occur in a range of different material carriers. Such a scenario is viewed as improbable as the thermal stability of these material carriers would depend on the nature of the carriers themselves and not the stellar environment in which the thermal processing occurs (Kleine et al., 2020). Therefore, thermal processing is unlikely to solely account for the observed NC-CC dichotomy as a meteorites bulk chemistry appears intrinsically linked to the region from which their parent body accreted within the protoplanetary disk (e.g., Nanne et al., 2019; Burkhardt et al., 2019; Tenner et al., 2019). The current prevailing hypothesis for the development of the NC and CC reservoirs suggests that the two coevolved together in the early protoplanetary disk, before becoming spatially separated post-condensation of Calcium-Aluminium-rich inclusions (CAIs), preventing further mixing until after planetesimal formation was well underway (Figure 1; Nanne et al., 2019; Kleine et al., 2020; Charlier et al., 2019), probably during the time of the Grand Tack (e.g., Walsh et al., 2011) or the later stages of gas giant accretion (e.g., O'Brien et al., 2018). The spatial separation of the two reservoirs, and in parallel the divide between the inner and outer disk, is often attributed to the accretion of proto-Jupiter (Kruijjer et al., 2017; Desch et al., 2018; Burkhardt et al., 2019; Nanne et al., 2019) and/or an associated pressure barrier (Brasser and Mojzsis, 2020; Desch et al., 2018; Morbidelli et al., 2016), which appears to have restricted inward drift of outer disk materials, while limiting but not completely halting the outward drift of inner disk materials (e.g., Williams et al., 2020).

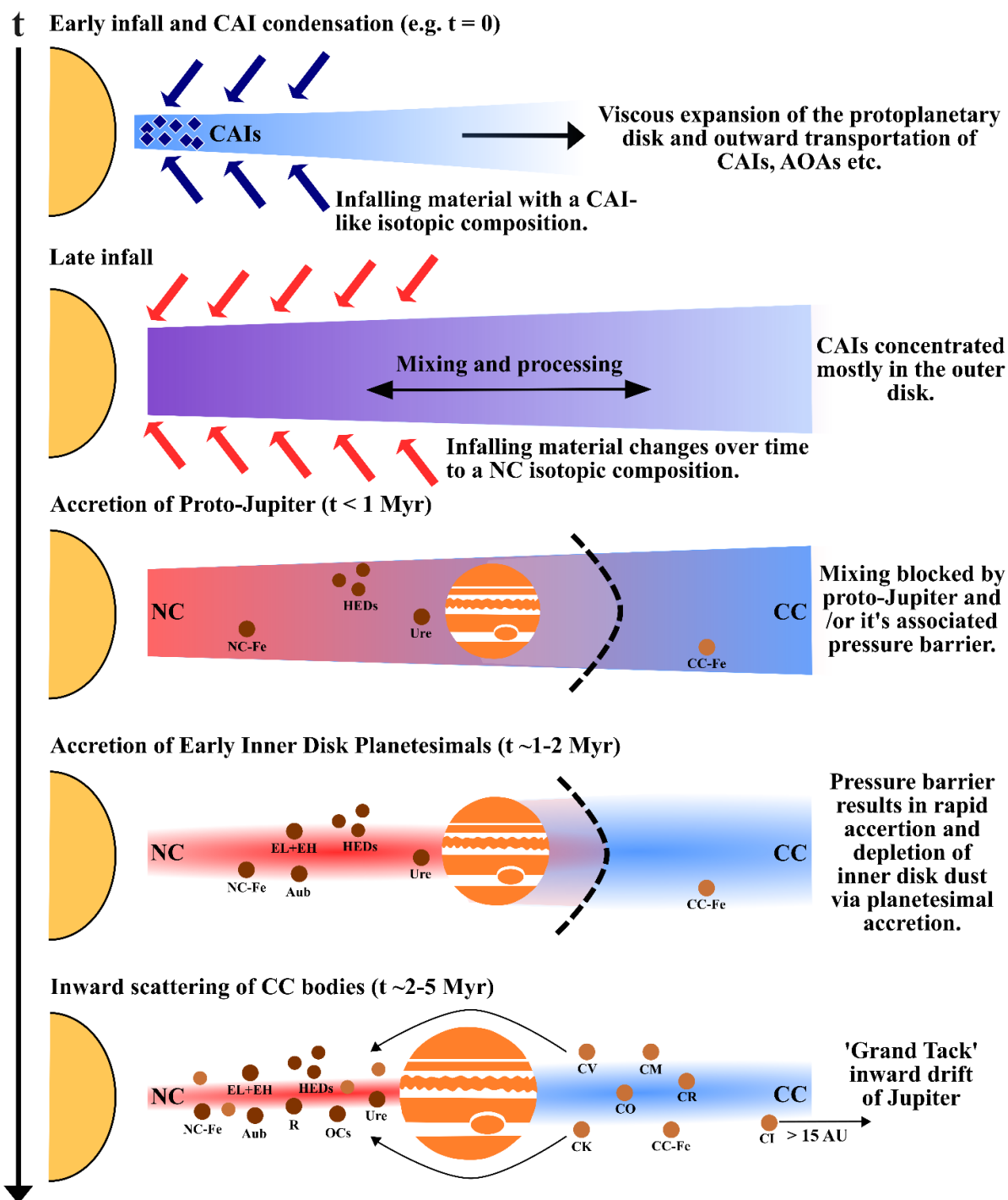


Figure 1- A simplified schematic model for early solar system evolution resulting in the formation of the NC and CC reservoirs. N.B. not to scale. The rapid infall of proto-molecular cloud materials formed a protoplanetary disk that initially possessed a CAI-like isotopic signature, which became more NC-like as infalling material compositions changed during late infall, particularly in the inner disk. A degree of mixing occurred between the inner and outer disk, but complete homogenisation was prevented by the proto-Jupiter's rapid accretion, which essentially spatially separated the two leading to the development of the NC and CC reservoirs. Planetesimal temporal appearance is based on previously collated model accretion ages (Desch et al., 2018). Figure adapted from Nanne et al. (2019), Burkhardt et al. (2019) and Kleine et al. (2020).

The principal planetesimal building materials present in the protoplanetary disk during the development of NC-CC reservoirs and at the time of their separation were CAIs (predominately normal but also FUN (fractionated and unidentified nuclear effects)-type and PLAC (platy hibonite crystal)-like CAIs; for an overview see Dauphas and Schauble, 2016), ameboid olivine aggregates (AOAs), chondrules and finer

nebula/planetesimal derived dust. These materials have been extensively studied and resultingly have well defined major element, trace element and isotope characteristics (e.g., Charlier et al., 2019; Park et al., 2017; Williams et al., 2020; Schrader et al., 2020). Chemical evidence from CAIs and chondrules suggests that the proto-Jupiter barrier was not totally effective in separating the NC and CC reservoirs and that some outer disk materials (typically <100 μm in size; Weber et al., 2018; Haugbølle et al., 2019) were able to drift inwards, affecting inner disk chemistry (Spitzer et al., 2020; Pignatale et al., 2019). Accordingly, some NC meteorites are known to possess similar isotopic/chemical signatures to CC meteorites (e.g., Spitzer et al., 2020), though in part these chemical similarities can also be attributed to parent body accretion at times when CAIs and outward drifting CC-like dust were still relatively abundant in the inner disk i.e., before inner/outer disk separation by proto-Jupiter (e.g., Desch et al., 2018; Spitzer et al., 2020). For example, ureilites, whilst isotopically thought to be an inner disk product and classified as a NC achondrite group, have often been described as having a chemical link to CC meteorites (Warren, 2011; Budde et al., 2017; Goodrich et al., 2015), specifically CV chondrites (Greenwood et al., 2017; Rankenburg et al., 2007). Explaining the origins of these geochemical signatures provides valuable insights into early solar system evolution, however, current interpretations are somewhat inhibited by the poorly constrained histories of early formed planetesimals, the nucleosynthetic origins of the materials they initially accreted from and the exact timing of their accretion. Strontium isotopes are well suited to addressing some of these problems and improving on existing models for the chemical evolution of the early solar system.

Strontium is a refractory lithophile element with four naturally occurring stable isotopes: ^{84}Sr (0.56%), ^{86}Sr (9.86%), ^{87}Sr (7.00%) and ^{88}Sr (82.58%). These four isotopes have distinct nucleosynthetic origins; therefore, Sr isotopic variations can help to identify the nucleosynthetic heritage of early solar system material and provide constraints on the genetic relationships between planetesimals and meteorites (Dauphas and Schauble, 2016). Crucial, in this regard is ^{84}Sr , a p-process nuclide with likely origins in type II (core collapse; Rauscher et al., 2002) or Ia (Travaglio et al., 2018) supernovae. The other three Sr isotopes are produced by two slow neutron capture processes (s-process) and the rapid neutron capture process (r-process). The two relevant s-process pathways to ^{86}Sr , ^{87}Sr and ^{88}Sr nucleosynthesis are the main s-process nucleosynthesis (accounting for 60% of all ^{86}Sr and ^{87}Sr and 70% of all ^{88}Sr produced; Lugaro et al., 2003), that occurs in AGB stars (e.g., Bisterzo et al., 2014), and the weak s-process, that takes place in massive stars (e.g., Pignatari et al., 2010). Around 30% of ^{88}Sr is also produced via the r-process in supernovae or by neutron star mergers. The production of ^{87}Sr through the radioactive β -decay of ^{87}Rb ($T_{1/2} = 49.624$ Gyr; Rotenberg et al., 2012) is also notable, as ^{87}Rb decay products typically dominate over possible nucleosynthetic and/or mass dependent variations in ^{87}Sr abundances. Therefore, the ^{87}Rb - ^{87}Sr parent-daughter isotope system has widespread utility, being used in terrestrial and meteoritic geochronology and has provided key constraints on early solar system processes, for example, the timing of volatile element depletion due to the differences in volatility between Rb and Sr (e.g., Papanastassiou and Wasserburg, 1969; Moynier et al., 2012).

Much work has already been done on the Sr isotope geochemistry of meteorites over the past several decades, initiated by pioneering double-spike ^{84}Sr and ^{88}Sr studies of Allende, CAIs and chondrules (Patchett, 1980a; 1980b). Bulk meteorite ^{84}Sr and $^{87}\text{Sr}/^{86}\text{Sr}$ ratios have been recorded to possess heterogeneities in a large number of chondrites, notably excluding carbonaceous CI chondrites, that correlate with mass-independent O isotope variations (e.g., Moynier et al., 2012). The observed heterogeneity in $^{87}\text{Sr}/^{86}\text{Sr}$ were initially suggested as having chronological significance however it was later proposed that the heterogeneities were instead the product of a heterogenous distribution of Sr isotopes in the early solar system (Moynier et al., 2012). Evidence from other isotope systems, e.g., Mo and W, also hinted at a heterogenous distribution of isotopes in the early solar system and lead to the proposal of the now widely accepted NC and CC reservoirs, which were separated by the formation of proto-Jupiter (e.g., Kruijer et al., 2017). Since the development of the proto-Jupiter hypothesis, abundant ^{84}Sr data has been collected for a wide variety of bulk meteorites and their constituent components providing further evidence for the existence of the NC and CC reservoirs (e.g., Charlier et al., 2017; Hans et al., 2013; Paton et al., 2013; Moynier et al., 2012; Fukai and Yokoyama, 2019; Myojo et al., 2018).

In recent years, there has been increasing interest in other stable Sr signatures in meteorites and their constituent phases after several studies reported resolvable ^{88}Sr fractionation in both terrestrial and extra-terrestrial materials (e.g., Charlier et al., 2012; Amsellem et al., 2018). Recent studies have shown that $^{88}\text{Sr}/^{86}\text{Sr}$ is a useful tool for studying magmatic and fluid conditions, as, unlike $^{87}\text{Sr}/^{86}\text{Sr}$, it can be fractionated in natural systems as a consequence of variations in redox conditions and ionic speciation (Charlier et al., 2012; Charlier et al., 2017; Amsellem et al., 2018; Klaver et al., 2020). Primarily, $^{88}\text{Sr}/^{86}\text{Sr}$ studies have focused on its use as a weathering tracer (e.g., Böhm et al., 2012; Wei et al., 2013) and in cosmochemistry (e.g., Charlier et al., 2017; Amsellem et al., 2018); though the use of stable Sr for these purposes relies on the assumptions that (1) the high-temperature fractionation of Sr isotopes is well-understood and (2) isotopic variations in weathering products are not the result of fraction. The fractionation behaviour of Sr is relatively well established with the degree of fraction known to be particularly sensitive to the presence of CO_3^{2-} and SO_4^{2-} (e.g., Böhm et al., 2012; Widanagamage et al., 2015). Fractionation is also known to occur in igneous systems during the precipitation of isotopically heavy plagioclase (Charlier et al., 2012).

Stable and radiogenic Sr studies have been crucial in advancing our understanding of the early solar system, however, arguably they have also been somewhat limited by the accuracy of data collection methods used (Henshall et al., 2018). With the exception of the pioneering work of Patchett et al. (1980a;1980b), many ^{88}Sr studies have used multicollector-inductively coupled plasma mass spectrometer (MC-ICP-MS) techniques, which allow for rapid measurements but at the expense of both precision (typically 30-70 ppm) and the simultaneous measurement of ^{84}Sr due to the low relative abundance of this isotope (e.g., Charlier et al., 2012). Thermal ionisation mass spectrometer (TIMS) measurements on the other hand provide more precise data (typically 10-20 ppm or better) and allow for the measurement of all Sr isotopes. Such TIMS measurements are not, however, without their own issues; specifically, the use of a static TIMS collection technique is

believed to potentially produce data inaccuracies as analytical artefacts may produce a spurious signal for ^{84}Sr (Henshall et al., 2017), with excess ^{84}Sr reported in many studies utilising static collection (e.g., Moynier et al., 2012). Multi-dynamic TIMS collection is believed to be more accurate (Henshall et al., 2017), however for ^{84}Sr measurements, the problem remains that it is never entirely clear whether any variation in ^{84}Sr is mass dependent or independent. These processes can only be resolved by obtaining high-precision data for both ^{84}Sr and ^{88}Sr from the same sample solution, which at present can only be achieved through a double-spike protocol as this helps eliminate much of the uncertainty associated with both static and multi-dynamic TIMS collection (Charlier et al., 2017).

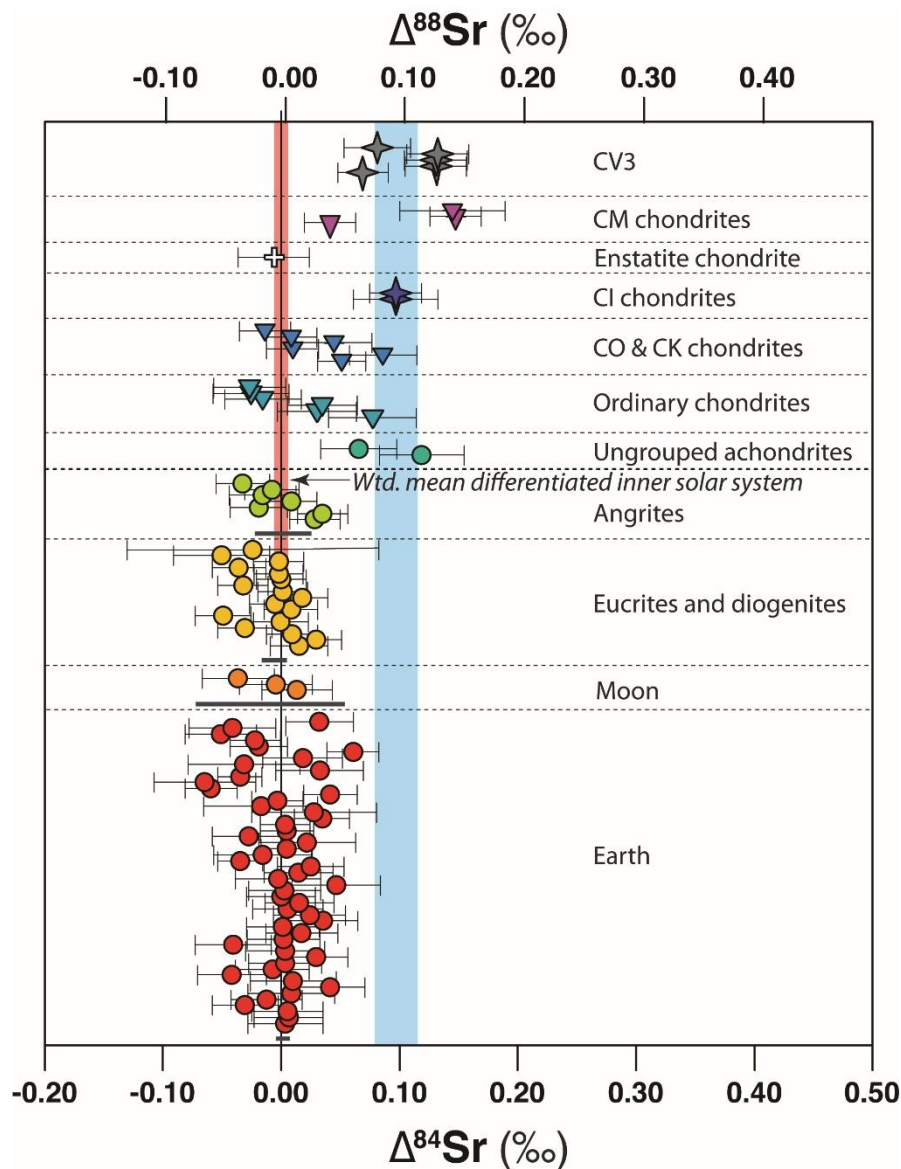


Figure 2- Plot of $\Delta^{84}\text{Sr}$ and $\Delta^{88}\text{Sr}$ for a previous dataset obtained by Charlier et al., 2017. The vertical pink line represents a weighted mean Sr value for the inner solar system (NC meteorites) and the vertical blue line represents a weighted mean for the outer solar system (CC meteorites). Credit to Charlier et al., 2017.

Few studies at present have utilised this method for Sr isotope analysis, however datasets have been obtained for many meteorite classes and CAIs (Figure 2; e.g., Charlier et al., 2017; Charlier et al., 2019). Measurements from these studies suggests a clear divide in stable Sr isotopes between the NC and CC reservoirs, with CAI Sr signatures found to be indistinguishable from most bulk CC meteorites (Charlier et al., 2017; Charlier et al., 2019). While relatively comprehensive, these current datasets lack high precision data on several key NC meteorite classes, including the ureilites. This study aims to resolve this gap in our observations and build upon previous work, by reporting high precision double-spike ^{84}Sr and ^{88}Sr data for a suite of ureilites CAIs and other meteorite materials. This data is used to improve our understanding of the early solar system in the first 5 Myr post CAI condensation, constraining the ureilite parent body's (UPB) evolution, geochemical origins, and its catastrophic destruction. The multi-isotope approach of this study also provides a window into the development of the NC reservoir during proto-Jupiter's accretion and the 'Grand Tack' (Walsh et al., 2011) helping refine our understanding of a key formative period during early solar system evolution.

2. Background on Meteorites

2.1 Meteorite classes

As mentioned previously, meteorites native to our solar system can be broadly divided into inner solar system (NC) and outer solar system (CC) groupings before being sub-divided into chondrite (‘primitive’ unmelted/undifferentiated parent bodies) and achondrite (melted/differentiated parent bodies) classes (Figure 3; Warren, 2011). Here the different types of NC-CC chondrites and achondrites and the principal components of these meteorites are briefly reviewed. Meteorites sampled on Earth are also divided into separate categories based on their acquisition history alongside their geochemical and petrographic classifications. Samples are divided into either ‘falls’, those meteorites whose fall and subsequent impact is observed with samples collected shortly thereafter minimising terrestrial contamination, and ‘finds’, meteorites that cannot be ascribed to a specific impact and whose provenance since arriving on Earth is unclear. A large proportion of meteorite samples accessible on Earth are ‘finds’ typically discovered by expeditions in Antarctica and the Sahara Desert.

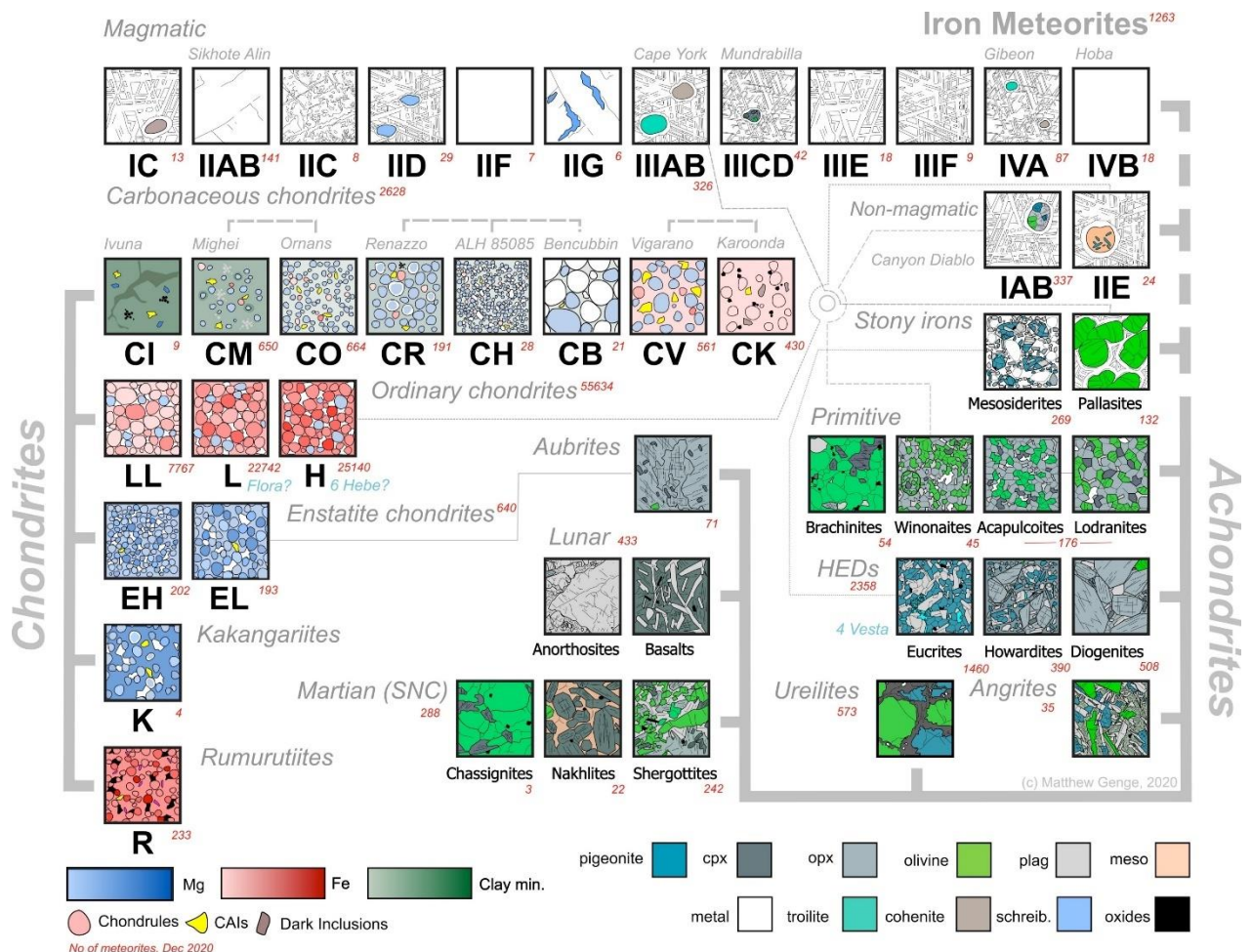


Figure 3- Taxonomy of the majority of common carbonaceous and non-carbonaceous chondrites and achondrites, including iron meteorites, pallasites and mesosiderites. (Credit to Genge, 2020).

Ordinary chondrites (OCs) are by far the most common type of NC chondrite sampled on Earth, accounting for 85% of all observed meteorite falls. The OCs are sub-divided into three groups (H, L and LL) based on compositional variations including bulk Fe contents. The three OC groups are considered to have derive from at least 3 different parent bodies, with the LL parent body originating closest to the Sun (e.g., Lucas et al., 2020); the OC parent bodies are believed to have accreted in the presence of H₂O at around 2.0-2.2 Myr post-CAI condensation (Desch et al., 2018), before being destroyed via catastrophic collision around ~60 Ma after their accretion (Blackburn et al., 2017). Enstatite chondrites (ECs) are a slightly older chondrite class believed to have accreted at around 1.7-1.9 Myr post-CAI condensation under extremely reducing conditions (Desch et al., 2018). This class of chondrites has two sub-groups (EH and EL), both dominated by reduced mineralogies and believed to have originated well within the snowline, essentially accreting no H₂O during formation (e.g., Defouilloy et al., 2016; Desch et al., 2018).

2.1.2 Non-Carbonaceous Achondrites

Howardite-Eucrite-Diogenites (HED) are the most common type of achondrite sampled on Earth and are well studied, particularly eucrites. The HED parent body is believed to be the large asteroid (4)Vesta (e.g., Drake, 2001) and is estimated to have accreted early at around 0.8 Myr post-CAI condensation (e.g., Desch et al., 2018). After HEDs, angrites are the next best sampled early solar system crust; the meteorites are believed to have crystallized from low-silica melts with high CaO (Mittlefehldt et al. 2002; Jambon et al. 2008) and very low volatile alkali contents under high fO_2 (e.g., Wadhwa, 2008). It is believed, based on early studies, that a refractory CAI-like component was involved in angrite formation (Prinz et al. 1988). Aubrites are a rarer achondrite class, geochemically related to ECs (e.g., Defouilloy et al., 2016), that are mineralogically diverse comprising primarily of enstatite with various proportions of diopside, inverted pigeonite, forsterite, and albitic plagioclase (Keil, 2010). The aubrite parent body is believed to have accreted in the same part of the solar nebula as the EC parent bodies under comparably reducing conditions around ~1.5 Myr post-CAI condensation (Desch et al., 2018; Barrat et al., 2016).

Ureilites are coarse-grained ultramafic achondrites rich in olivine and pigeonite, that also contain significant amounts of metal (<5 wt%) and carbon phases (~3 wt%), which include graphite and high-pressure diamond (Goodrich, 1992; Nestola et al., 2020). Ureilites are further sub-divided based on their petrology into two groups- main group ureilites (formerly referred to as monomict or unbrecciated ureilites and accounting for 95% of all ureilites) and polymict ureilites. The ureilite parent body (UPB) is generally believed to have accreted within <1 Myr post-CAI condensation (Zhu et al., 2020; Desch et al., 2018; Goodrich et al., 2015), possibly as early as 0.6 Myr (Goodrich et al., 2015; Wilson and Goodrich, 2016). However, some evidence suggests a younger accretion age for the UPB of 1.6-1.7 Myr (Budde et al., 2015; Hilton and Walker, 2020). The UPB is thought to have been catastrophically disrupted by a major impact event around 5 Myr post-CAI condensation (Figure 4; e.g., Desch et al., 2019(a)). The exact origin of the impactor and its geochemical composition is debated (Desch et al., 2019a; Rai et al., 2020), however it likely had some influence on observed

ureilite geochemistry (e.g., Goodrich and Desch, 2019) and is thought to be responsible for observed noble gas abundance in ureilites (Amari et al., 2020). Evolution of the UPB is described in greater detail in chapter five. Polymict ureilites are considered to be derived from the regolith or outer areas of the UPB or ureilite daughter bodies (UDBs; e.g., Goodrich et al., 2015). On the other hand, main group ureilites are believed to represent preserved UPB mantle residues formed after the extraction of feldspar rich magmas and sulfur-rich iron melts (e.g., Bischoff et al., 2014; Rankenburg et al., 2008; Barrat et al., 2015; Barrat et al., 2016).

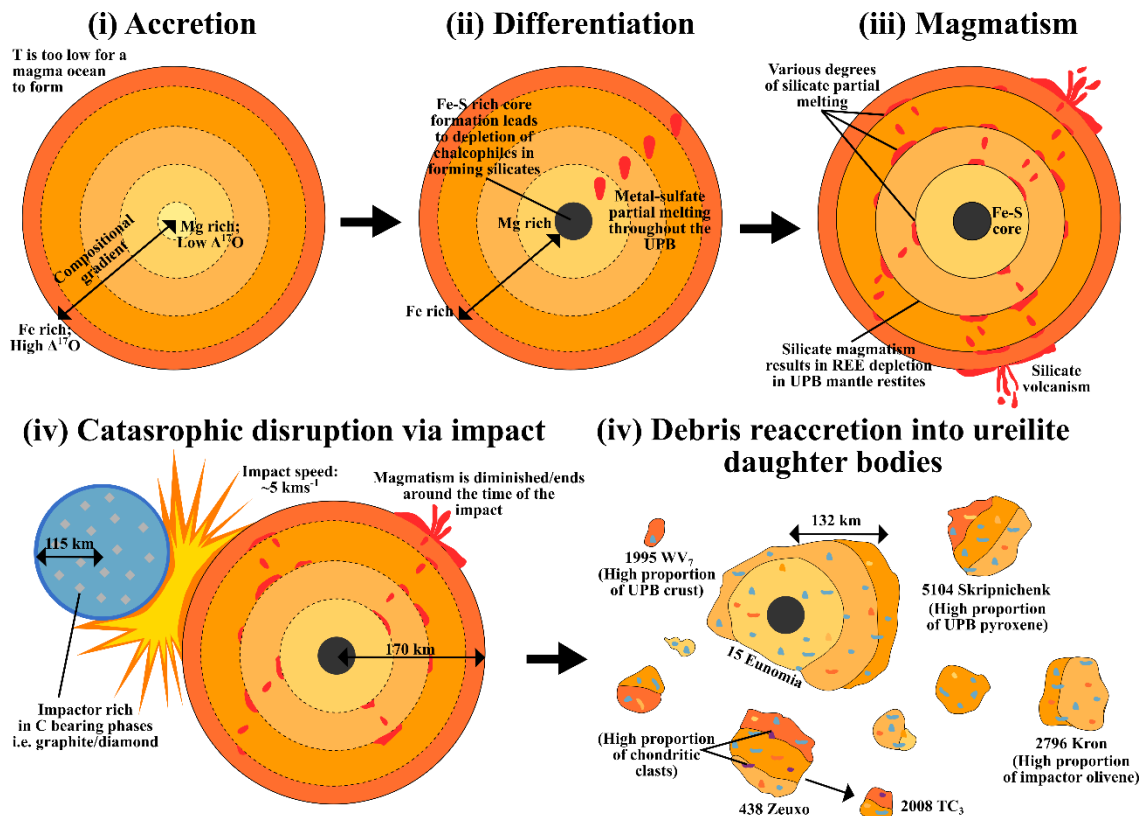


Figure 4- Model depicting the evolution of the UPB (i) Accretion of early solar system materials, primarily MgO-rich and FeO-rich chondrules. It is believed MgO-rich chondrules accrete slightly earlier, resulting in a compositional gradient within the planetesimal. (ii) Early heating facilitated by accretion and short-lived isotope decay and formation of eutectic metal-sulfide melts and a Fe-S core. Onset of partial melting. (iii) Increased silicate partial melting and loss of magma via explosive volcanism. (iv) Catastrophic disruption of the UPB by an unknown impactor. A greater proportion of FeO-rich material was removed from the planetesimal than deeper MgO-rich material; the UPB core was not disrupted. (v) Impactor and UPB debris reaccreted to form UDBs composed of jumbled fragments, though no UDBs have been formally identified those labelled here are all potential candidates (Desch et al., 2019a). Adapted from Rai et al., (2020).

2.1.2 Carbonaceous meteorites

Carbonaceous chondrites are subdivided into multiple classes (CB, CH, CI, CK, CM, CO, CR and CV), and are believed to have accreted in the outer solar system between 2.4-4.1 Myr post-CAI condensation (Desch et al., 2018). The carbonaceous chondrites all formed well beyond the snowline and therefore accreted in the presence of abundant H₂O. The first non-iron carbonaceous meteorites to form were CV and CK chondrites which have comparable geochemistry, sharing very high mass fractions of CAIs (Wasson et al., 2013). Similarities between CV and CK chondrites are believed to originate from the CV and CK parent bodies accreting at similar times, close to the proposed location of proto-Jupiter's associated pressure barrier (Desch

et al., 2018), though it has also been posited that the two groups may share a common parent body (e.g., Dunn et al., 2016). Typically, CV chondrites possess large chondrules and refractory inclusions, enclosed in a predominantly FeO-rich olivine coarse-grained matrix (e.g., Brearley and Jones, 1998) and are of petrological type-3, hence they are commonly referred to as CV3 chondrites. The CV chondrites are subdivided by into reduced and oxidized subgroups (McSween, 1977); in the reduced subgroup, metal predominates over magnetite, whereas metal is either absent, or present in only trace amounts in the oxidized subgroup (Krot et al., 1995). Also noteworthy are the CI chondrites, which are enriched in volatiles (H, C, N O etc.; e.g., Lodders, 2003) and are often heavily affected by aqueous alteration, having some of the highest concentrations of water (~12-13 wt%) measured in any chondrite (Alexander et al., 2013; King et al., 2020). The CI parent body is believed to have accreted in a cold part of the presolar nebula, likely at a substantial distance from the Sun, beyond the snowline (< 15 AU; Desch et al., 2018), as CI meteorites are noted to have near primordial water/rock mass ratios (Krot et al., 2015) and lack obvious chondrules and CAIs (e.g., Morlok et al., 2006; King et al., 2020).

Compared to NC achondrites, CC derived achondrites are poorly sampled in Earth's meteorite collections; therefore, CC achondrites are not a well-studied class, though in recent years there has been a push to reanalyse previously ungrouped achondrites with many subsequently identified as having CC characteristics (Sanborn et al., 2019; Sanborn and Yin, 2019). At present several distinct CC achondrite chemistries have been observed. These chemistries are thought to be representative of at least four distinct parent bodies (e.g., Huyskens et al., 2019), which appear to have formed in similar regions of the protoplanetary disk as CV (e.g., Sanborn and Yin, 2019) and CR chondrites (Huyskens et al., 2019; Sanborn et al., 2019). The magmatism responsible for the formation of these achondritic bodies is believed to have spanned a very short time in the CR forming region (~1 Myr; Huyskens et al., 2019), comparable to the magmatic activity durations calculated for outer solar system iron meteorites (Kruijer et al., 2017).

2.2 Principal carbonaceous chondrite components

2.2.1 CAIs

Calcium aluminium inclusions are found in varying abundance across all known chondrites and are most abundant in CC chondrites, excluding CI chondrites where just a single CAI has been observed (Frank et al., 2014). The mineralogy of these inclusions coupled with textural observations and radiometric dating suggest that CAIs were the first materials to condense from the protoplanetary disk (e.g., Connelly et al., 2012). The mineral assemblages of CAIs are dominated by Ca and Al-rich phases such as corundum (Al_2O_3), spinel ((Fe, Mg, Cr, Al, Ti) $_3\text{O}_4$), perovskite (CaTiO_3), and anorthite ($\text{CaAl}_2\text{Si}_2\text{O}_8$) (MacPherson et al., 2005). These assemblages primarily comprise the minerals predicted to condense first from the cooling proto-molecular cloud as it collapses to form the initial protoplanetary disk (e.g., Ebel and Grossman, 2000). The presence of these early condensing minerals reinforces the prevailing view that CAIs were likely the first materials to

condense in the disk, though a few of the minerals and textures present in CAIs are the product of later melting (e.g., MacPherson et al., 2017) and hydrothermal alteration events (e.g., Tang et al., 2017). Refractory lithophile elements (e.g., Ca, Al, Ti, Y, Zr, Hf and rare earth elements (REE)) are also typically enriched in CAIs. Despite being used as the metric by which the start of the solar system is measured, not all CAIs formed instantaneously and while most are believed to be condensed in ~20 kyr (canonical CAIs), many more continued to condense and undergo various forms of processing for ~0.7 Myr post after the defined solar system t_0 (MacPherson et al., 2017). There are two main CAI varieties that are believed to predate canonical CAIs (e.g., Kööp et al., 2016); these are PLAC-like CAIs and FUN-type CAIs, which are considered to be representative of the earliest disk compositions as they preserve more pronounced nucleosynthetic anomalies than canonical CAIs (e.g., Sahijpal et al., 1998).

2.2.2 AOAs

Amoeboid olivine aggregates are fine-grained, irregularly shaped refractory inclusions comprising aggregates of olivine and several other minerals including anorthite, Ca-rich clinopyroxenes (e.g., pigeonite (Ca, Mg, Fe)(Mg, Fe)Si₂O₆), FeNi metal, and less commonly spinel, perovskite, and melilite ((Ca, Na)₂SiO₇) (Krot et al., 2004). The majority of AOAs are not as refractory-rich as CAIs and are present in most chondrites in varying abundance, though are a relative minor component of most CC chondrites compared to CAIs (<1 vol%); however, CV and CO chondrites can contain relatively large concentrations of AOAs (up to 9 vol% and 16 vol% respectively; McSween, 1977). Radiometric dating and direct observation of AOAs suggests that they formed in very similar environments to CAIs, condensing directly from protoplanetary disk gases at very similar times (e.g., Krot et al., 2004). The lack of abundant AOAs in most chondrites may be because they are surviving representatives of precursor condensed materials that accreted and later melted to form chondrules (e.g., Yurimoto and Wasson 2002).

2.2.3 Chondrules

Chondrules are mm-sized spherules found in large concentrations in all known NC and CC chondrite groups, excluding CI chondrites where they are found fractured and in low abundances (making up < 5 vol% compared to 15-80 vol% in all other chondrite groups; Leshin et al., 1997). Chondrules are known to have evolved as free-floating objects that were processed by transient heating in the protoplanetary disk (e.g., Krot et al., 2014), however the exact mechanism responsible for chondrule formation is debated. Various models for the chondrule formation mechanism have been present including passage through large-scale nebular shocks (e.g., Morris & Desch, 2010), passage through bow shocks around large planetary embryos (e.g., Mann et al., 2016) and impact melt droplets during collisions between asteroids (e.g., Lichtenberg et al., 2018). One commonality between these models is that these mechanisms were all active early in the solar systems history as radiometrically dated chondrules indicate that chondrules may have formed as early as 0.1-0.9 Myr (e.g., Kita et al., 2000; Schrader et al., 2017).

However, despite many of these early ages it is the canonical view that chondrules are genetically linked to their bulk meteorite compositions with the nucleosynthetic anomalies in ^{50}Ti and ^{54}Cr of individual chondrules observed to be very similar to their respective bulk meteorites (Olsen et al., 2016; Gerber et al., 2017). The similarities in chemistry between chondrules and their bulk chondrite implies a close relationship between the regions where chondrules formed and where they later accreted into their respective parent bodies alongside other disk materials. Such a relationship has been observed between chondrules and their bulk meteorites (e.g., Tenner et al., 2019), suggesting that most chondrules may have a very short time between formation and accretion into a planetesimal and therefore most will be sourced locally in the region where a parent bodies accretes. The major exception to this hypothesis are CV chondrites, whose parent body appears to have sampled a wide variety of chondrules from across most known chondrite groups (Olsen et al., 2016; Gerber et al., 2017), hinting that these chondrules or their precursor materials were not locally sourced from the CV accretion region but instead were transported to the CV accretion region from elsewhere in the protoplanetary disk (Olsen et al., 2016; Williams et al., 2020).

2.2.4 Presolar SiC grains

Among the large variety of presolar materials, SiC is the best characterised, largely due to its acid resistivity allowing relatively easy separation from bulk meteorites and extensive cleaning to remove any potential terrestrial or solar contaminants (e.g., Liu et al., 2014). Presolar SiC grains are divided into distinct sub-types based on the C, N and Si isotopic compositions; the main presolar SiC grain sub-types are mainstream (the most common SiC grain type), AB, C, X, Y, and Z. Mainstream, Y, and Z grains are thought to originate from low-mass AGB stars with mainstream grains originating from stars with solar metallicity and Y and Z grains from stars with subsolar. These three grain types comprise more than 90% of known SiC grains (e.g., Clayton and Nittler 2004). Mainstream SiC grains are known to be depleted in ^{84}Sr and enriched in s-process Sr isotopes (Liu et al., 2015; Stephane et al., 2018) and have been suggested as the potential carrier of ^{84}Sr for the NC reservoir (e.g., Paton et al., 2013). C and X grains are believed to originate from Type II supernovae. It is possible that AB grains are also derived from Type II supernovae (Liu et al., 2015) though their exact origin is still a matter of debate (e.g., Asplund et al., 1998). Though they only comprise a very low proportion of presolar SiC grains, X grains can also be subdivided into three sub-groups X0, X1 and X2 based on their nucleosynthetic isotopes (Lin et al., 2010). Mainstream SiC grains and X-type grains have previously been found to possess a wide range of s-process Sr isotope compositions but are similarly depleted in ^{84}Sr to mainstream grains (Liu et al., 2015; Stephane et al., 2018). In the case of X-type grains these variations have been ascribed to the weak s-process, which occurs in massive stars prior to supernova explosion (Stephane et al., 2018).

2.2.5 Matrix

Chondritic matrix materials are typically defined as an optically opaque mixture of grains (10 nm to 5 μ m in size) that fill interstices between chondrules, CAIs and other major components and often rim them (e.g., Scott et al., 1988). Matrices are distinguished from other chondritic components by their distinct sizes, shapes and textures and account for a large proportion on most chondrites (5-50 vol%). Matrix materials are thought to comprise a mixture of presolar materials and nebula condensates, which subsequently mixed with chondrule fragments; typically, matrices encompass a wide variety of mineral compositions including silicates, oxides, sulfides, phyllosilicates, carbonates and metallic Fe and Ni (Scott and Krot, 2005). The matrices of many carbonaceous chondrites are thought to be largely unaltered, e.g., Allende (Neuland et al., 2021), though remain poorly studied compared to other chondritic components isotopically. Geochemical studies of Allende have highlighted that its matrix is chemically homogenous possessing strong depletions of volatile elements (Scott and Krot, 2005; Neuland et al., 2021). Major and trace element chemistry of Allende matrix suggests that the process that mixed chondrules with matrix materials did not result in significant element or mineral fractionation (Neuland et al., 2021).

3. Samples and analytical methods

3.1 Samples

Fourteen bulk ureilite samples and two mineral separates were analysed in this study, comprising a mixture of main-group and polymict ureilites. Comprehensive Sr isotope data was also obtained for CAIs and Allende meteorite components in this study after previous analysis of $^{87}\text{Sr}/^{86}\text{Sr}$ and $\delta^{88}\text{Sr}$ analysed previously by Kevin Burton and Sune Nielsen (WHOI). Specific details regarding the analysis of these CAIs are given in chapter four. Bulk meteorite samples were crushed from interior chips under sterile conditions in Durham Universities clean laboratory facilities. Analytical techniques used in this study follow established methods designed by Charlier et al. (2006), with an emphasis on minimising all possible terrestrial contamination and optimising chemical separation techniques. All ‘find’ bulk powders were leached in warm ~2 M HCl for 20 minutes, rinsed in MilliQ water and then dried in an oven to remove the possibility of terrestrial contamination, as Sr is known to be sensitive to arid/desert weathering (Braukmüller et al., 2018). Other bulk powders prepared from ‘falls’ or from terrestrial samples were not leached. Measured sample sizes ranged from 103.5 mg to 162 mg. Samples were dissolved in concentrated HF–HNO₃ (3:1 mixture) at 130 °C on a hotplate, then almost dried down before the addition of aqua regia. Refractory C-phases were only observed in small quantity after acid digestion. Full dissolution of these phases was not deemed necessary as it is highly unlikely that these phases would contain significant enough Sr to affect bulk isotope measurements and as indicated by previous studies (e.g., Charlier et al., 2017). Following this, all samples were completely dried down and dissolved in 6M HCl. Aliquots from the initial dissolutions were removed for trace element and Rb and Sr concentration determination via ICP-MS with the remaining portions of the bulk dissolutions converted to nitrate form and internally equilibrated in 8 M HNO₃. For each sample the solution was aliquoted as follows (i) equivalent to 1 mg of sample was taken for trace element analysis (ii) equivalent to 1 µg of Sr for measurement of the natural (unspiked) Sr and (iii) equivalent to 500 ng for the addition of ^{84}Sr - ^{87}Sr double spike, also for isotope measurement.

3.2 ICP-MS

Once suitable aliquots had been taken, samples and blanks were prepared using a HNO₃/HF mixture (Romil SPA-grade) in Savillex 22 mL PFA vials followed by evaporation and further addition of HNO₃. After driving off the initial HF/ HNO₃ mixture, samples were then taken up in 1 mL of concentrated HNO₃ and dried again. Following this, a further 2.5 mLs of concentrated HNO₃ was added alongside 0-15 mL of high-purity water, before leaving samples overnight on a hot plate. After cooling, samples were further diluted to exactly 50 mL again using high purity water, to yield a solution in approximately 3.5% HNO₃. Sample and standard weights were 0.1000 ± 0.001 g. Re and Rh internal “spikes” were added during the final dilution to 50 mL, to yield 20 ppb in solution. Samples, blanks and standards (BHVO-2, JB-2, AGV-2 and BCR-2) were then run on an Thermo XSERIES 2 inductively coupled plasma mass spectrometer (ICP-MS) at Durham University

(Department of Earth Sciences) by Dr Chris Ottley. Analytical precision was within $\pm 5\%$ for the elements reported.

3.3 Sr isotope measurements

The remaining bulk solution after ICP-MS aliquoting was further divided into two equal portions, one optimally spiked with ^{84}Sr - ^{87}Sr double-spike before column separation and the other left untouched. The double-spike and natural aliquots were then processed independently, with all further manipulations and separations carried out in separate laminar flow cabinets and using equipment specifically designated for use with spiked or natural samples, respectively. However, the methods used for each of the spiked and natural aliquots were left identical removing the possibility of differential blank issues. Strontium was separated from both aliquots using identical protocols involving sorbing the Sr onto Sr-spec resin and eluting matrix elements in 3 M HNO_3 , then recovering Sr in MQ H_2O (Figure 5). Samples were processed in batches of 10, alongside a blank (determined by isotope dilution using a dilute ^{84}Sr single spike), which never exceeded 18 pg. No blank correction was applied for any of the Sr samples analysed throughout this study as the analyte amount taken was of the order of hundreds of ng for both DS and natural aliquots.

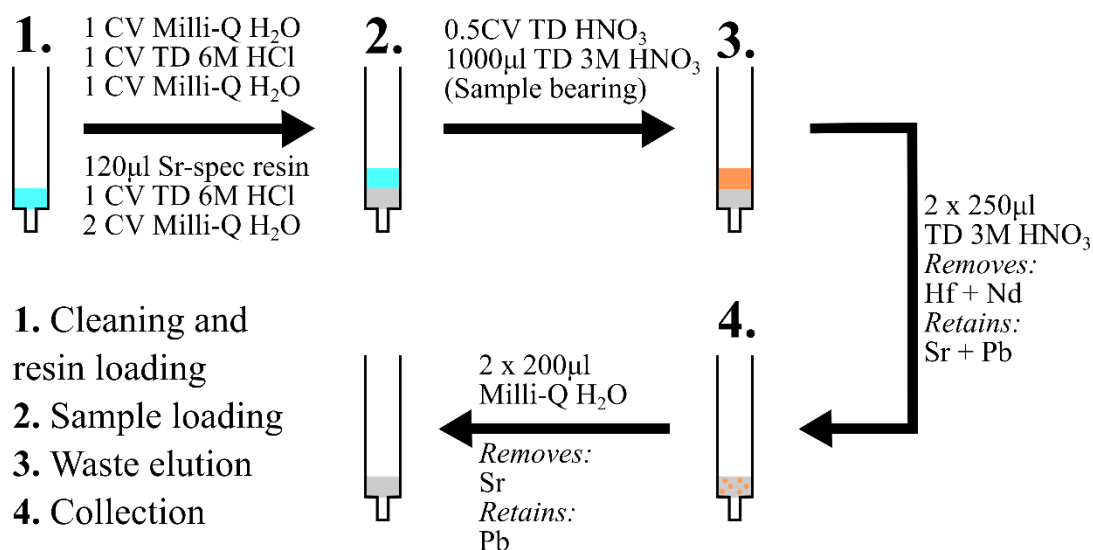


Figure 5- Summary illustration of the Sr separation scheme, demonstrating retention and loss of phases at each stage. CV = Column volume TD = Teflon distilled

All Sr samples were loaded onto 99.999% Re filaments, spot welded onto posts and outgassed at 30 minutes at 4.5 A. The filaments were first heated to 0.9 A and a thin Parafilm® layer was melted onto the surface, creating a central 1.5 mm gap in the Re ribbon for sample loading in order to concentrate the sample and prevent it from spreading across the filament. The current was reduced to 0 A and 1.0 μl of TaF_5 activator was added to the filament, to enhance efficiency of ionization of Sr (Birck, 1986). Samples were dissolved in 0.8 μl 16 M HNO_3 and added directly to the TaF_5 droplet. The current was increased to 1.0 A drying the sample. Once beige in colour, the current was increased to 1.5 A, turning the sample black and burning off remaining Parafilm®. The current was then increased until a dull red glow was observed (~ 2.0 A) and held 5 seconds before being reduced to 0 A.

Strontium isotope measurements were carried out on a Thermo Fisher Scientific Triton Thermal Ionization Mass Spectrometer (TIMS) at Durham University. Amplifier gains were performed daily to minimise the uncertainty. Filaments were heated slowly at 100 mAmin⁻¹ reaching a temperature of 2400 mA, minimising Sr ionization before analysis. At 2400 mA the lens was autofocused before a further increase to 2800 mA, where a second autofocus was performed. Once the lenses were focused, the rate of heating was lowered to 10 mAmin⁻¹ and set to a maximum of 3100 mA. The voltage for sample runs ranged from 1 to 12 V ⁸⁸Sr for 12 blocks of 20 cycles with 4 second integrations (total 240 measurements), with amplifier rotations in between each block measurement. Run time for each sample was ~2.5 hours, including 40 minutes of filament heating.

Instrumental fractionation for un-spiked measurements was corrected for using ⁸⁶Sr/⁸⁸Sr = 0.1194 (Nier, 1938) to determine radiogenic ⁸⁷Sr/⁸⁶Sr ratios. Instrumental fractionation for natural un-spiked measurements was corrected for using ⁸⁶Sr/⁸⁸Sr = 0.1194 (Nier, 1938) to determine the radiogenic ⁸⁷Sr/⁸⁶Sr ratios. The average values and reproducibility of the NBS987 for ⁸⁷Sr/⁸⁶Sr was 0.7102655 ± 46 (n = 25). Stable Sr isotope ratios were determined from the raw data for both spiked and un-spiked samples by deconvolving, using the exponential fractionation law and Newton-Raphson iterative sequence in ⁸⁷Sr denominator space (Albarède and Beard, 2004). The stable isotope data are presented in the standard delta notation with deviations in ⁸⁸Sr/⁸⁶Sr and ⁸⁴Sr/⁸⁶Sr in per mille (‰) relative to the NBS-987 standard:

$$\delta^i\text{Sr} = \left(\frac{(^i\text{Sr}/^{86}\text{Sr})_{\text{sample}}}{(^i\text{Sr}/^{86}\text{Sr})_{\text{reference}}} - 1 \right) \times 1000 \quad (\text{Eq.1})$$

Over the period of measurement the external reproducibility on $\delta^{84}\text{Sr}/^{86}\text{Sr}$ (2 s.d.) was 0.028‰, and for $\delta^{88}\text{Sr}/^{86}\text{Sr}$ (2 s.d.) was 0.014‰ (cf. Charlier et al. 2017). Repeat measurement of the rock reference material BHVO-2 yielded values for $^{87}\text{Sr}/^{86}\text{Sr} = 0.703464 \pm 3$ and $\delta^{88}/^{86}\text{Sr} = 0.266 \pm 0.010\text{‰}$ (2 s.d., n = 3) indistinguishable to those obtained by Klaver et al. (2020) of $^{87}\text{Sr}/^{86}\text{Sr} = 0.703476 \pm 7$ and $\delta^{88}/^{86}\text{Sr} = 0.267 \pm 0.010\text{‰}$ (2 s.d., n = 6).

4. Early solar system materials: Calcium-Aluminium Inclusions and chondrules from the meteorite Allende

4.1 Background on early solar system materials and Allende

4.1.1 The origins of CAIs

Among the various constituents of chondritic meteorites, CAIs are somewhat unique as they hold a record of the nebular processes that shaped the initial composition of the protoplanetary disk and ultimately the compositions of all early planetary materials. These inclusions are also believed to be the oldest solids formed in the solar system (e.g., Connelly et al., 2012), having condensed from cooling nebula-derived gases of solar composition (e.g., MacPherson, 2014). As such, the study of CAIs potentially allows the processes that controlled material compositions in the early solar system to be constrained. However, despite extensive study, the exact nature of these nebular processes remains elusive as CAIs have a complicated and as yet not entirely resolved post-condensation history. Unravelling this complexity is made more difficult as there is also debate as to exactly where in the solar system CAIs condensed.

The oxygen (O) isotope systematics of more pristine samples coupled with other elemental and isotopic evidence indicate that CAIs formed under extremely high temperature, low fO_2 conditions, likely linked to the solar environment around the proto-Sun (Scott et al., 2018; Desch et al., 2018; Saji et al., 2020), however CAIs are most abundant in several CC chondrite classes (up to ~3 vol%), with very few found in inner solar system chondrites (<0.2 vol%). The abundance of CAIs in outer solar system materials have led others to argue CAIs must have formed elsewhere in the early solar system in a similar environment to that of the proto-Sun, e.g., during the early accretion of Jupiter (Brennecka et al., 2018). The current model for the formation of CAIs places their formation in the inner solar system close to the proto-Sun before being rapidly transported to the outer solar system prior to the separation of the inner and outer solar system around the time of the formation of proto-Jupiter, accounting for the disparity between NC and CC abundances (Nanne et al., 2019; Kleine et al., 2020). Much debate also still surrounds the post-condensation processing in CAIs that leads to changes in their textures, isotopic compositions and mineralogical assemblages (Krot et al., 1995; MacPherson et al., 2012). It is widely believed that most sampled CAIs originally formed as fine-grained condensates, with many later experiencing episodes of re-melting to form coarser-grained igneous textures though the exact timing of these events are not well established (e.g., Mendybaev et al., 2021). There is also abundant evidence that the mineralogies of some CAIs (both fine and coarse-grained) have been aqueously altered at some stage to form secondary minerals such as nepheline, sodalite and ilmenite (Krot et al., 2004; Tang et al., 2017). However, it is still uncertain when and where this alteration occurred and whether it reflects nebular and/or asteroidal processes (e.g., Krot et al., 1995; Tang et al., 2017).

In addition to complexities around CAIs post-condensation histories, there are unanswered questions around the controls on isotopic anomalies observed in bulk CAIs, which are believed to derive from original nebula

materials. The nucleosynthetic processes responsible for the isotopic anomalies in these materials (r-, s- and p-process) are diverse, yet most CAIs possess similar anomalies for a given element (excluding FUN-type CAIs, which are isotopically anomalous for many elements and are believed to have condensed earlier than most canonical CAIs; Kööp et al., 2016). An overarching explanation for the observed isotopic diversity in CAIs has yet to be reached, although several possible hypotheses have been postulated including heterogeneity in the molecular cloud and injection of supernovae materials into the protoplanetary disk post-CAI condensation (e.g., Dauphas and Schauble, 2016; Brennecka et al., 2020). Furthermore, it is also unclear at present whether the stable isotope fractionation effects measured in CAIs correlate with observed nucleosynthetic anomalies. Such correlations would support arguments that exotic pre-solar materials were once present in CAIs but were selectively destroyed through thermal processing (Trinquier et al., 2009; Davis et al., 2018), though such a scenario is currently considered to be unlikely (e.g., Kleine et al., 2020). In this respect, strontium isotope systems provide a valuable perspective on CAI genesis and processing, as they are able to address the possibilities of alteration and fractionation simultaneously.

4.1.2 Allende

Allende is the largest carbonaceous chondrite ever recovered on Earth having impacted in Mexico early in 1969. After breaking up in the atmosphere, an extensive search for material was conducted and over two tonnes of the meteorite were recovered. The availability of large quantities of samples of Allende has enabled extensive study of the meteorite and its constituent materials and it is sometimes described as "the best-studied meteorite in history" (Ma et al., 2014). Allende CAIs are utilised here as they have been well-studied over the past half a century and their size and abundance in the host meteorite allows for multiple isotope systematics to be investigated on individual inclusions with relative ease. However, a significant drawback of Allende CAIs is that they have experienced various degrees of metasomatic aqueous alteration, presumed to have occurred on the CV parent-body (e.g., Yurimoto et al., 2008) and are typically not as pristine when compared to CAIs from reduced examples of CV chondrites (e.g., Efremovka).

4.2 Sample preparation and methods

Allende CAI fragment splits of between 5 and 15 mg were handpicked using a binocular microscope for Sr isotope analyses (see Table 1). During fragment selection, great care was taken to avoid contamination and select the most pristine CAI samples (see Bekaert et al., 2021). Several chondrules and matrix samples were also picked from the same Allende samples for analysis. Fragments were then directly digested without powdering using double-distilled concentrated HF, HNO₃, and HCl. Insoluble phases (fluorides and refractory minerals, e.g., spinel) were further digested in concentrated HNO₃ in an Anton Parr high pressure asher at ~110 bar and 260 °C. All samples were then fully digested using the method described in chapter 3 with no solid residue remaining. Elemental concentrations were measured for all samples using a ThermoFinnigan iCap quadrupole ICP-MS, located at the WHOI Plasma Mass Spectrometry Facility. Accuracy and precision were

better than $\pm 7\%$ (2SE) based on the correspondence of concentrations in USGS reference materials AGV-2, BCR-2, and BHVO-2 determined during the same analytical sessions as the CAIs.

Table 1- Descriptions of all CAIs analysed in this study.

Sample name	CAI75	CAI352 9-42	CAI65	CAI08	CAI30	CAI01a	CAI01b	CAI02	CAI03
Texture	coarse-grained	coarse-grained	coarse-grained	coarse-grained	coarse-grained	fine-grained	fine-grained	fine-grained	fine-grained
REE group	III	III	I, V	I, V	III	II	II	II	II

Strontium separation and mass spectrometry closely follows the methods outlined in chapter three. Instrumental fractionation for natural un-spiked measurements was corrected for using $^{86}\text{Sr}/^{88}\text{Sr} = 0.1194$ (Nier, 1938) to determine the radiogenic $^{87}\text{Sr}/^{86}\text{Sr}$ ratios. The average values and reproducibility of the NBS987 for $^{87}\text{Sr}/^{86}\text{Sr}$ was 0.7102655 ± 46 ($n = 25$). Stable Sr isotope ratios were determined from the raw data for both spiked and un-spiked samples by deconvolving, using the exponential fractionation law and Newton-Raphson iterative sequence in ^{87}Sr denominator space (Albarède and Beard, 2004). Over the period of measurement the external reproducibility on $\delta^{84}\text{Sr}/^{86}\text{Sr}$ (2 s.d.) was 0.028‰, and for $\delta^{88}\text{Sr}/^{86}\text{Sr}$ (2 s.d.) was 0.014‰ (cf. Charlier et al., 2017). Repeat measurement of the rock reference material BHVO-2 yielded values for $^{87}\text{Sr}/^{86}\text{Sr} = 0.703464 \pm 3$ and $\delta^{88}\text{Sr}/^{86}\text{Sr} = 0.266 \pm 0.010\text{‰}$ (2 s.d., $n = 3$) indistinguishable to those obtained by Klaver et al. (2020) of $^{87}\text{Sr}/^{86}\text{Sr} = 0.703476 \pm 7$ and $\delta^{88}\text{Sr}/^{86}\text{Sr} = 0.267 \pm 0.010\text{‰}$ (2 s.d., $n = 6$).

4.3 Results

4.3.1 Rare Earth Elements

The Rare Earth Element (REE) patterns of CAIs are thought to be a product of their condensation and evaporation histories (Ireland and Fegley, 2000); many CAIs experience similar condensation and evaporation histories, therefore most can be divided into sub-groups based on their REE patterns. All fine-grained CAIs analysed here possess group II REE patterns; the coarse-grained CAIs possess group I, V, or III REE patterns (Table 2; Figure 6). Group II CAIs are typically characterised by depletion in both highly refractory and volatile REEs (Ireland and Fegley, 2000). Depletion in highly refractory and volatile REEs is consistent with a two-stage evaporation-condensation scenario. Such a scenario likely consists of a period of closed-system, kinetically controlled nebular dust evaporation, before the selective removal of an early formed ultra-refractory-REE phase (e.g., hibonite) followed by condensation of the residual vapor (e.g., Hu et al., 2021). It has been previously demonstrated that mass-dependent isotopic variations of Ca (Huang et al., 2012; Bermingham et al., 2018), Ti (Davis et al., 2018), Mg and Fe (Shollenberger et al., 2019) are coupled with group II REE patterns. The link between group II CAIs and mass-dependent variations is particularly interesting when observing the data collected here, especially in the case of Mg and Fe, as they have 50% condensation temperatures broadly comparable to Sr ($T_{50}(\text{Sr}) = 1464 \text{ K}$, $T_{50}(\text{Mg}) = 1336 \text{ K}$, $T_{50}(\text{Fe}) = 1334 \text{ K}$; Lodders, 2003). Generally, CAIs with group II REE patterns tend to have lighter isotope compositions

compared to group I pattern CAIs, implying kinetically controlled volatility fractionation during condensation of group II CAIs, likely as part of the selective removal of the early REE host phase (Davis et al., 2018; Hu et al., 2021).

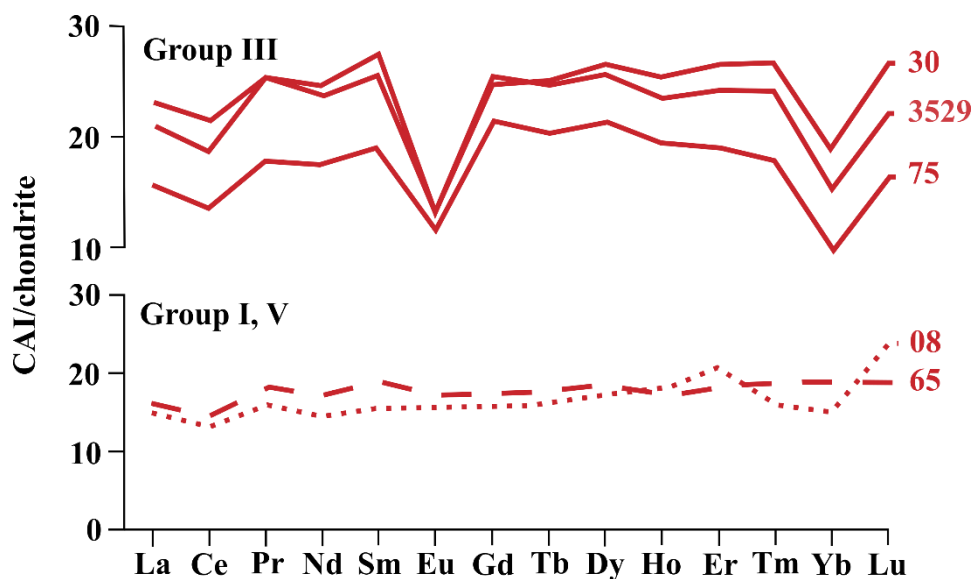


Figure 6- REE profiles for the coarse-grained CAIs analysed in this study. Credit to Bekaert et al. (2021).

Two coarse-grained CAIs (CAI08 and CAI65) have group I or group V REE patterns, which are flat chondrite-normalised profiles, while the other coarse-grained CAIs analysed have similarly flat chondrite-normalised profiles with the addition of depletions in the two most volatile REEs (Eu and Yb), giving rise to group III REE patterns. Group I and V REE patterns are likely the product of near complete condensation from a gas of nebular composition (Davis et al., 2018). However, CAIs with flat REE profiles tend not to experience Ti mass fractionation effects (Davis et al., 2018), probably as Ti and REE condensed almost completely into CAIs. Strontium is less refractory than Ti (Lodders, 2003) and therefore complete Ti condensation does not imply complete condensation of Sr. This conclusion is supported by observed mass fractionation effects in CAIs with flat REE profiles which are associated with evaporation events for elements with condensation temperatures close to Sr (e.g., Mg, and Fe; Shollenberger et al., 2019). Depletions in Eu and Yb in the group III pattern can be produced either by condensation which was isolated from the gas phase prior to the condensation of the more volatile elements, or by distillation, whereby a CAI with a chondritic profile is heated until the more volatile elements are evaporated. This second scenario is favoured to explain the REE profiles of the two coarse-grained CAIs (CAI3529-42 and CAI75), for which the Sr isotope compositions are heavier than the chondritic composition, requiring them to have undergone at least partial evaporation.

4.3.2 Isotopic data

4.3.2.1 Internally normalised $\mu^{84}\text{Sr}$ data

Strontium has four naturally occurring stable isotopes: ^{84}Sr (0.56%), ^{86}Sr (9.86%), ^{87}Sr (7.00%) and ^{88}Sr (82.58%). All four isotopes have distinct nucleosynthetic origins, however measured ^{87}Sr also includes a

radiogenic component from the decay of ^{87}Rb . This radiogenic component is significant as it means that after internal normalization to $^{86}\text{Sr}/^{88}\text{Sr} = 0.1194$ (Nier, 1938), only the $^{84}\text{Sr}/^{86}\text{Sr}$ ratio can be used to directly assess isotopic anomalies. At this point all data was internally normalised to allow direct comparisons with the earlier studies. The internally normalised sample $^{84}\text{Sr}/^{86}\text{Sr}$ ratios are reported here in $\mu^{84}\text{Sr}$ notation, which represents the parts per 10^6 deviation from the average $^{84}\text{Sr}/^{86}\text{Sr}$ ratio of NBS987, a Sr isotope standard, measured alongside the other samples in this study. The data presented here also includes chondrules and matrix separated alongside CAIs from Allende (Table 2; Figure 7). The CAI data reported spans a similar range of $\mu^{84}\text{Sr}$ values to those seen in previous studies (Figure 8), although two samples possess unusually high $\mu^{84}\text{Sr}$ values (285 ± 45 ppm and 679 ± 113 ppm respectively). The mean $\mu^{84}\text{Sr}$ value for all the CAI data plotted in Figure 8 is $+127 \pm 95$ ppm (2 s.d., $n = 55$), while the mean of our data set alone is $+141 \pm 375$ ppm (2 s.d., $n = 12$), or $+92 \pm 169$ ppm (2 s.d., $n = 11$) excluding the unusually high value obtained for CAI30. Coarse- and fine-grained CAIs have slightly different $\mu^{84}\text{Sr}$ anomalies, defining average values of $+192 \pm 236$ ppm (2 s.d., $n = 7$), and $+68 \pm 43$ ppm (2 s.d., $n = 5$), respectively. It is apparent in Figure 8 that there is considerable heterogeneity in our reported $\mu^{84}\text{Sr}$ values that well exceeds analytical uncertainties. Heterogeneities exceeding analytical uncertainty in bulk CAIs have also been observed in a number of previous studies (Charlier et al., 2019; Myojo et al., 2018; Paton et al., 2013; Moynier et al., 2012; Hans et al., 2013; Burkhardt et al., 2019), implying the existence of additional heterogeneity below the scale of whole CAI sampling. Further evidence for heterogeneity below the scale of whole CAI sampling lies in the disparity between core/rim data to the bulk data in samples CAI1A and CAI1B.

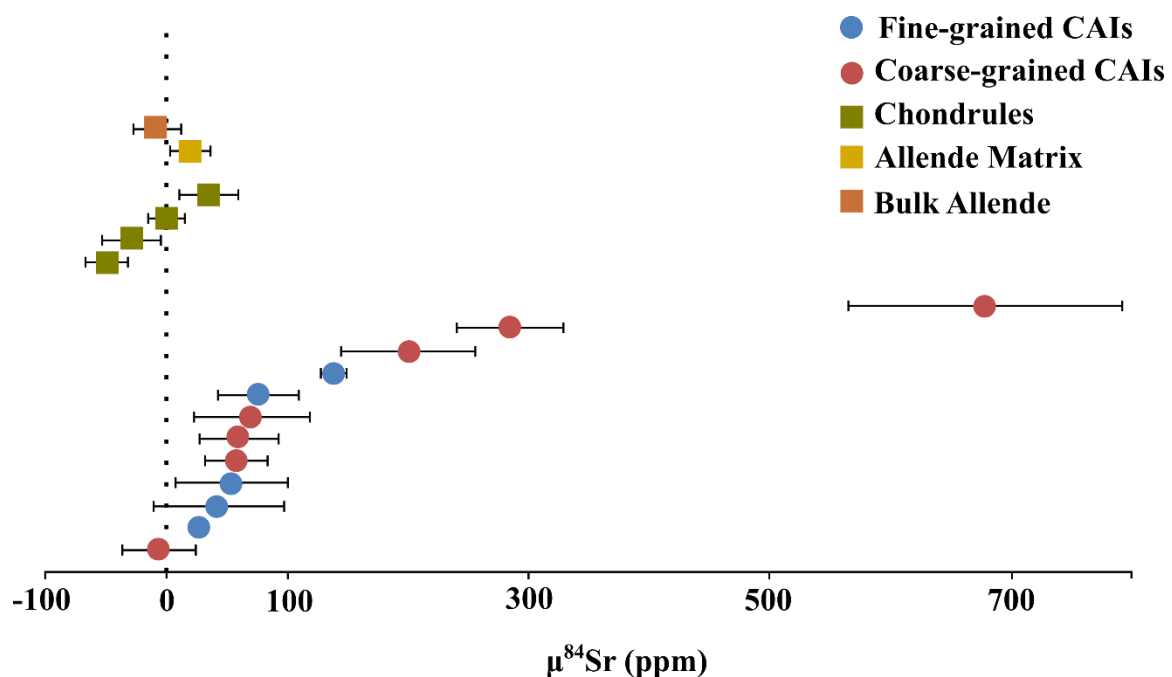


Figure 7- A plot of all CAI $\mu^{84}\text{Sr}$ data obtained in this study alongside chondrule, matrix and bulk data for their host meteorite Allende.

Table 2- Elemental and isotopic data for all Allende CAIs, chondrules and matrix analysed in this study.

Sample	Texture	$^{87}\text{Sr}/^{86}\text{Sr}$	$^{84}\text{Sr}/^{86}\text{Sr}$	$\mu^{84}\text{Sr}$ (ppm)	Error (ppm)	$\delta^{84/86}\text{Sr}$ (‰)	2s.e. (‰)	$\delta^{88}\text{Sr}$ (‰)	2s.e. (‰)	Rb (ppm)	Sr (ppm)
CAI 3529-42	Coarse	0.70055	0.05647	285	45	-0.3601	0.063	0.6303	0.033	0.93	122.6
CAI 65-1	Coarse	0.69946	0.05649	58	26	-0.0056	0.036	0.0471	0.016	0.39	157.3
CAI 65-2	Coarse	0.69947	0.05644	60	33	-0.9411	0.045	0.9675	0.021	0.39	157.3
CAI 75-1	Coarse	0.70097	0.05639	71	48	-1.8066	0.061	1.8532	0.022	0.74	99.6
CAI 75-2	Coarse	0.70120	0.05638	-6	30	-1.9707	0.044	1.9225	0.026	0.74	99.6
CAI 8	Coarse	0.70168	0.05653	201	55	0.6012	0.073	-0.3859	0.033	2.42	152.2
CAI 30	Coarse	0.70013	0.05664	679	113	2.5637	0.140	-1.8223	0.040	0.76	121.3
CAI 1a Bulk	Fine	0.73078	0.05652	139	11	0.5715	0.030	-0.4159	0.011	14.42	64.6
CAI 1b Rim	Fine	0.72519	0.05658	55	46	1.5991	0.020	-1.4980	0.011	7.40	53.5
CAI 1b Core	Fine	0.74276	0.05660	43	54	1.9922	0.027	-1.8849	0.012	10.18	44.0
CAI 2 Bulk	Fine	0.74369	0.05654	76	34	0.9108	0.044	-0.7990	0.014	6.42	27.0
CAI 3 Bulk	Fine	0.72919	0.05666	27	18	3.0535	0.030	-2.9336	0.018	7.61	44.5
Chondrules <1 mm	N/A	0.71778	0.05654	-29	25	0.9147	0.032	-0.9204	0.011	1.86	18.6
Chondrules >3 mm	N/A	0.80158	0.05659	35	24	1.6834	0.031	-1.6040	0.012	4.42	6.5
Chondrules SiO ₂ -rich	N/A	0.71945	0.05654	0	15	0.8922	0.023	-0.8585	0.011	1.40	13.2
Chondrules S-rich	N/A	0.70994	0.05652	-49	18	0.4351	0.026	-0.4595	0.013	0.58	10.5
Matrix	N/A	0.71866	0.05649	20	17	-0.0361	0.024	0.0679	0.012	1.79	14.7

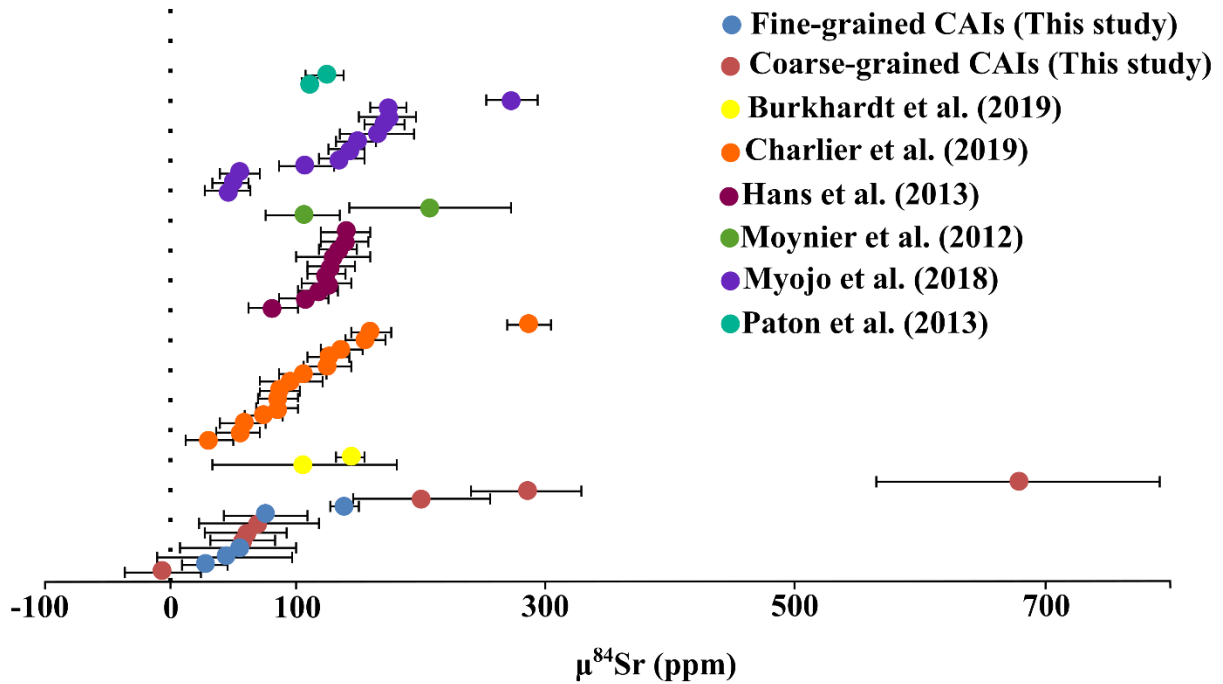


Figure 8- Plot of $\mu^{84}\text{Sr}$ for the data obtained in this study alongside published data for other Allende CAIs (Moynier et al., 2012; Brennecke et al., 2013; Hans et al., 2013; Paton et al., 2013; Myojo et al., 2018).

4.3.2.2 Internally normalized $^{87}\text{Sr}/^{86}\text{Sr}$ and $^{87}\text{Rb}/^{86}\text{Sr}$ data

Typically, Rb/Sr ratios in CAIs are highly variable, with fine-grained CAIs often possessing elevated values consistent with the introduction of chondritic Rb (and likely chondritic Sr to a lesser extent) into the CAIs by alkali-rich secondary alteration fluids (e.g., Charlier et al., 2019). Importantly, ^{87}Sr variations in CAIs are primarily controlled by the radiogenic decay of ^{87}Rb ($T_{1/2} = 49.624$ Gyr; Rotenberg et al., 2012), with ^{87}Rb decay products typically dominating over possible nucleosynthetic and/or mass dependent variations in observable ^{87}Sr abundances. Coarse-grained CAIs appear to possess primitive $^{87}\text{Sr}/^{86}\text{Sr}$ (< 0.702) and low $^{87}\text{Rb}/^{86}\text{Sr}$ ratios (Figure 9), implying that aqueous alteration has had limited influence on their Sr isotope compositions. Conversely, fine-grained CAIs possess $^{87}\text{Sr}/^{86}\text{Sr}$ up to ~ 0.744 suggesting a substantial secondary addition of Rb. All CAIs analysed in this study plot broadly within the errorchron 2σ -envelope defined by coarse-grained CAIs (Figure 9). However, this errorchron has limited geochronological significance due to the large dispersion of the data for the CAIs analysed. Its slope provides a poorly defined CAI condensation age of 4.1 ± 0.7 Gyr, with an initial $^{87}\text{Sr}/^{86}\text{Sr} = 0.69904 \pm 0.00062$ (2σ ; Figure 9), indistinguishable from the current canonical initial $^{87}\text{Sr}/^{86}\text{Sr}$ of CAIs (0.69886 ± 0.00020 ; Charlier et al., 2019).

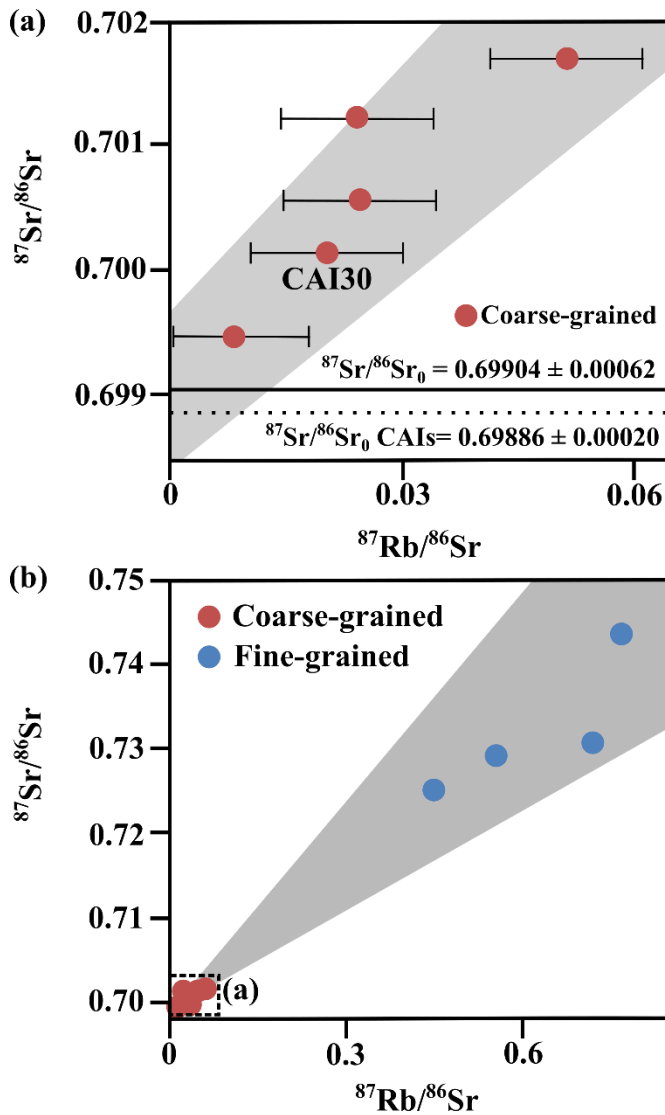


Figure 9- ^{87}Rb - ^{86}Sr errorchron of the Allende CAIs analysed in this study. Coarse-grained CAIs define an errorchron corresponding to an age of 4.1 ± 0.7 Gyr (grey envelopes, MSWD: 2.6). The initial $^{87}\text{Sr}/^{86}\text{Sr}$ corresponding to this errorchron (0.69904 ± 0.00062 at 2σ , horizontal solid line, panel (a)) is similar to the canonical initial $^{87}\text{Sr}/^{86}\text{Sr}$ of CAIs (horizontal dashed line, panel (a); Charlier et al. 2019). Fine-grained CAIs, characterized by much higher $^{87}\text{Rb}/^{86}\text{Sr}$, appear to plot within the error envelope of the coarse-grained CAI errorchron. The observed scatter in the full data set may be indicative of open system processes (e.g., the decoupling of Rb from Sr during alteration/ later addition of Rb) and/or physical admixture of matrix during sampling of the CAIs (Charlier et al., 2019). Credit to Bekaert et al. (2021).

4.3.2.3 Stable Sr isotope data ($\delta^{88}\text{Sr}$ and $\delta^{84}\text{Sr}$)

Stable strontium isotope compositions in CAIs are reported as parts per thousand (‰) deviations from the common Sr reference material NBS987, using the delta notation (Equation 1; Table 2). In three isotope space ($\delta^{88}\text{Sr}$ vs. $\delta^{84}\text{Sr}$), fine- and coarse-grained CAIs form a correlation line covering a total range of $\sim 5\%$ in $\delta^{88}\text{Sr}$, from $+1.92\%$ to -2.93% (Figure 10). A linear regression yields a best fit line with slope -1.06 ± 0.038 (2 s.e.) which passes through an x-intercept value of $\delta^{84}\text{Sr} = 0.129 \pm 0.057\%$. Terrestrial materials have previously been estimated to possess a similar slope to angrites (-1.00 ± 0.11 , intercept 0.001 ± 0.029 ; Charlier et al., 2019), which is closer to the equilibrium mass-dependent fractionation line (MDFL; slope = -0.978 ; Young et al., 2002) expected during kinetic-dominated fractionation. The slope of the best fit line presented here corresponds to the theoretical expectation for mass-dependent fractionation which stipulates that the relative isotopic variations scale as the difference in the absolute masses of the isotopes involved; $(^{84}\text{Sr}-^{86}\text{Sr}) / (^{88}\text{Sr}-^{86}\text{Sr}) \sim -1.0$.

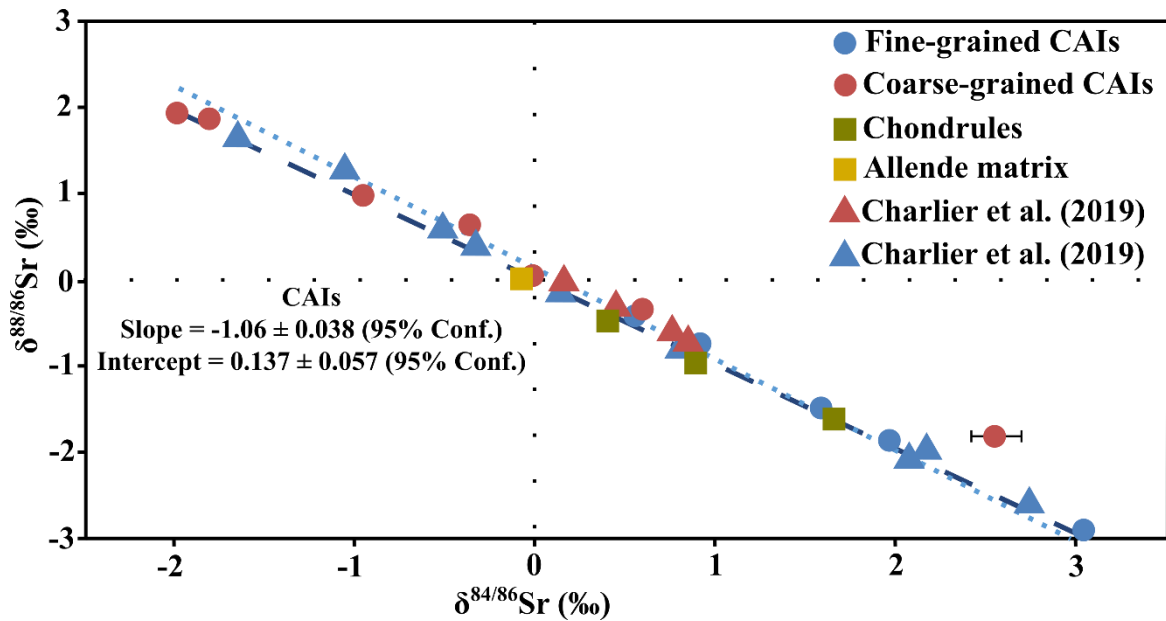


Figure 10- Plot of $\delta^{88/86}\text{Sr}$ vs $\delta^{84/86}\text{Sr}$ for samples analysed in this study. Equilibrium MDFL (dark blue dashed line) denotes the equilibrium mass-dependent fractionation line (solid line) which passes through the origin (the assumed composition of NBS987) with a slope of -0.978 (Young et al., 2002). All errors are smaller than markers.

4.4 Discussion

4.4.1 Nucleosynthetic anomalies in ^{84}Sr

As outlined previously, in order to compare our $\mu^{84}\text{Sr}$ values with published data we calculated the difference between each of the internally normalised $^{84}\text{Sr}/^{86}\text{Sr}$ sample values and the average value for the NBS987 standard. By using a fixed $^{86}\text{Sr}/^{88}\text{Sr}$ ratio for the internal normalisation there is a possibility that if nucleosynthetic anomalies lie in isotopes other than ^{84}Sr they would be concealed, however the data (as in all studies utilising the Sr isotope system) do not allow this to be unambiguously resolved. Here, the data are corrected for mass fractionation using the exponential law. As mentioned previously, the CAIs analysed in this study record significant mass-dependent fractionation (Figure 10). If the natural mass-fractionation experienced by the analysed Allende CAIs does not follow the exponential law, this correction could produce spurious isotopic anomalies after normalisation of the mass spectrometric data to the exponential law, especially in cases where the $^{88}\text{Sr}/^{86}\text{Sr}$ fractionation is large. This effect has been discussed extensively by previous studies in the context of $\delta^{26}\text{Mg}$ and in early solar system chronology from ^{26}Al - ^{26}Mg systematics (e.g., Kita et al., 2013), and Fe isotopic anomalies (e.g., Tang and Dauphas, 2012). The total range in $\delta^{88}\text{Sr}$ is $\sim 5\%$ (+1.92 ‰ to -2.93 ‰; Figure 11). Over this range, all analysed CAIs are resolvably offset from $\mu^{84}\text{Sr} = 0$, regardless of mass-dependent fractionation they may have experienced. There is no significant evidence for a correlation between $\delta^{88}\text{Sr}$ and $\mu^{84}\text{Sr}$ as observed in previous studies (Charlier et al., 2019); however, despite the lack of an overall correlation, fine-grained CAIs generally appear to possess small $\mu^{84}\text{Sr}$ anomalies and light $\delta^{88}\text{Sr}$ values while coarse-grained CAIs have larger $\mu^{84}\text{Sr}$ anomalies and heavy $\delta^{88}\text{Sr}$ values. The correction for natural mass fractionation using the exponential law can induce a bias across the full range in $\delta^{88}\text{Sr}$ values of at most ~ 12.5 μ -units (i.e., the difference in $\mu^{84}\text{Sr}$ values using the different fractionation laws

across the entire measured range of $\delta^{88}\text{Sr}$ values in this study; Figure 11). Hence, the selection of an inappropriate fractionation correction cannot be a significant factor in influencing the $\mu^{84}\text{Sr}$ variability observed in the Allende CAIs.

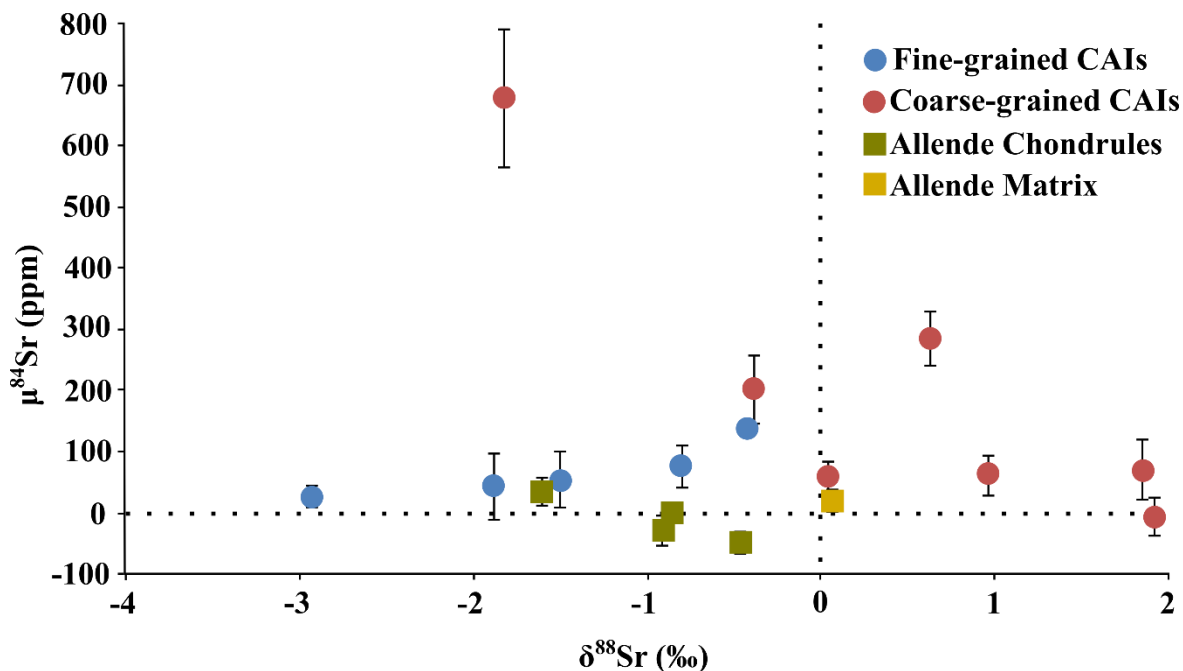


Figure 11- Plot of $\mu^{84}\text{Sr}$ vs. $\delta^{88}\text{Sr}$ for the CAI, chondrule and matrix samples analysed in this study from Allende (CV3). There is no systematic variations between nucleosynthetic anomalies ($\mu^{84}\text{Sr}$) and degree of mass-dependent fractionation ($\delta^{88}\text{Sr}$) for each CAI, regardless of texture. Uncertainties in $\delta^{88}\text{Sr}$ values are smaller than symbol size.

The $\mu^{84}\text{Sr}$ values obtained here for the Allende CAIs are fairly similar to those obtained in previous studies (Figure 8), though one sample (CAI30) possesses a much higher $\mu^{84}\text{Sr}$ than any other previously measured CAI. Our data implies that there is heterogeneity between CAIs, in agreement with the findings of previous studies (Myojo et al., 2018; Charlier et al., 2019). It is possible to rationalise the unusually high bulk $\mu^{84}\text{Sr}$ value reported here for CAI30 by considering the ‘nugget effect’ (e.g., Charlier et al., 2019), which would suggest that an ^{84}Sr -enriched component is present in some inclusions but is difficult to identify in low-mass samples. Such intra-grain heterogeneity beyond analytical uncertainty in $\mu^{84}\text{Sr}$ has previously been reported for a single fine-grained FTA-type CAI (Myojo et al., 2018) and high variability in $\mu^{84}\text{Sr}$ for CAIs with a low sample mass has also been reported previously (Charlier et al., 2019). Based on the data here, it is unlikely that contamination of samples by matrix and/or chondrules can account for CAI30’s high $\mu^{84}\text{Sr}$ value as they possess low $\mu^{84}\text{Sr}$ values. As discussed later, it is also unlikely that CAI30’s high $\mu^{84}\text{Sr}$ is the product of aqueous alteration as the sample is considered to have experienced minor alteration compared to most other CAIs analysed here.

4.4.2 ^{87}Rb - ^{87}Sr isotope systematics

The clearest distinction in our Rb-Sr data is between the coarse-grained CAIs, which have low Rb abundances, low $^{87}\text{Rb}/^{86}\text{Sr}$ ratios and consistently relatively unradiogenic (primitive) $^{87}\text{Sr}/^{86}\text{Sr}$ ratios, and the fine-grained CAIs, which have elevated Rb abundances, high $^{87}\text{Rb}/^{86}\text{Sr}$ ratios, and correspondingly large amounts of

radiogenic Sr ingrowth (Figure 9). Our CAI data falls along a 3.075 ± 0.021 Ga correlation line with an initial $^{87}\text{Sr}/^{86}\text{Sr}$ ratio of 0.69931 ± 0.011 . Our data has greater uncertainties associated with the fit of the CAI age line than previous studies, particularly in regard to our initial $^{87}\text{Sr}/^{86}\text{Sr}$ ratio value for CAIs. Due to the large uncertainty associated with this line, we cannot say that our initial $^{87}\text{Sr}/^{86}\text{Sr}$ for all the CAIs analysed agrees with the ranges in initial CAI values reported for the ‘ALL’ CAI ‘D7’ = ‘USNM#3898’ by Gray et al. (1973): 0.69877 ± 4 , and other CAIs (e.g., Hans et al., 2013: 0.698935 ± 9). Note that the first value is as reported, with no standard normalisation (see Hans et al., 2013), while later values are typically normalised to NBS987 $^{87}\text{Sr}/^{86}\text{Sr} = 0.710250$. The apparent timing implied by our correlation line is significantly more recent than the alteration chronologies yielded by Mn-Cr (3.7 ± 0.7 Myr post-CAI condensation; MacPherson et al., 2015) and ^{129}I - ^{129}Xe systematics ($3.8\text{--}4.5 \pm 0.3$ Myr post-CAI condensation; Pravdivtseva et al., 2003) in CV3 meteorites, including Allende. The observed scatter in the CAI data about the best fit line, is indicative of open system processes (e.g., Rb-Sr decoupling during alteration) post-CAI condensation and likely contributes to the uncertainty our Rb-Sr errorchron age and initial $^{87}\text{Sr}/^{86}\text{Sr}$ value.

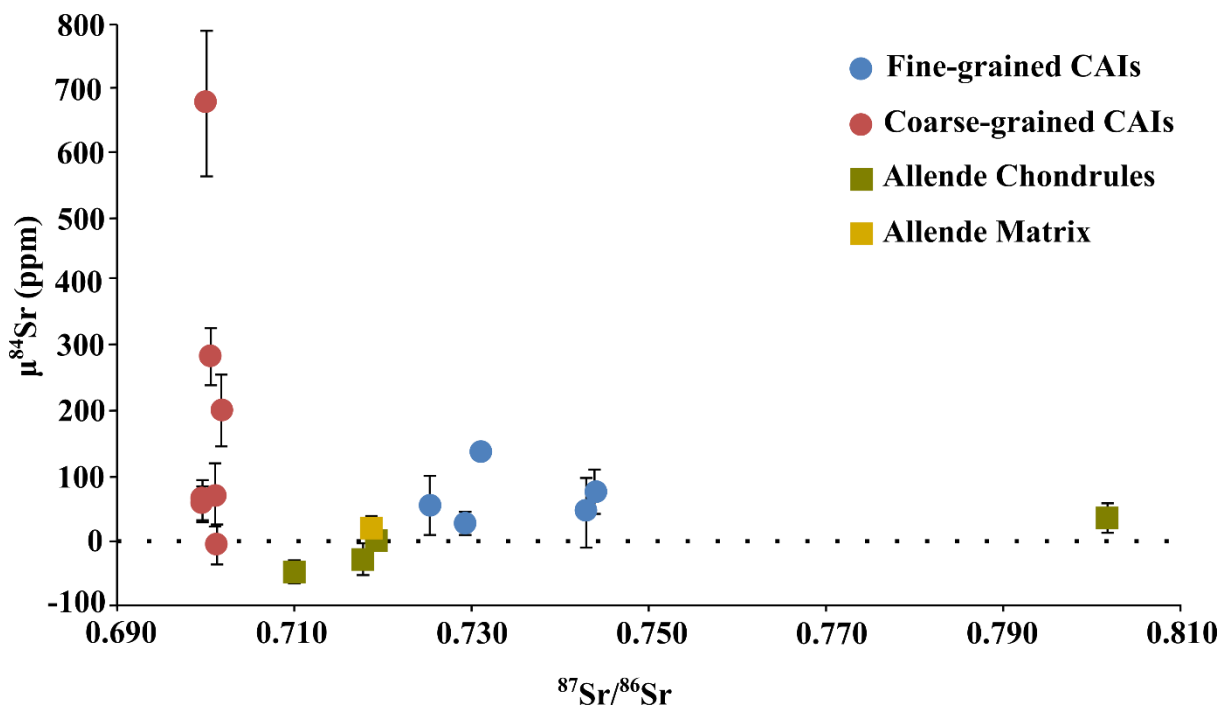


Figure 12- Plot of $\mu^{84}\text{Sr}$ vs. $^{87}\text{Sr}/^{86}\text{Sr}$ for the fine- and coarse-grained CAIs analysed in this study. Data for Allende chondrules and matrix are also included. The standard error in $^{87}\text{Sr}/^{86}\text{Sr}$ is smaller than the markers used. Coarse-grained CAIs possess very restricted $^{87}\text{Sr}/^{86}\text{Sr}$ ratios compared to fine-grained CAIs but span a greater range of $\mu^{84}\text{Sr}$ values, even when excluding CAI30. Differing behaviour between the two may be indicative of fine-grained CAIs experiencing a re-equilibration or homogenisation event.

Further evidence that at least some of the CAIs sampled have been affected by open system processes post-condensation can be found by comparing $^{87}\text{Sr}/^{86}\text{Sr}$ to $\mu^{84}\text{Sr}$ (Figure 12). Generally, coarse-grained CAIs possess less radiogenic $^{87}\text{Sr}/^{86}\text{Sr}$ than fine-grained CAIs, which, as previously noted, typically possess smaller $\mu^{84}\text{Sr}$. These patterns are consistent with the fine-grained CAIs having experienced significant Rb addition relative to Sr during alteration and subsequently evolving more radiogenic $^{87}\text{Sr}/^{86}\text{Sr}$ compositions through ^{87}Rb decay. The exact nature of the alteration these CAIs have undergone can be explored through the comparison of $1/\text{Sr}$

and $^{87}\text{Sr}/^{86}\text{Sr}$ in a mixing diagram (Figure 13). Using this plot, it is evident that the observed Rb-Sr systematics of these CAIs cannot be explained by simple incorporation of matrix materials either in situ on Allende or during the separation processes used in this study, as in most cases the fine-grained CAIs analysed possess more radiogenic signatures than the Allende matrix analysed. Instead, the more likely source of radiogenic Sr in these CAIs is material akin to the large (>3mm) chondrule separate, which possess low Sr concentrations but are highly radiogenic compared to all other chondrules and CAIs analysed from Allende. If material from similar chondrules were incorporated into the analysed fine-grained CAIs then it is also possible that their $\mu^{84}\text{Sr}$ signatures have also been affected. Specifically, as most chondrules possess much smaller excesses or deficits in $\mu^{84}\text{Sr}$ (this study; Dauphas and Schauble, 2016) the fine-grain CAIs in this study may have experienced Sr re-equilibration or homogenisation, explaining the discrepancy between CAI30s large, reported excess and the fine-grained CAIs analysed.

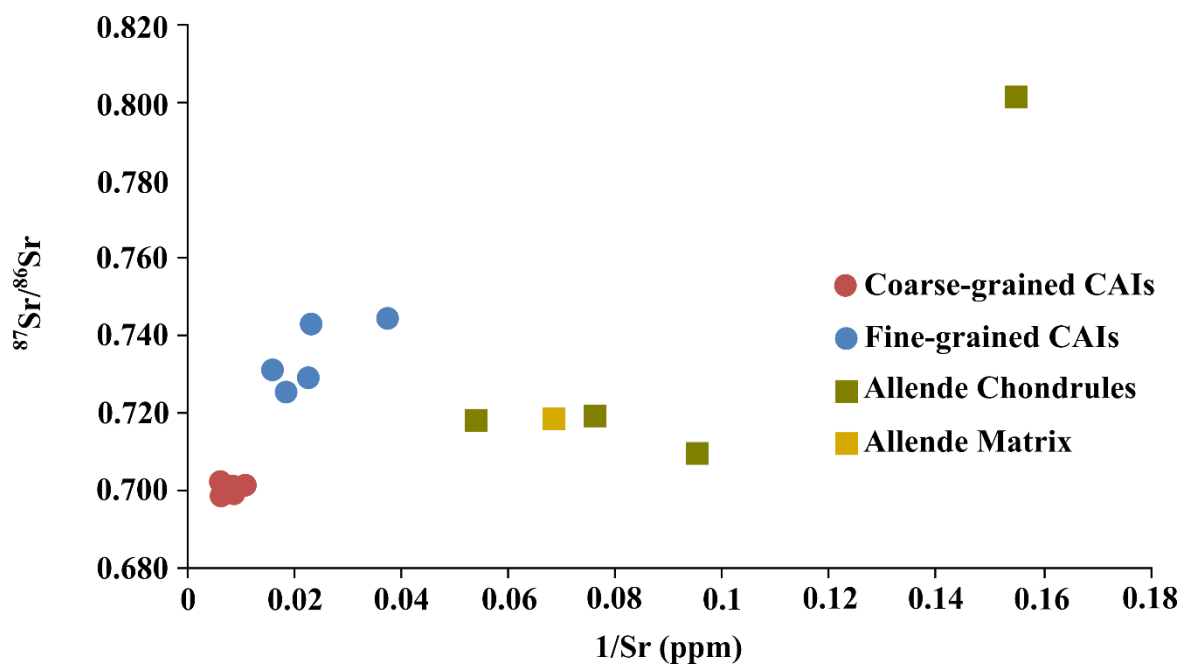


Figure 13- Plot of $1/\text{Sr}$ vs. $^{87}\text{Sr}/^{86}\text{Sr}$ for the fine- and coarse-grained CAIs analysed in this study. Data for Allende chondrules and matrix are also included. The standard error in $^{87}\text{Sr}/^{86}\text{Sr}$ is smaller than the markers used. Radiogenic Sr variations in both sets of CAIs are unlikely to be attributed to matrix or smaller (< 3mm) chondrule incorporation. It is possible that incorporation of coarser-grained chondrules (>3mm) could result in the observed spread of $^{87}\text{Sr}/^{86}\text{Sr}$ in both fine- and coarse-grained CAIs.

In order to further investigate the open system behaviour experienced by these CAIs, we consider the variability in the abundance of Rb and Sr relative to an immobile element, in this case Th after Charlier et al. (2019) (Figure 14). The fine-grained CAIs display a broad correlation between Rb/Th and Sr/Th, as has been observed in previous studies (Charlier et al., 2019). The coarse-grained CAIs analysed here possess relatively lower Rb/Th ratios, which appear to remain low when Sr/Th ratios increase. These data imply that the Rb-Sr distributions between the fine- and coarse-grained CAIs are decoupled, as was predicted by the poor errorchron between $^{87}\text{Rb}/^{86}\text{Sr}$ and $^{87}\text{Sr}/^{86}\text{Sr}$ (Figure 9). Decoupling of Rb and Sr distributions between the two textures may explain why the 3.075 Ga errorchron age is much younger than previous estimates of the timing of alteration for CAIs (e.g., Charlier et al., 2019; MacPherson et al., 2015; Pravdivtseva et al., 2003). It has previously been observed that the Sr/Th ratio in fine-grained CAIs are largely controlled by variations in the

concentration of the fluid-immobile Th (Charlier et al., 2019). The data presented here agrees with this previous observation, with Sr varying by a factor of ~4.5 among fine-grained CAIs while Th varies by a factor of ~16.

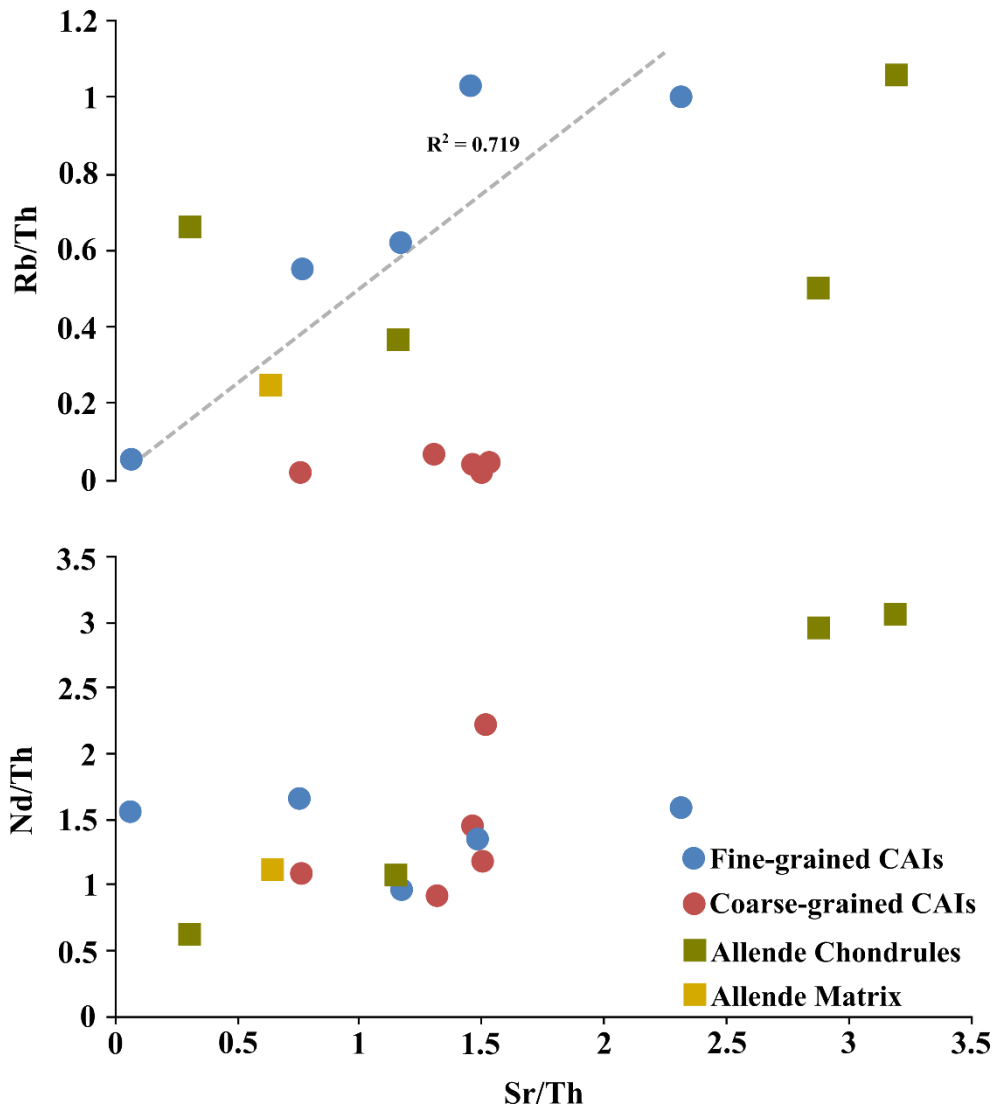


Figure 14- Plots of Nd/Th versus Sr/Th and Rb/Th versus Sr/Th for all the CAIs analysed in this study alongside Allende chondrules and matrix material. All data is normalised to CI chondrites: data values from Table 2; normalising values from Palme and Beer (1993). Uncertainties for all data points are smaller than symbol size. Thorium and Nd data from Bekaert et al. (2021).

An explanation for the broad correlation between Sr/Th and Rb/Th among fine-grained CAIs would be that Rb was added in unequal measure compared to Sr during aqueous, post-condensation alteration but in a relatively constant amount in the fine-grained CAIs, and both the Rb/Th and Sr/Th ratios are driven by variations in the concentration of Th. It is unlikely that these variations in Th are the product of matrix incorporation during sampling as the matrix materials analysed here have lower Rb/Th and Sr/Th than most of the CAIs. The coarse-grained CAIs that are most closely representative of complete refractory element condensation according to their flat type-I or -V REE profiles (e.g., Davis et al., 2018; Figure 6) still have detectable Rb contents that appear to have influenced their present-day radiogenic Sr-isotopic characteristics (Figure 9). Unlike previous studies, the observed variations in Sr/Th for both fine- and coarse-grained CAIs seems to mostly reflect the introduction of Sr during aqueous alteration as there is only a broad correlation between Sr/Th and Nd/Th (Figure 14).

4.4.3 Stable Sr isotope variations

The stable strontium isotopic compositions of the CAIs analysed here are shown on a three-isotope plot (Figure 10) which informs on stable isotopic fractionation processes (e.g., condensation, evaporation and mixing) operating during CAI formation. When compared with bulk undifferentiated meteorite data (+0.32 to -0.09‰; Charlier et al., 2017), and the average terrestrial $\delta^{88}\text{Sr}$ value (+~-0.29‰; Moynier et al., 2012; Charlier et al., 2012) the CAI data extend to both heavier and lighter values for $\delta^{88}\text{Sr}$ (+1.92 to -2.93‰), though tend to be slightly heavier than the data obtained for Allende CAIs in previous studies (+1.69 to -3.64‰; Charlier et al., 2019).

When Sr abundances are ratioed to a refractory element, such as Nd (Figure 15), theoretical considerations for different stable isotopic fractionation process pathways can be explored to study the variations in $\delta^{88}\text{Sr}$, assuming that all discernible isotopic variations are inherited from high-temperature processes (e.g., Charlier et al., 2019). Fine-grained CAIs are asymmetrically distributed towards light $\delta^{88}\text{Sr}$ values, with such enrichments likely the product of kinetic effects during CAI condensation as the kinetic theory of gases predicts that light isotopes tend to impinge on surfaces at a higher rate than heavier isotopes. To a first order, kinetic fractionation can be as large as the square root of the involved isotopes atomic masses, i.e., -11.4‰ for the $\delta^{88}\text{Sr}$, assuming gas supersaturation (Simon and DePaolo, 2010; Dauphas et al., 2015). With no supersaturation, the gas would be in thermodynamic equilibrium with the condensate (i.e., the CAI) and kinetic isotopic fractionation would not occur. The $\delta^{88}\text{Sr}$ values observed in the fine-grained CAIs analysed here reach ~-2.90‰, therefore residual vapour from CAI formation would be enriched in heavier Sr isotopes and subsequent condensation from such a gas may explain the average heavier Sr isotope composition measured in some fine-grained samples. Equilibrium fractionation at the high temperatures involved in CAI condensation is undoubtedly lower than the total range in $\delta^{88}\text{Sr}$ (4.85‰) measured here. We thus conclude that the stable Sr isotopic compositions in the fine-grained CAIs analysed here primarily reflect kinetic isotope effects that occurred during condensation, though there may be some influence of both partial evaporation and/or recondensation post initial formation (e.g., Simon et al., 2017; Charlier et al., 2019). Similar inferences have previously been reached with stable isotope variations for Ti (Davis et al., 2018; Simon et al., 2017) and Ca (Niederer and Papanastassiou, 1984) documented in other CAI samples, primarily from Allende, and attributed to multi-stage condensation, evaporation and recondensation in the early protoplanetary disk.

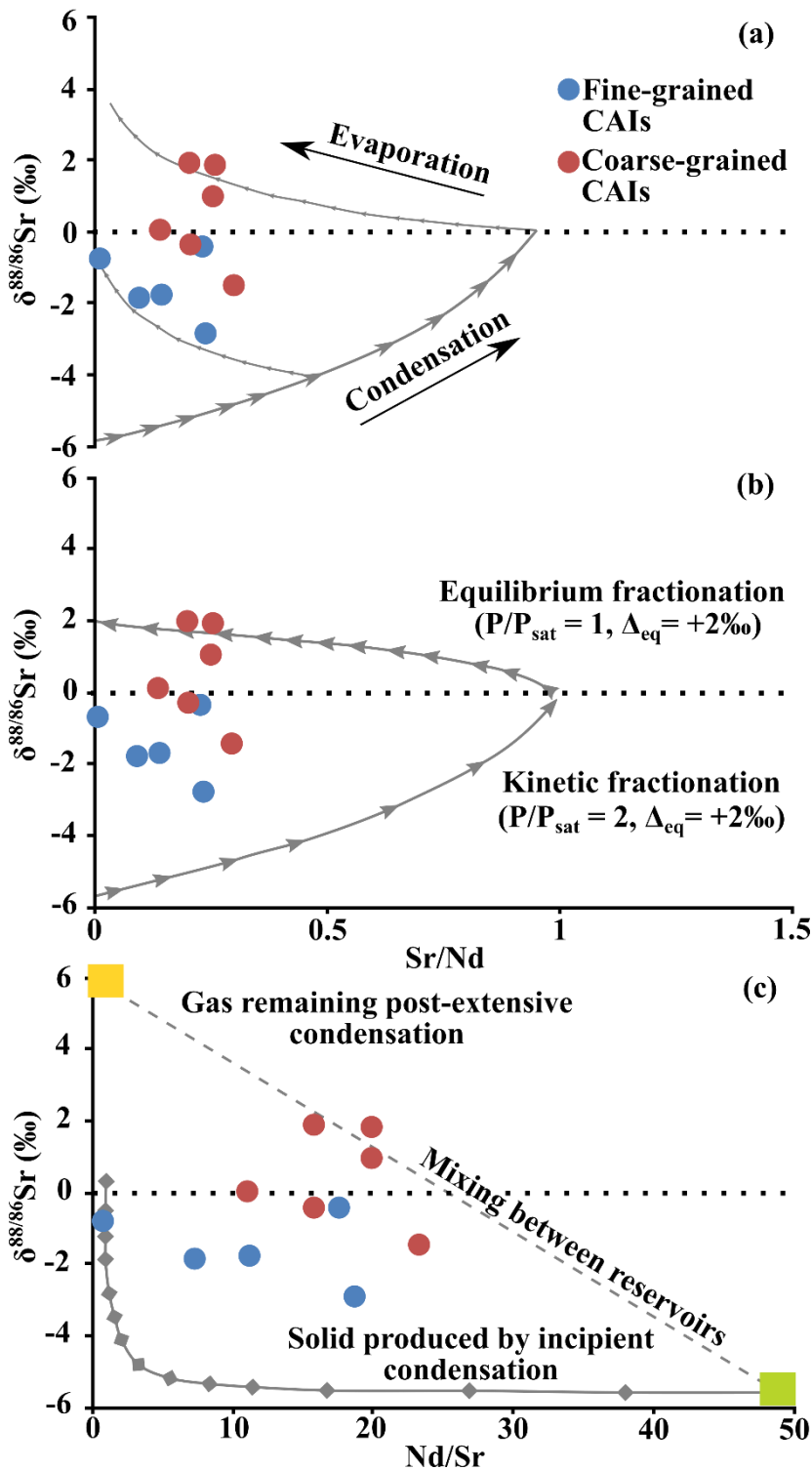


Figure 15- Schematic plots (after Dauphas et al., 2015 and Charlier et al., 2019) illustrating three possible scenarios that could explain stable Sr isotopic fractionation versus the elemental ratio of Sr (moderately volatile) to Nd (refractory) for the fine-grained CAIs analysed. The schematics use the data collected by this study applied to previously generated models (e.g., Dauphas et al., 2015; Charlier et al., 2019). (a) Partial condensation followed by evaporation. Initial condensates will be enriched in lighter Sr isotopes at the expense of heavier isotopes (^{88}Sr) and possess low Sr/Nd ratios. Additional condensation increases Sr/Nd and drives $\delta^{88}\text{Sr}$ towards heavier values (maximum of 0). At any point during these processes, partial condensates can be reheated and evaporated to achieve positive $\delta^{88}\text{Sr}$ values. Two potential paths are depicted. (b) Condensation only under variable gas saturation. The bottom curve represents an oversaturated scenario resulting from undercooling where kinetic fractionation dominates. (c) Condensed solid and gaseous component variable mixing. The black curve is the same condensation curve from the upper panels but note Nd/Sr is now plotted on the x-axis. The first condensed solid which will be enriched in Nd but have very little Sr is represented by the green square; as in panels (a) and (b), the associated $\delta^{88}\text{Sr}$ values will be light. The yellow square represents the residual gas post-extensive condensation (low Nd/Sr, heavy $\delta^{88}\text{Sr}$). Mixing of solids formed along the condensation path with the gas remaining after extensive condensation can generate the full range of data obtained here and in previous studies (e.g., Charlier 2019). The ranges in Sr/Nd and $\delta^{88}\text{Sr}$ values imply that part of the stable isotope variations may reflect processes other than simple gaseous phase condensation.

Plotting elemental Rb concentrations, $\delta^{88}\text{Sr}$ and $\mu^{84}\text{Sr}$ values against Sr concentrations provides a complementary perspective to the previous stable Sr plots. Increasing Sr and Rb concentrations in the fine-grained inclusions accompany a broad decrease in the $\delta^{88}\text{Sr}$ values and a broad increase in $\mu^{84}\text{Sr}$ (Figure 16). Our coarse-grained inclusions do not show the general clustering of $\delta^{88}\text{Sr}$ values reported by Charlier et al. (2019) and instead display a trend towards lighter $\delta^{88}\text{Sr}$ at high Sr concentrations. Such a trend may reflect a

condensation path from a less supersaturated parent gas, favouring the accretion of lighter Sr isotopes (Figure 15b) or may be the result of post-condensation processes that also possess kinetic controls, such as remelting. Unlike in previous studies (e.g., Charlier et al., 2019), the larger scatter observed in $\delta^{88}\text{Sr}$ for fine-grained CAIs seems more likely to be due to aqueous alteration as, as discussed previously in section 4.4.2, (I) Sr does not strongly correlate with Nd in fine grained CAIs and (II) there is a substantial difference in the $\mu^{84}\text{Sr}$ values obtained between fine- and coarse-grained CAIs, with fine-grained inclusions appearing to have their anomalies reduced towards zero when compared to the seemingly aqueously unaltered CAI30. The overall offset MDFL in $\delta^{84}\text{Sr}$ versus $\delta^{88}\text{Sr}$ space measured from the CAI suite analysed here (Figure 10) also does not match those obtained previously by other studies from bulk meteorites (Charlier et al., 2017; Charlier et al., 2019), with most fine-grained CAIs deviating from this line. The likeliest cause of the observed deviation in the MDFL is CAI30 as CAIs with such a large $\mu^{84}\text{Sr}$ have never previously been sampled and such a large excess is likely to cause leverage. Without further sampling it is difficult to state with certainty which of the two lines represents the true MDFL for CAIs as at present it is unknown how abundant CAI30-like CAIs are.

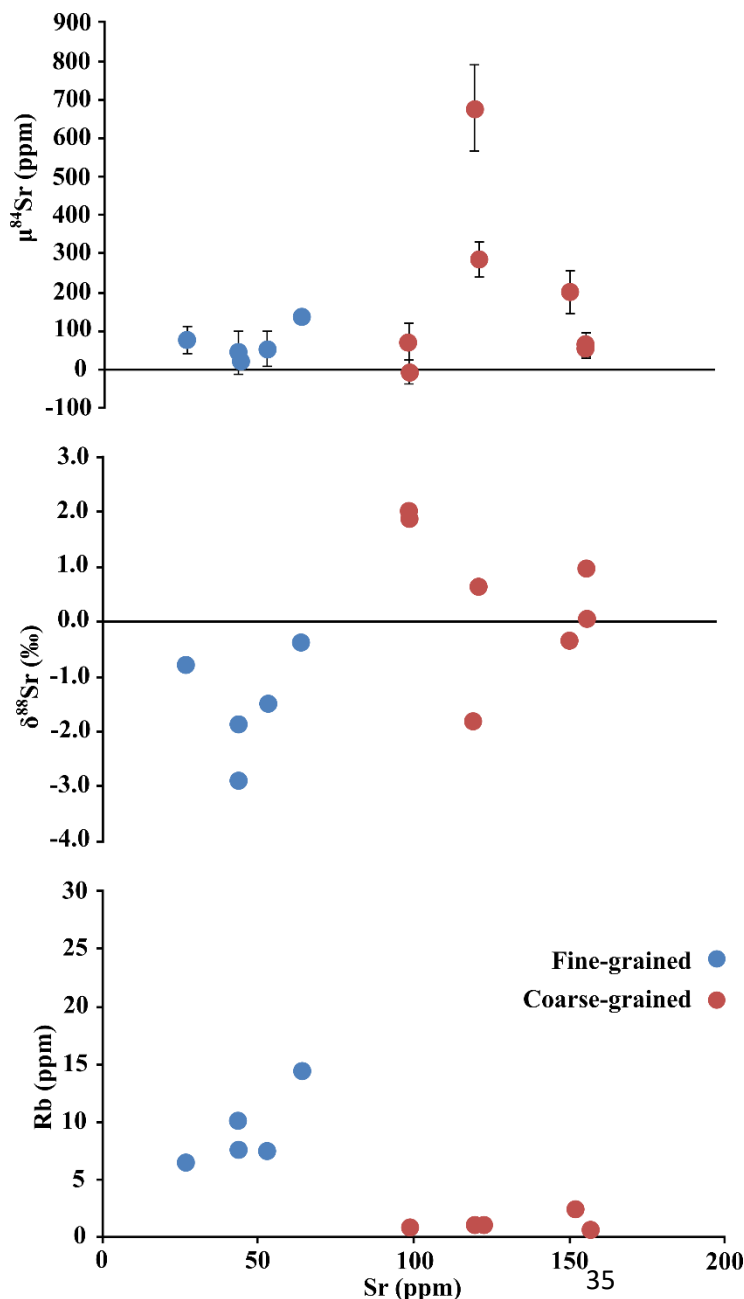


Figure 16- Plots of (a) Rb versus Sr (values shown in ppm and chondrite normalised: data values from Table 1; normalising values from Palme et al., 2014) for CAIs also analysed for stable strontium isotopes (this study; Patchett, 1980a). (b) Double-spike $\delta^{88/86}\text{Sr}$ values versus Sr abundance for our samples and those reported by Patchett (1980a). (c) $\mu^{84}\text{Sr}$ Values versus Sr abundance for our samples. We omit the data of Patchett (1980a) because the reported precision for ^{84}Sr in that paper spans the entire range of values presented here.

4.4.4 Ambiguity of p- versus r-/s-process anomalies in bulk CAIs

The $\mu^{84}\text{Sr}$ values obtained for CAIs here (Figure 7) can be most simply considered to represent an excess in p-process ^{84}Sr . The possibility that there are instead variations in r-process ^{88}Sr that influence the conventional $^{86}\text{Sr}/^{88}\text{Sr}$ ratio (0.1194; Nier, 1938) used for internal normalisation, cannot be uniquely addressed here. As to properly discriminate between these alternatives either the carrier of the nucleosynthetic anomalies in CAIs must be found, or samples must be measured that possesses extremely low $^{87}\text{Rb}/^{86}\text{Sr}$ ratios, for example, CAIs from reduced CV3 materials. In the latter case, such samples would record close to the initial $^{87}\text{Sr}/^{86}\text{Sr}$ ratio (requiring minimal age correction) in order to test the conformity of the double spike-derived $^{87}\text{Sr}/^{86}\text{Sr}$ data to a mass-dependent fractionation line in $^{87}\text{Sr}/^{86}\text{Sr}$ - $\delta^{88}\text{Sr}$ space. Our Rb concentration data is not precise enough for such an approach, however previous studies have attempted to use coarse-grained, Rb-poor CAI double-spike data to address the issue (Charlier et al., 2019). It was concluded that based on their data and previous observations that the canonical $^{88}\text{Sr}/^{86}\text{Sr}$ ratio used for normalisation must be relatively close to the real value and that the observed $\mu^{84}\text{Sr}$ anomalies are most probably caused by variations in ^{84}Sr , reflecting a p-process rather than r-/s-process variability.

4.4.5 Fine-grained versus coarse-grained CAIs

Although the consensus is that CAIs formed in a region close to the proto-sun (e.g., Scott and Krot, 2014; MacPherson, 2019; Bekaert et al., 2021), the distinctive Sr isotopic compositions in three-isotope space and the distinctive $\mu^{84}\text{Sr}$ anomalies (Chapter 6; e.g., Charlier et al., 2017; Charlier et al., 2019) of the fine- and coarse-grained CAIs studied here both display some isotopic affinities with carbonaceous chondrites, which are believed to have formed far from the Sun, beyond the accretion zone of proto-Jupiter. Recent studies of the nucleosynthetic anomalies in Mo isotopes appear to preclude a simple genetic relationship between these two textural classes of inclusions (e.g., Brennecka et al., 2017), however the Sr systematics of the CAIs analysed here suggest that, at least for Allende CAIs, there is a genetic relationship between fine- and coarse-grained variants. Overlapping isotopic anomalies in fine- and coarse-grained CAIs have also been reported previously for Sr (Charlier et al., 2019) and many other isotopic systems including Cr, Ti, Ba, Hf, Sm and Nd (Dauphas and Schauble, 2016 and references therein; Brennecka et al., 2017; Davis et al., 2018; Scott et al., 2018; Shollenberger et al., 2018).

It is currently unclear why fine- and coarse-grained CAIs show similar anomalies in some elements and distinctive anomalies in others however it is possible that differing degrees of thermal processing in their precursor materials could have partially destroyed/ homogenised specific pre-solar grain carriers. A difference in thermal processing has previously been noted in fine-grained CAIs compared to coarse-grained CAIs in terms of the distributions of REE patterns and the larger dispersion in Sr and Ti isotopic compositions in fine-grained CAIs compared to coarse-grained CAIs (e.g., Davis et al., 2018). An alternate hypothesis could be that

some of these elements and isotope systems are more susceptible to post-condensation alteration than others. In terms of the samples analysed here, evidence that aqueous alteration is key to understanding elemental and isotopic differences in fine- and coarse-grained CAIs is evident when comparing CAI30 to the fine-grained CAIs analysed here. Typically, fine- and coarse-grained CAIs have fairly similar $\mu^{84}\text{Sr}$ (this study; Charlier et al., 2019) however CAI30 possesses an extremely large ^{84}Sr excess and, unlike the fine-grained CAIs, shows little evidence of post-condensation alteration (Figures 12 and 13). The previously perceived similarity in fine- and coarse-grained CAI Sr isotope systematics therefore appears to be the product of either aqueous alteration and/or preferential thermal processing of the fine-grained CAIs post-condensation. It is possible such alteration has a significant effect on other isotope systems in fine- and coarse-grained CAIs, however this is currently difficult to speculate on as CAI30 is currently the only CAI sampled from Allende to have such high $\mu^{84}\text{Sr}$ and low $^{87}\text{Rb}/^{86}\text{Sr}$.

4.5 Conclusions

Our high precision isotopic Sr data for fine- and coarse-grained Allende CAIs coupled with Rb-Sr and trace element analyses offers a new perspective on the complex history of Allende CAIs. All fine-grained CAIs analysed here (excluding CAI30) possess group II REE patterns while coarse-grained CAIs possess group I, V, or III REE patterns (Figure 6). A large number of CAIs analysed possess elevated nucleosynthetic $\mu^{84}\text{Sr}$ values with an average of $+141 \pm 375\text{ppm}$ (2 s.d., $n = 12$) across both textural types. Coarse- and fine-grained CAIs have slightly different $\mu^{84}\text{Sr}$ anomalies, defining average values of $+192 \pm 236\text{ppm}$ (2 s.d., $n = 7$), and $+68 \pm 43\text{ppm}$ (2 s.d., $n = 5$), respectively. These values correlate within error to $\mu^{84}\text{Sr}$ values previously obtained for carbonaceous chondrites (e.g., Charlier et al., 2017), which likely originate from the outer solar system, however these values are slightly higher than averages previously obtained from Allende CAIs. This observed deviation in the average nucleosynthetic anomaly is likely the product of CAI30, a coarse-grained CAI that possesses an unusually high $\mu^{84}\text{Sr}$ anomaly. Complimentary Rb-Sr data for the CAIs analysed (Figure 9) suggests that the fine-grained CAIs analysed here have been affected by open-system alteration post-condensation. A possible explanation is that post-condensation these fine-grained CAIs mixed with another early solar system material component that possess lower or negative $\mu^{84}\text{Sr}$ excesses i.e., chondrules, in line with previously published leaching experiments for the CI chondrite Ivuna (Paton et al., 2013). An alternative explanation is that these fine-grained CAIs experienced open-system aqueous alteration as indicated by their Rb-Sr chemistry and the absence of a strong correlation between Sr and Nd.

The double-spike stable Sr CAI data yields an MDFL that is offset with respect to the equilibrium MDFL for differentiated meteorite and terrestrial samples in three-isotope space ($\delta^{88/86}\text{Sr}$ versus $\delta^{84/86}\text{Sr}$) and is not concordant with previously obtained MDFLs for CAIs (Charlier et al., 2019), showing a significant degree of scatter. The scatter observed in the MDFL is likely a result of the presumed aqueous alteration of most of the fine-grained CAIs studied. Fine-grained CAIs are asymmetrically distributed towards light $\delta^{88}\text{Sr}$ values we thus conclude that the stable Sr isotopic compositions in the fine-grained CAIs analysed here primarily reflect

kinetic isotope effects that occurred during condensation, with minimal influence from partial evaporation and/or recondensation post initial formation. Our coarse-grained inclusions do not show the general clustering of $\delta^{88}\text{Sr}$ values reported by previous studies (Charlier et al., 2019) and instead display a trend towards lighter $\delta^{88}\text{Sr}$ at high Sr concentrations, reflecting either a condensation path from a less supersaturated parent gas than the for fine-grained CAIs or possibly the result of post-condensation processes that also possess kinetic controls, such as remelting or susceptibility to aqueous alteration for CAIs with low Sr concentrations. As in previous studies, our data alone is unable to categorically distinguish between p-process anomalies in ^{84}Sr versus r-, and weak and main s-process variability in ^{88}Sr , however previous studies suggest that anomalies likely reside in ^{84}Sr and we support this hypothesis.

5. Ureilites and their Sr isotope evolution

5.1 An introduction to Ureilites

Many meteorite parent bodies are believed to have undergone efficient metal-silicate separation during their formation, often resulting in the formation of a metallic core overlain by a silicate mantle and crust. Magmatic iron meteorites are thought to derive from the cores of these differentiated protoplanet (e.g., Kruijer et al., 2014), while differentiated achondrites are believed to sample silicate domains in these bodies (Mittlefehldt, 2014). Primitive achondrites are derived from planetary bodies that remained incompletely differentiated during their lifetime (Weisberg et al., 2006), with many also believed to represent melt residues that have lost silicate and Fe-Ni-S components to partial melting in varying degrees (Collinet and Grove, 2020; Keil and McCoy, 2018). Ureilites are the second most abundant achondrite sampled by terrestrial impacts (after HEDs); they are considered to be primitive achondrites but are sometimes also classified as differentiated achondrites owing to the high degrees of melting thought to have taken place on the ureilite parent body (UPB).

5.1.1 Ureilite petrography

Ureilites are coarse-grained ultramafic olivine- and pigeonite-rich achondrites, that also contain significant amounts of metal (<5 wt%) and carbon phases (~3 wt%). The defining feature of ureilites compared to other achondrites is their high C content, which is often present as intergranular ‘veins’ of semi-amorphous ‘C-matrix’, euhedral graphite (Berkley and Jones, 1982) and in some cases high-pressure diamond (Goodrich, 1992; Nestola et al., 2020). Ureilites are sub-divided based on their petrology into two groups- main group ureilites (formerly monomict or unbrecciated ureilites), accounting for 95% of ureilites, and polymict ureilites. Petrographically, main group ureilites are in essence extremely depleted peridotites with typical samples possessing around 66% olivine, 30% pyroxenes (mostly pigeonite) and almost negligible feldspars (Mittlefehldt et al., 1998), though rare pyroxene-rich samples have been observed (Rai et al., 2020). On the basis of their silicate mineralogy, main group ureilites are classified into three different types: olivine-pigeonite, olivine-orthopyroxene, and augite-bearing (Goodrich et al., 2004; 2006). Main group olivines commonly possess strong zonation with high MgO rims, ascribed to the late-stage reduction suggested to have occurred during the impact event that likely destroyed the UPB (Warren, 2012), and Fe-rich cores (Fe_{75} - Fe_{97} ; Goodrich et al., 2004) and reduced, almost Fe-free rims (Fe_{84-96} ; Mittlefield et al., 1998; Meteoritical Bulletin). The compositions of the three major pyroxenes present in main group specimens are also variable, with pigeonite between $Wo_{2.5-16.0}En_{71-90}$, orthopyroxene between $Wo_{1.7-5.0}En_{75-88}$ and augite between $Wo_{32-39}En_{52-60}$ (Mittlefehldt et al., 1998). Main group ureilite textures are characterised by large, anhedral olivine and pyroxene grains (~1mm), which meet in triple junctions with curved intergranular boundaries thought to be indicative of equilibrium crystallisation. Some ureilites possess a more mosaic texture characterised by much smaller grains; this texture is believed to be a recrystallisation/shock product as many of these ureilites appear to possess preferred grain orientation within relict domains (Neuvonen et al., 1972).

Polymict ureilites are fragmental and/or regolith breccias that appear chemically indistinguishable from main group ureilites, though typically show evidence for greater degrees of shock (e.g., Goodrich et al., 2004). Lithic clasts in polymict ureilites are typically set in a matrix of smaller mineral fragments believed to mostly derive from main group ureilites; these include olivine, pyroxenes, suessite, carbon phases, chromite, apatite and, unlike main group ureilites, plagioclase (Prinz et al., 1987). Polymict olivines generally have similar chemistry to main group olivines, though a few polymict specimens are known to span a great Fo range than most main groups (Mittlefehldt et al., 1998). Polymict plagioclases tend to span the entire range of compositions from, An₃₀₋₈₀ containing little measurable K₂O (Prinz et al., 1987). Ureilite-like clastic materials thought to originate from the UPB possess a petrographic range from typical main group ureilite-like to basaltic (Cohen et al., 2004) and trachyandesitic clasts (Bischoff et al., 2014). There are often low concentrations of more exotic clasts present in polymict ureilites originating from later formed planetesimals, e.g., ordinary, enstatite and Rumuruti-type chondrites (e.g., Goodrich et al., 2015). The oldest observed clasts in polymict ureilites are thought to be approximately 5 Myr younger than main group ureilites based on Mn-Cr dating (Zhu et al., 2020) and are thought to be related to the impact history of ureilite daughter bodies (UDBs) after the UPBs catastrophic destruction.

5.1.2 Ureilite chemistry

Ureilites typically possess moderate (versus chondrites) siderophile-element depletion (e.g., Rankenburg et al., 2007) with main group ureilites also being depleted in incompatible lithophile elements. In these respects, ureilite bulk chemistry somewhat resembles typical terrestrial peridotites (e.g., Iherzolites and harzburgites) that experienced the removal of a basaltic component during partial melting events on the UPB, as evidenced by the presence of basaltic melt and trachyandesitic clasts in polymict ureilites (Cohen et al., 2004; Bischoff et al., 2014). Ureilites show a wide array of oxygen isotope compositions (e.g., Clayton and Mayeda, 1988; Greenwood et al., 2017), which fall close to the Carbonaceous Chondrite Anhydrous Mineral (CCAM) line (Figure 17) and show a strong negative correlation with bulk ureilite compositions (Clayton and Mayeda, 1988; Downes et al., 2008). The exact significance of the CCAM line correlation remains contentious but has been interpreted to suggest that two component mixing (possibly between the NC and CC reservoirs) may be responsible for the compositional variation observed in the ureilites isotopic and trace element chemistries (Warren, 2011; Rankenburg et al., 2007; Budde et al., 2017).

5.1.3 The ureilite parent body (UPB) and ureilite daughter bodies (UDBs)

The ureilite parent body (UPB) is generally believed to have accreted within <1 Myr post-CAI condensation (Zhu et al., 2020; Desch et al., 2018; Goodrich et al., 2015), possibly as early as 0.6 Myr (Goodrich et al., 2015; Wilson and Goodrich, 2016). However, Hf-W dating of ureilites suggests a younger accretion age for the UPB of 1.6-1.7 Myr based on the mean age of core formation (Budde et al., 2015; Hilton and Walker,

2020). More recent bulk ureilite Mn-Cr dating provides an age of $\sim 0.6 \pm 1.5$ Myr, in line with early accretion of the UPB and an early onset of partial melting and magmatism (Zhu et al., 2020). Ureilite equilibration temperatures estimated using two-pyroxene thermometry range from ~ 1200 to 1280 °C (e.g., Takeda, 1987), while olivine-pigeonite-liquid thermometry (Singletary and Grove, 2003) suggests a slightly broader range of temperatures from ~ 1150 to 1300 °C. Main group ureilites are believed to represent preserved UPB mantle residues formed after the extraction of feldspar rich magmas and sulfur-rich iron melts (e.g., Bischoff et al., 2014; Rankenburg et al., 2008; Barrat et al., 2015; Barrat et al., 2017). Monte Carlo simulations suggest that a compositional gradient existed in the UPB, likely inherited from its accretion, with MgO-rich, low- $\Delta^{17}\text{O}$ material found closer to the core with compositions becoming progressively more FeO-rich and high- $\Delta^{17}\text{O}$ towards the surface (Rai et al., 2020).

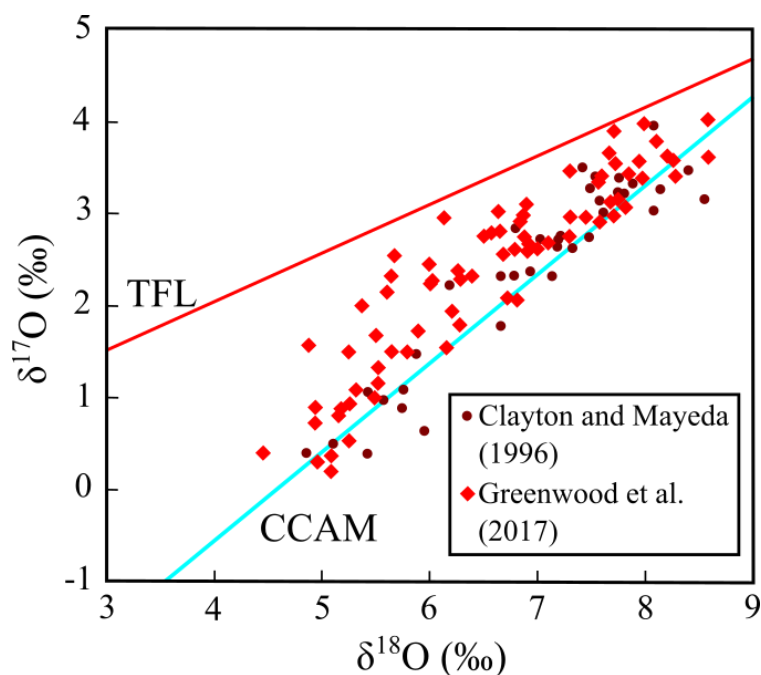


Figure 17- Oxygen isotopic composition of various ureilites measured by conventional methods (Clayton and Mayeda, 1996) and by laser fluorination (Greenwood et al., 2017). Adapted from Greenwood et al., (2017). Abbreviations: TFL: terrestrial fractionation line, CCAM: carbonaceous chondrite anhydrous minerals line (Clayton et al., 1977; Clayton and Mayeda, 1996).

There is significant evidence for magmatism on the UPB, with basaltic and trachyandesitic melts believed to have been produced based on the clastic content of polymict ureilites (Cohen et al., 20004; Bischoff et al., 2014). Despite widespread magmatism on the UPB, ureilites appear to have preserved primordial signatures in light stable isotopes, exhibiting ^{33}S isotope enrichment (Farquhar et al., 2000), and large $\delta^{15}\text{N}$ differences between silicate and carbon phases (Rai et al., 2003a). The isotopic heterogeneity of accreted precursor materials suggests it is unlikely that the UPB underwent complete magmatic equilibration. Previously recorded primitive isotopic evidence from ureilites (e.g., Greenwood et al., 2017; Zhu et al., 2020) suggests that the UPB never experienced a global-scale magma ocean with both O and Cr isotopes possessing primitive heterogeneities that would have been homogenised had such large-scale high degree melting occurred across the UPB (e.g., Zhu et al., 2020; Goodrich et al., 2004; 2015). However, the UPB likely formed a core, albeit to an incomplete extent, i.e., without the efficient melt-silicate separation as that is assumed to have occurred during Earth-style core formation. The UPB is canonically considered to have experienced a significant degree of pressure-dependent carbon redox controlled magmatism (e.g., Goodrich et al., 1987; Walker and Grove 1993) commonly referred to as ‘smelting’. In the UPB ‘smelting’ model, silicate FeO reacts with carbon in the

presence of silicate melt forming Fe-metal and carbon monoxide. The carbon monoxide produced via ‘smelting’ gives rise to rapid, gas-driven localised melt extraction resulting in the loss of melt to space due to high eruption velocities; the presence of such magmatism has previously been proposed to account for the lack of basaltic ureilites sampled to date (Scott et al., 1993).

The exact region of the solar system the UPB originated in is debated, though it is generally believed to have accreted in the inner solar system in proximity to proto-Jupiter before being catastrophically disrupted by a major impact event around 5 Myr post-CAI condensation (Figure 4; e.g., Desch et al., 2019a). The impactors exact origin and geochemical composition is debated (Desch et al., 2019a; Rai et al., 2020), however it likely influenced observed ureilite geochemistry to a degree (e.g., Goodrich and Desch, 2019) particularly observed ureilite noble gas abundance (Amari et al., 2020). It is also possible that some of the diamonds found in ureilites originate from this impactor, however it is more likely that these diamonds are simply the product of impact shock, with their precursor C originating on the UPB itself (e.g., Nestola et al., 2020; Goodrich et al., 2020). No ureilite daughter bodies (UDBs) have been formally identified however 15-Eunomia and its collisional family have been proposed as potential UDBs (Desch et al., 2019b). Polymict ureilites are considered to be derived from the regolith or outer areas of the UPB or the UDBs that reaccreted after the UPBs destruction (e.g., Goodrich et al., 2015).

5.1.4 Nucleosynthetic variations in ureilites

Ureilites have been extensively studied using a variety of metal and volatile isotope systems. Most isotope systems analysed by these studies have focused on core formation (e.g., Hf-W; Budde et al., 2015) and radiometric dating (e.g., Mn-Cr; Zhu et al., 2020), however a few studies have also focused on nucleosynthetic isotopes and other isotope process tracers (e.g., Farquhar et al., 2000; Goderis et al., 2015; Rankenburg et al., 2007). Ureilites are enriched in ^{33}S (Farquhar et al., 2000) and possess largely differing $\delta^{15}\text{N}$ values between both the main C phases present (graphite and diamond) and the dominating silicate phases (Rai et al., 2003a). Such behaviour in S and N isotopes argues against complete magmatic equilibration of the UPB and instead suggests that many isotope systems in ureilites are primitive nebular signatures inherited from the protoplanetary disk during UPB accretion. Existing Mo and Os isotope data provides evidence for excesses in s-process isotopes in ureilites (Goderis et al., 2015; Budde et al., 2017), which complements ureilites lying on an s-process mixing line between an enriched and depleted endmember, as defined by other NC meteorites (e.g., Spitzer et al., 2020).

Specifically, ureilites appear to be more closely related to the s-process enriched endmember (Goderis et al., 2015), however, at present few other elements been analysed for both p- and s-process isotopes making it difficult to distinguish whether this s-process enrichment extends to other elements or simply a feature restricted to Os and Mo isotopes, though s-process enrichment in inner solar system materials has been observed in Nd isotopes (e.g., Burkhardt et al., 2016). Strontium isotopes are therefore a good tool to test

whether ureilites possess s-process isotope enrichment as if ^{86}Sr , ^{87}Sr and ^{88}Sr are enriched via coproduction then deficits in ^{84}Sr are anticipated. This study aims to investigate ureilite s- and p-process systematics through the precise measurement of all the isotopes of Sr in order to clarify the ureilites position on the NC s-process mixing line and by extension the UPBs accretion history.

5.2 Sample preparation and methods

Fourteen bulk ureilite samples were analysed in this study, comprising main group, polymict and dimict ureilites (Table 3); plagioclase and clinopyroxene mineral separates were also taken for analysis from DaG 319. Analytical techniques used in this study follow established methods designed by Charlier et al. (2006), with an emphasis on minimising all possible terrestrial contamination and optimising chemical separation techniques. As Sr in particular is known to be sensitive to arid/desert weathering in meteorites weathering (Braukmüller et al., 2018), all ‘find’ bulk powders were leached in warm ~2 M HCl for 20 minutes, rinsed in MilliQ water and then dried in an oven to remove any possible terrestrial contamination. Samples were dissolved in concentrated HF–HNO₃ (3:1 mixture) at 130 °C on a hotplate, then almost dried down before the addition of aqua regia. Following this, all samples were completely dried down and dissolved in 6M HCl. Aliquots from the initial dissolutions were removed for trace element and Rb and Sr concentration determination via ICP-MS with the remaining portions of the bulk dissolutions converted to nitrate form and internally equilibrated in 8 M HNO₃.

Table 3: A summary of the ureilite samples analysed in this study, their provenance and existing olivine and pyroxene (pigeonite) petrography’s. [1] = MetBase, [2] = Meteoritical Bulletin, [3] = Berkley et al. (1980).

Sample	Classification	Find/Fall	Fa (mol%)	Fs (mol%)	Wo (mol%)	Reference
DaG 319	Ureilite (Polymict)	Find	14.5	-	-	[1]
DaG 801	Ureilite	Find	22.9	20.8	8	[2]
DaG 999	Ureilite (Polymict)	Find	14.3-23.5	14.3-19.3	8.5-4.5	[2]
Dhofar 979	Ureilite	Find	15.8	14.9	5.0	[2]
Dyalpur	Ureilite	Fall	15.7	-	-	[3]
EET 96042	Ureilite	Find	18	-	-	[2]
Hajmah	Ureilite	Find	-	-	-	[2]
NWA 766	Ureilite	Find	24	18.7	-	[2]
DaG 976	Ureilite (Polymict)	Find	25.8	22.7	1.6	[2]
NWA 1241	Ureilite (Dimict)	Find	17	4-22	4-15	[2]
NWA 2082	Ureilite	Find	17.8	15.6	6.2	[2]
NWA 2624	Ureilite	Find	19.6	16.8	2.9-3.8	[2]
NWA 2703	Ureilite	Find	12.3	10.6	5.1	[2]
NWA 3140	Ureilite	Find	13.8	12.1	9.4	[2]

5.2.1 Trace element and isotopic analyses

Major and trace element concentrations were measured on a Thermo XSERIES 2 inductively coupled plasma mass spectrometer (ICP-MS) at Durham University. Internal ‘spikes’ of Re and Rh were added to all samples during their final dilution step before analysis, yielding 20 ppb in solution. Samples were calibrated against a set of international rock standards (BHVO-1, BIR-1, BEN and AGV-1). W2 was further measured as an unknown to ensure the accuracy of the analyses. Analytical precision was within $\pm 5\%$ for all trace elements reported. Strontium separation and mass spectrometry closely follows the methods outlined in chapter three. Instrumental fractionation for natural un-spiked measurements was corrected for using $^{86}\text{Sr}/^{88}\text{Sr} = 0.1194$ (Nier, 1938) to determine the radiogenic $^{87}\text{Sr}/^{86}\text{Sr}$ ratios. The average values and reproducibility of the NBS987 for $^{87}\text{Sr}/^{86}\text{Sr}$ was 0.7102655 ± 46 ($n = 25$). Stable Sr isotope ratios were determined from the raw data for both spiked and un-spiked samples by deconvolving, using the exponential fractionation law and Newton-Raphson iterative sequence in ^{87}Sr denominator space (Albarède and Beard, 2004). Over the period of measurement the external reproducibility on $\delta^{84}\text{Sr}/^{86}\text{Sr}$ (2 s.d.) was 0.028‰, and for $\delta^{88}\text{Sr}/^{86}\text{Sr}$ (2 s.d.) was 0.014‰ (cf. Charlier et al., 2017). Repeat measurement of the rock reference material BHVO-2 yielded values for $^{87}\text{Sr}/^{86}\text{Sr} = 0.703464 \pm 3$ and $\delta^{88}\text{Sr}/^{86}\text{Sr} = 0.266 \pm 0.010\text{‰}$ (2 s.d., $n = 3$) indistinguishable to those obtained by Klaver et al. (2020) of $^{87}\text{Sr}/^{86}\text{Sr} = 0.703476 \pm 7$ and $\delta^{88}\text{Sr}/^{86}\text{Sr} = 0.267 \pm 0.010\text{‰}$ (2 s.d., $n = 6$).

5.3 Results

5.3.1 Trace and rare earth elements

Ureilite REE patterns are divided into three different groups: group-A, B and ALM-A-like (Barrat et al., 2016). Group A and B differ in their heavy and light REE patterns with group A ureilites tending to be more heavily REE depleted and light REE enriched (Barrat et al., 2016), while ALM-A like ureilites possess a flatter REE profile with a pronounced positive Eu anomaly (Bischoff et al., 2014). Ureilite REE chemistry is thought to arise from melt processes as that would be normally associated with restites, however light REE enrichment also correlates with Eu anomalies in ureilites (Barrat et al., 2016) and this has been suggested to indicate that LREE enrichment in ureilites is the result of terrestrial contamination due to post-impact weathering. Group B ureilites are characterised by depletions in large ion lithophile elements (LILE), strong depletions in Zr, P and V and weak depletion in Ti with group A ureilites generally more enriched in LILE and possessing a flatter trace element profile (Barrat et al., 2016). Trachyandesite-like patterns are characterised by significant enrichments in LILE and Zr with a strong depletion in V (Bischoff et al., 2014). The ureilites analysed in this study possess mostly trachyandesite-like REE patterns though all samples appear to have significantly higher enrichments in La compared to the other LREE with five ureilites also possessing significant Lu enrichment (Figure 18). Most ureilites studied here also show no significant Eu anomaly compared to previously analysed ureilites (e.g., Barrat et al., 2016), with only three samples possessing strong positive Eu anomalies. There appears to be a greater diversity of REE patterns in main group ureilites compared to the polymicts, which

display no Eu anomaly and have relatively flat profiles. Three ureilites (DaG 319, NWA 766 and NWA 3140) possess negative Tb anomalies. Trace element patterns for the analysed ureilites (Figure 19) also match more closely to the ALM-A trachyandesite (Bischoff et al., 2014) than group A and B ureilites, with all samples possessing strong Sr and Ba enrichment and Rb depletion. Similar to group B ureilites, all samples analysed here possess strong negative Zr anomalies, though lighter element patterns more closely match the ALM-A trachyandesite or group A ureilites. Both NWA 1241 and DaG319 also possess a strong negative Sc anomaly, which is absent in all main group ureilites analysed here and in all previously analysed samples (Barrat et al., 2016; Bischoff et al., 2014).

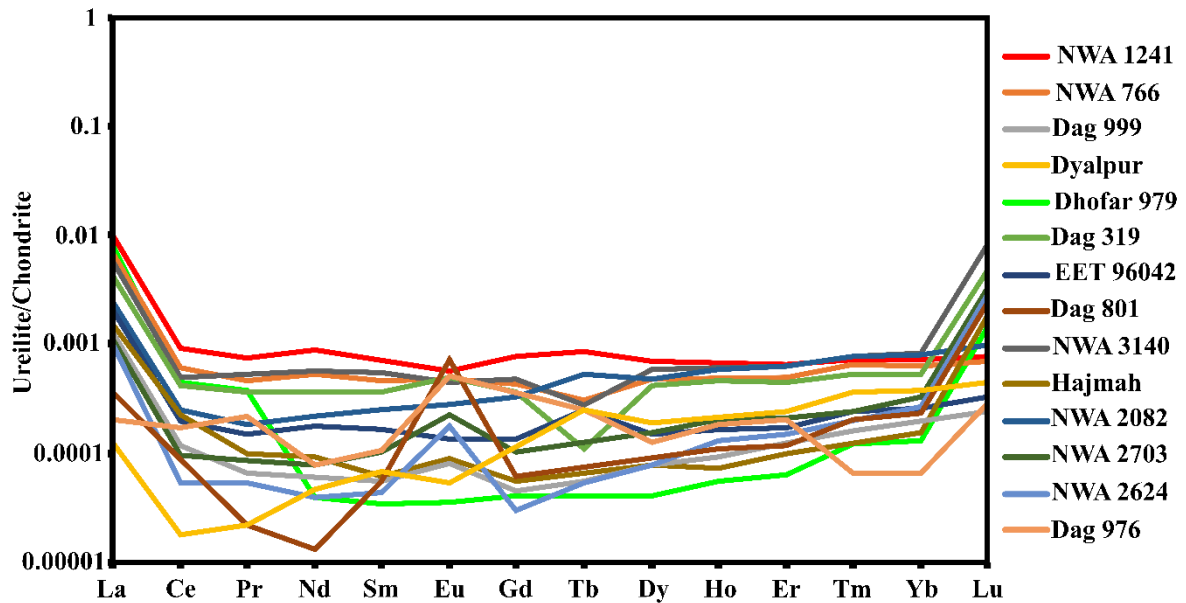


Figure 18- REE patterns for the ureilites analysed in this study. All elements are normalised to CI values (Palme and Beer, 1993). All values are depleted compared to chondrites and all samples possess vastly different patterns to previous studies (e.g., Barrat et al., 2016).

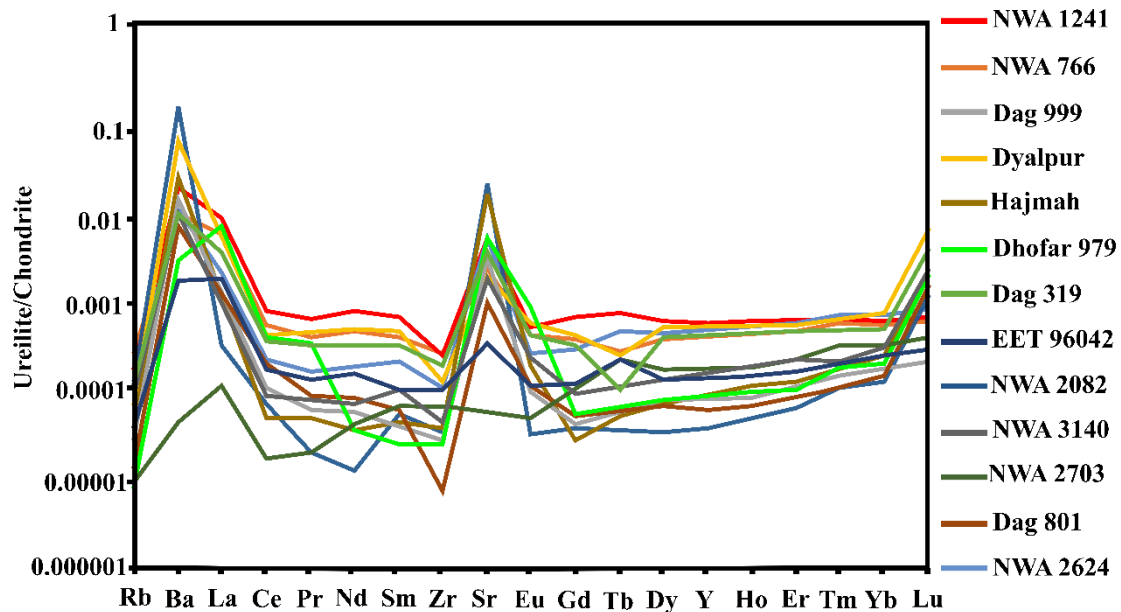


Figure 19- Trace element patterns for the ureilites analysed in this study. All elements are normalised to CI values (Palme and Beer, 1993).

5.3.2 Isotopic data

5.3.2.1 Internally normalised $\mu^{84}\text{Sr}$ data

Strontium has four naturally occurring stable isotopes: ^{84}Sr (0.56%), ^{86}Sr (9.86%), ^{87}Sr (7.00%) and ^{88}Sr (82.58%). All four isotopes have distinct nucleosynthetic origins with ^{86}Sr , ^{87}Sr and ^{88}Sr attributed to s- and r-process synthesis and ^{84}Sr attributed to p-process synthesis; in addition to nucleosynthetic synthesis measured ^{87}Sr also includes a radiogenic component from the decay of ^{87}Rb . This radiogenic component is significant as it means that after internal normalization to $^{86}\text{Sr}/^{88}\text{Sr} = 0.1194$ (Nier, 1938), only the $^{84}\text{Sr}/^{86}\text{Sr}$ ratio can be used to directly assess nucleosynthetic isotopic anomalies. At this point all data was internally normalised to allow direct comparisons with the earlier studies. The internally normalised sample $^{84}\text{Sr}/^{86}\text{Sr}$ ratios are reported here in $\mu^{84}\text{Sr}$ notation (Table 4), which represents the parts per 10^6 deviation from the average $^{84}\text{Sr}/^{86}\text{Sr}$ ratio of NBS987, a Sr isotope standard, measured alongside the other samples in this study. The ureilites analysed in this study possess a wide range of $\mu^{84}\text{Sr}$ values spanning both the NC and CC regions, with eight samples plotting well outside of the NC region possessing large ^{84}Sr deficits (Figure 20). The mean $\mu^{84}\text{Sr}$ for all ureilites analysed is -41.3 ± 56.9 ppm with main group ureilites possessing a mean of -29.4 ± 58.2 ppm and polymict ureilites possessing a mean of -88.9 ± 21.6 ppm. These class averages of many analysed bulk ureilites have resolvable ^{84}Sr deficits compared to terrestrial values, although not all do and are more representative of previous analysed NC meteorites (e.g., Charlier et al., 2017). All polymict samples analysed possess an ^{84}Sr deficit larger than the NC average, with a further four main group ureilites also plotting in this region. NWA 2624 is the only ureilite to plot firmly in the CC average region with all other samples plotting within or straddling the NC average region. Mineral separates separated from DaG 319 were also analysed; both clinopyroxene and plagioclase display ^{84}Sr excess compared to the majority of ureilites analysed, plotting in the CC region, compared to the whole rock deficit of DaG 319, which possesses a much greater ^{84}Sr deficit compared to the NC average.

5.3.2.2 Stable Sr isotope data ($\delta^{88}\text{Sr}$ and $\delta^{84}\text{Sr}$)

Stable strontium isotope compositions are reported here as parts per thousand (‰) deviations from the common Sr reference material NBS987, using the delta notation $\delta^i\text{Sr}$ (Eq.1) where i denotes either ^{84}Sr or ^{88}Sr (Table 5). In three isotope space ($\delta^{88}\text{Sr}$ vs. $\delta^{84}\text{Sr}$) ureilites form a correlation line which spans a range of $\sim 1.0\%$ in $\delta^{88}\text{Sr}$ from -0.59% to $+0.38\%$ (Figure 21). A linear regression for polymict and main group ureilites yields a best fit line with slope -1.2056 ± 0.0127 (2 s.e.), which passes through a x-intercept value of $\delta^{84}\text{Sr} = -0.1514 \pm 0.0552\%$ (2.s.e.). The ureilite data (barring NWA 2082, NWA 2624 and NWA 2703, which are discussed in greater depth in chapter 5.4) obtained deviate significantly from the NC/terrestrial and CC terrestrial lines obtained by previous studies (Charlier et al., 2017; Charlier et al., 2019), which possess slopes of -0.9291 ± 0.0279 (2.s.e.) and -0.8042 ± 0.1327 (2.s.e.) respectively. The slope value of the best fit line presented here corresponds to the theoretical expectation for mass-dependent fractionation which stipulates that the relative

isotopic variations scale as the difference in the absolute masses of the isotopes involved; $(^{84}\text{Sr}-^{86}\text{Sr}) / (^{88}\text{Sr}-^{86}\text{Sr}) \sim -1.0$.

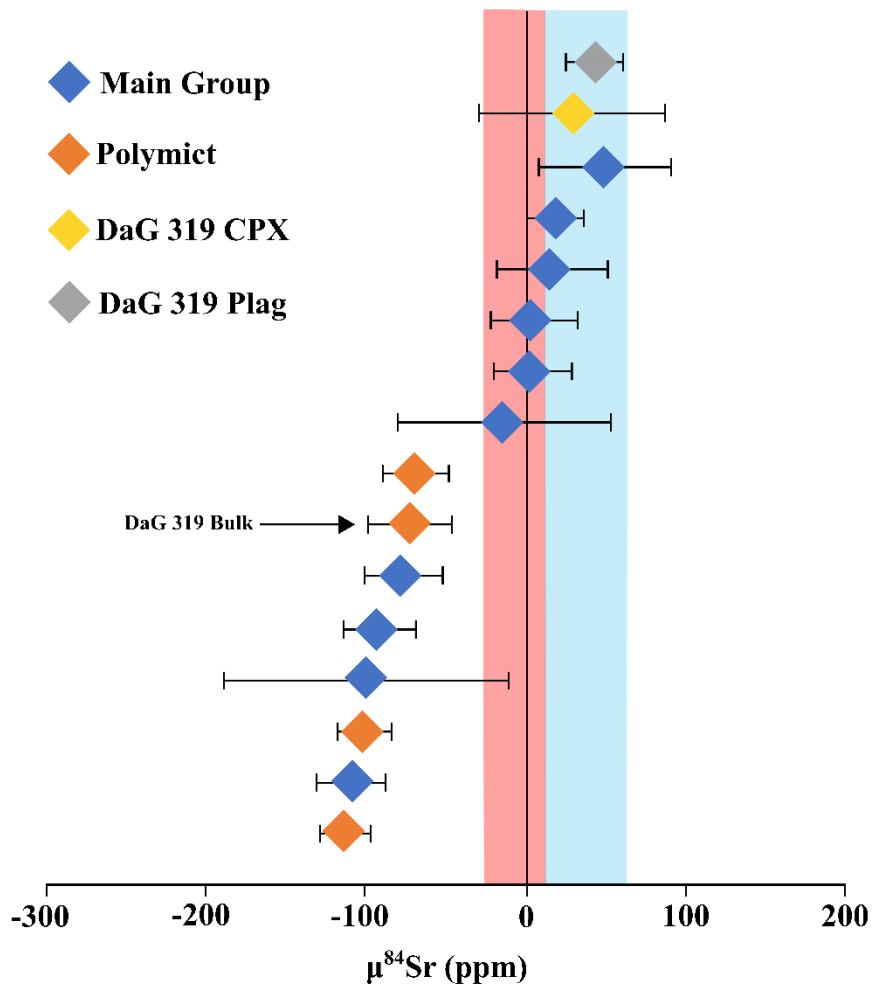


Figure 20- $\mu^{84}\text{Sr}$ plot for ureilites and mineral separates from the polymict ureilite DaG 319. Red and blue bounded regions represent average values for the NC and CC regions of the protoplanetary disk (Charlier et al., 2017).

Table 4- Sr isotopic data obtained for the ureilite samples and mineral separate samples analysed in this study. MG= main group, P = polymict and D = dimict

Sample	NWA 1241	NWA 766	DaG 999	Dyalpur	Hajmah	Dhofar 979	DaG 319	NWA 976
$\mu^{84}\text{Sr}$ (ppm)	-113.48	-109.16	-100.51	-99.14	-91.13	-76.08	-72.19	-69.40
2s.e.	15.70	22.17	17.13	89.24	21.78	23.72	26.63	20.57
$\delta^{84}\text{Sr}$ (‰)	0.0280	-0.2945	-0.0994	0.2981	-0.3004	-0.3410	-0.3229	-0.2051
2s.e.	0.0203	0.0597	0.0222	0.1078	0.0221	0.0606	0.0606	0.0262
$\delta^{88}\text{Sr}$ (‰)	-0.2061	0.1666	-0.0604	-0.5867	0.1805	0.2516	0.2045	0.0786
2s.e.	0.0070	0.0108	0.0077	0.0260	0.0061	0.0092	0.0153	0.0072
$^{87}\text{Sr}/^{86}\text{Sr}$	0.709121	0.712602	0.709734	0.717674	0.708526	0.708407	0.710951	0.708953
$\pm 2\text{sd}$	0.0000025	0.0000032	0.0000027	0.0000103	0.0000026	0.0000058	0.0000067	0.0000031
Sample	EET 96042	NWA 2082	NWA 3140	NWA 2703	DAG 801	NWA 2624	DAG 319 (cpx)	DAG 319 (plag)
$\mu^{84}\text{Sr}$ (ppm)	-13.27	4.11	5.17	17.21	18.98	49.35	29.22	42.74
2s.e.	66.92	24.25	26.55	34.97	18.16	41.42	58.42	17.90
$\delta^{84}\text{Sr}$ (‰)	0.1035	-0.0630	-0.3781	-0.0864	-0.1727	-0.0581	-0.2604	-0.3839
2s.e.	0.1133	0.0608	0.0308	0.0447	0.0316	0.0539	0.0682	0.0208
$\delta^{88}\text{Sr}$ (‰)	-0.2934	0.0052	0.3058	0.0414	0.0200	0.0419	0.1672	0.2944
2s.e.	0.0790	0.0136	0.0074	0.0131	0.0102	0.1126	0.0094	0.0055
$^{87}\text{Sr}/^{86}\text{Sr}$	0.709310	0.709710	0.709637	0.711028	0.708932	0.717674	0.711200	0.704246
$\pm 2\text{sd}$	0.0000087	0.0000066	0.0000038	0.0000049	0.0000038	0.0000057	0.0000075	0.0000025

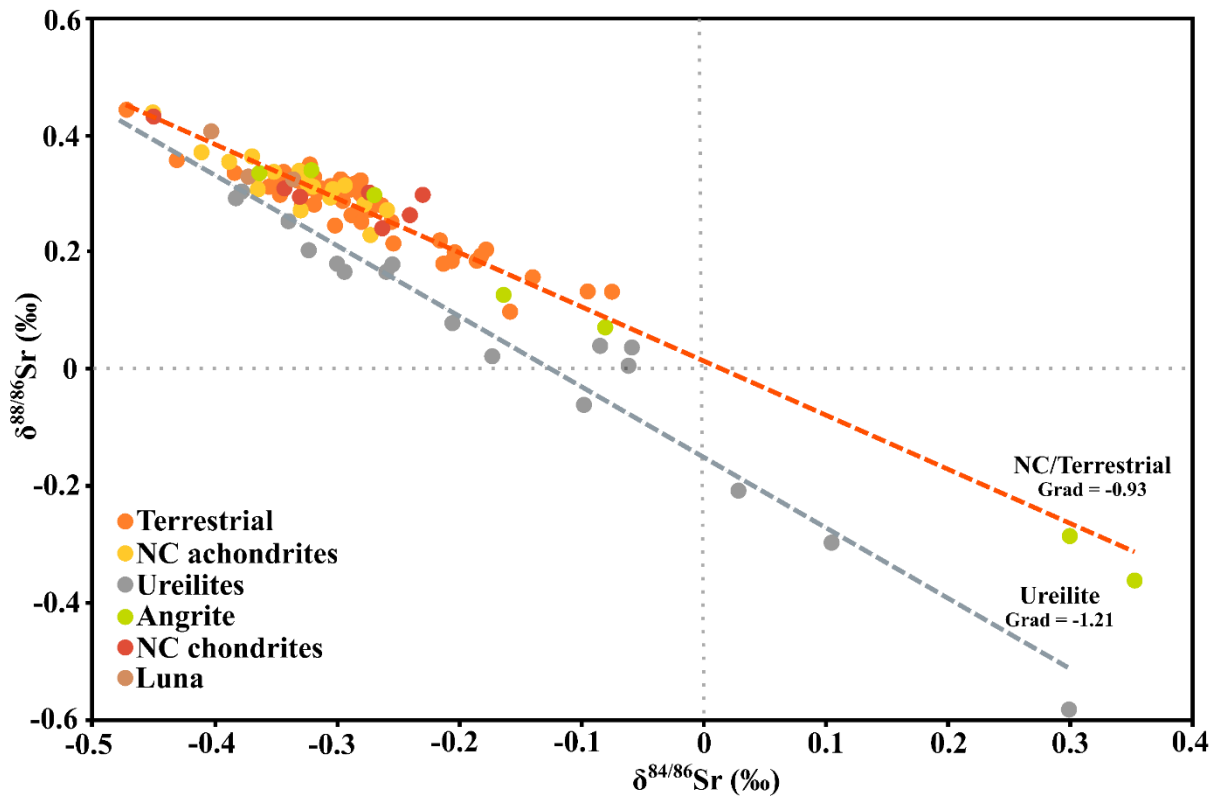


Figure 21- $\delta^{88/86}\text{Sr}$ vs $\delta^{84/86}\text{Sr}$ plot for ureilites and NC (Charlier et al., 2017). Ureilites lie on a significantly distinct correlation line from other inner solar system and terrestrial materials. Three ureilites (NWA 2082, NWA 2624 and NWA 2703) deviate significantly from this line and are positioned between the NC/terrestrial line and the ureilite line suggesting the possibility of mixing between the two trends or contamination of these three ureilites by terrestrial materials after impacting Earth, possibly via hot, dry desert weathering (Barrat et al., 2016).

5.3.2.3 Internally normalized $^{87}\text{Sr}/^{86}\text{Sr}$ and $^{87}\text{Rb}/^{86}\text{Sr}$ data

The observed ^{87}Sr variations in ureilites are primarily controlled by ^{87}Rb decay ($T_{1/2} = 49.624$ Gyr; Rotenberg et al., 2012), with ^{87}Sr produced by decay dominating over possible nucleosynthetic and/or mass dependent variations in observable ^{87}Sr abundances. Both main group and polymict ureilites have relatively radiogenic $^{87}\text{Sr}/^{86}\text{Sr}$ ranging from 0.70841-0.71767 and 0.70912- 0.71095 respectively (Figure 22). Main group ureilites analysed by previous studies show $^{87}\text{Rb}/^{86}\text{Sr}$ ratios ranging from 0.04028- 2.11460, with a mean value of 0.55958 (Barrat et al., 2016), while main group ureilites studied here possess a much narrower range between 0.00028-0.18688. Polymict ureilites $^{87}\text{Rb}/^{86}\text{Sr}$ ratios vary over a much smaller range between 0.007386-0.05134. A best fit line of main group ureilite data yields an initial $^{87}\text{Sr}/^{86}\text{Sr}$ for the UPB of 0.7104700, while polymict ureilite data yields an initial $^{87}\text{Sr}/^{86}\text{Sr}$ of 0.7091181. Linear regression of main group ureilite data yields an initial $^{87}\text{Sr}/^{86}\text{Sr}$ of 0.7104700 and an age of 3396.9 Myr post CAI condensation, while polymict ureilite data yields an initial $^{87}\text{Sr}/^{86}\text{Sr}$ of 0.7091181 and an age of 2596.4 Myr. Both of these ages are substantially different to the accretion and core formation ages of the UPB, which date ureilites at 0.6 ± 1.5 Myr and 1.6-1.7 Myr respectively (Zhu et al., 2020; Budde et al., 2015; Hilton and Walker, 2020). Larger dating discrepancies coupled with significant variations from the $^{87}\text{Rb}/^{86}\text{Sr}$ - $^{87}\text{Sr}/^{86}\text{Sr}$ best fit line suggest that not all analysed ureilite samples in this suite possess primary elemental and isotopic signatures. The ages obtained suggest that, at least, some of the samples have experienced open system behaviour of Rb and/or Sr,

though coupling of this information with the stable isotope variations might reveal which samples have been most significantly affected.

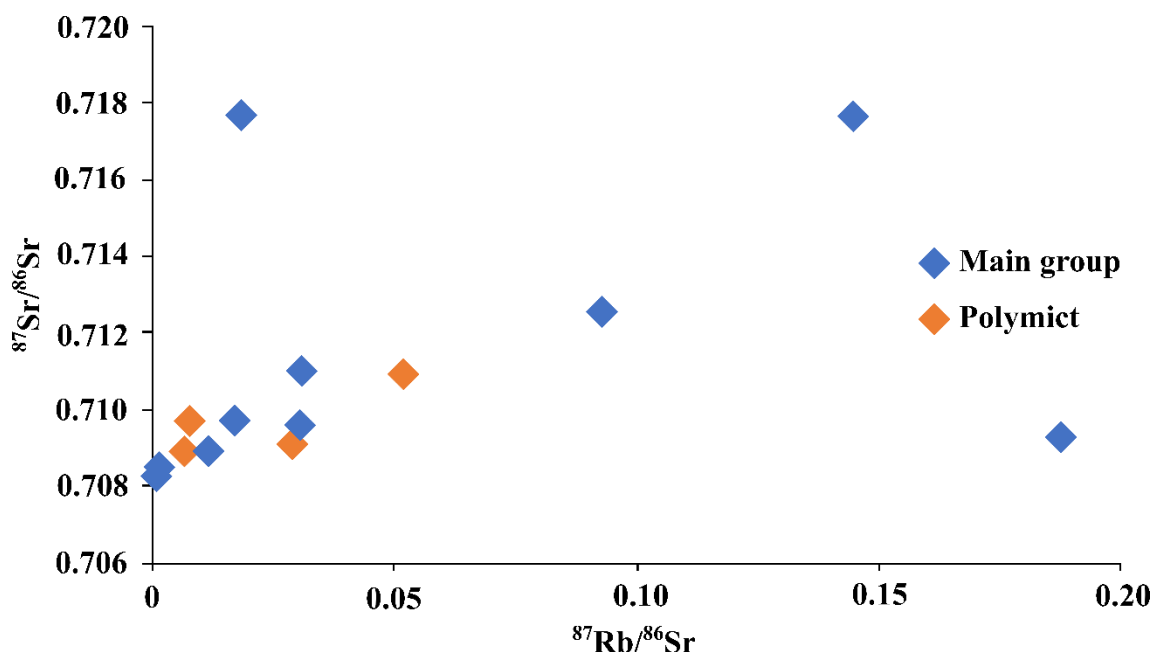


Figure 22- A $^{87}\text{Rb}/^{86}\text{Sr}$ - $^{87}\text{Sr}/^{86}\text{Sr}$ plot for the main group and polymict ureilites analysed by this study.

5.4. Discussion

5.4.1 Rare earth element and trace element systematics in ureilites

Both the main group and polymict ureilites analysed in this study appear to possess REE and trace element profiles unlike those previously obtained in recent studies (e.g., Barrat et al., 2016); instead most ureilites in this study possess relatively flat profiles with a pronounced positive or no Eu anomaly (Figure 18) that appear similar to older ‘v’-shaped profiles obtained for ureilites such as Novo Urey, Kenna, Goalpara and Haveró (Wänke et al., 1972; Guan and Crozaz, 2000). Over the past few decades there has been significant debate over the significance of these profiles and whether they represent true primary LREE enrichment of ureilites (e.g., Boynton et al., 1976) or secondary enrichment either via metasomatism on the UPB/UDBs or terrestrial contamination (e.g., Barrat et al., 2017; Guan and Crozaz, 2000). More recent studies tend to favour the latter explanation for LREE enrichments in the ureilites as many samples are finds rather than recorded falls and are more susceptible to terrestrial contamination especially in hot, arid conditions (Barrat et al., 2017) and this readily explains the LREE enrichment of samples like Novo Urei (Guan and Crozaz, 2000). The range of profiles obtained here may therefore be the product of varying degrees of terrestrial contamination, though this does not explain the presence of positive Eu anomalies and is not supported by the Sr isotopic data here (Figures 19 and 20), which should be more sensitive to terrestrial alteration compared to the REE. There are also examples of ureilites recovered shortly after their fall which possess ‘v’-shaped REE profiles such as Haveró, therefore, while likely that some samples experience a degree of terrestrial contamination on impact, such contamination is unlikely to be the only control on LREE distribution in ureilites.

Assuming that terrestrial contamination of the ureilites has a minimal impact on REE systematics, then the likelihood that LREE and HREE enrichment/MREE depletion is a primary feature of ureilites seems more likely. However, the exact origin of the profile possessed by most of the samples analysed here and in previous studies is not obvious, especially as ureilite olivines and clinopyroxenes are known to possess LREE-depleted, HREE-enriched profiles (Guan and Crozaz, 2000). Previous studies have additionally ruled out the possibility that Sr-rich mineral phases such as phosphate could host the ureilite LREE enrichment and instead favour surface-sited interstitial carbonaceous ureilitic materials as the primary host of LREE enrichments (e.g., Guan and Crozaz, 2000; Goodrich and Lugmair, 1995; Goodrich et al., 1995). These enrichments in interstitial materials have previously been ascribed to either terrestrial contamination of the ureilites (e.g., Barrat et al., 2016; Guan and Crozaz, 2000) or to metasomatism on the UPB (e.g., Goodrich et al., 1995), however as demonstrated by the $\delta^{88}\text{Sr}$ data obtained by this study most of the ureilites (analysed here) appear to possess no significant evidence of isotopic terrestrial contamination of a more labile element. Therefore, it is likely that the 'v'-shaped REE profile possessed by many ureilites is primary.

It is possible that LREE-depleted profiles (Barrat et al., 2016) are also a primary ureilite feature and that the two are products of the various magmatic processes on the UPB or differing degrees of metasomatism either on the UPB or UDBs. It is difficult to determine which of these scenarios is more viable as magmatic processes that operate in possible terrestrial analogues that possess similar 'v'-shaped REE profiles e.g., harzburgites, are poorly understood (Lesnov et al., 2010; Tilhac et al., 2021). However, it should be noted that a single magmatic process has been proposed to account for LREE-enrichment in harzburgites, which possess pyroxenes with LREE-depleted profiles, in which enrichment occurs in the intergranular space of the rocks and in the edge zones of clinopyroxene grains, while no inner zones of the grains were enriched (Niu, 2004), though the exact identity and nature of this processes remains elusive. Alternatively, evidence for significant metasomatism on the UPB is mixed and based on studies that predate the ureilite smelting concept (e.g., Guan and Crozaz, 2000; Goodrich et al., 1995). A few modern studies indicate that ureilite-fluid interactions on the UPB during magmatism were possible though it appears likely that the fluid phase was dominated by $\text{H}_2\text{-CH}_4\text{-H}_2\text{S-S}_2$ rather than H_2O (e.g., Langendam et al., 2021). In most terrestrial harzburgite examples 'v'-shaped REE profiles are considered to be the product of metasomatism (Lesnov, 2010; Tilhac et al., 2021), however it is largely believed that most metasomatic processes in arc and fore-arc settings are believed to occur under oxidising conditions (e.g., Debret et al., 2020), though a few studies have argued for more reducing conditions that would better approximate UPB-like metasomatism (e.g., Piccoli et al., 2019). Without further work on terrestrial and ureilite samples, neither scenario can be currently ruled out.

5.4.2 Nucleosynthetic anomalies in ^{84}Sr

In order to compare our $\mu^{84}\text{Sr}$ values with previously published data the difference between each of the internally normalised $^{84}\text{Sr}/^{86}\text{Sr}$ sample values and the average value for the NBS987 standard was calculated.

However, as discussed in Chapter 4.4.1, using a fixed $^{86}\text{Sr}/^{88}\text{Sr}$ ratio for internal normalisation creates the possibility that if nucleosynthetic anomalies lie in other isotopes then they would be concealed, and the ^{84}Sr data themselves do not allow this to be unambiguously resolved. As previously, the data here are corrected for mass fractionation using the exponential law. As mentioned in Chapter 5.3.2.2, the ureilites analysed in this study record significant mass-dependent fractionation forming a correlation line distinct from the terrestrial/NC line and the CC line (Figure 21). If the natural mass-fractionation experienced by the analysed ureilites does not follow the exponential law, the correction applied to the collected data could produce spurious isotopic anomalies, particularly where $^{88}\text{Sr}/^{86}\text{Sr}$ fractionation is large as this effect would be comparable to $\delta^{26}\text{Mg}$ and ^{26}Al - ^{26}Mg systematics (e.g., Kita et al., 2013), and Ni isotopic anomalies (e.g., Tang and Dauphas, 2012) in early solar system materials. Across both ureilite types there is a general trend that samples that possess heavier $\delta^{88}\text{Sr}$ also possess $\mu^{84}\text{Sr}$ excess, nevertheless there is no significant correlation between $\delta^{88}\text{Sr}$ and $\mu^{84}\text{Sr}$ within the main group ureilite data (Figure 23).

The total range in $\delta^{88}\text{Sr}$ is $\sim 1.0\text{‰}$ (-0.59‰ to $+0.38\text{‰}$); over this range, many of the analysed ureilites are resolvably offset from $\mu^{84}\text{Sr} = 0$, regardless of any mass-dependent fractionation they have experienced. A lack of $\mu^{84}\text{Sr}$ - $\delta^{88}\text{Sr}$ correlation would be expected if $\mu^{84}\text{Sr}$ was a primary feature inherited from disk materials during UPB accretion, as $\mu^{84}\text{Sr}$ values would almost certainly be unaffected by magmatic fractionation processes and therefore could only be significantly altered by mixing between ureilite material and a reservoir with either ^{84}Sr enrichment or depletion. On the other hand, ^{88}Sr is potentially susceptible to fractionation during magmatic processes (e.g., Charlier et al., 2012; Amsellem et al., 2018), however as the ureilites lie on an MDFL in $\delta^{84}\text{Sr}$ - $\delta^{88}\text{Sr}$ isotope space (Figure 21) it is possible that direct isotope fractionation may not be significant; instead, as with ^{84}Sr , ^{88}Sr variations could be a primary product, inherited from accreted disk materials. However, considering the ureilites REE and trace element chemistry coupled with the available isotopic data isotopic reservoir mixing as a part of magmatic processing appears to be the more likely scenario. Polymict ureilites appear to also be the product of isotopic reservoir mixing possessing a strong $\mu^{84}\text{Sr}$ - $\delta^{88}\text{Sr}$ correlation; however, in the case of polymict ureilites, multiple potential reservoirs should be considered as they represent a mixture of main group, non-ureilite, UPB regolith and UPB surface materials, which possess similar $\delta^{88}\text{Sr}$ but possess vastly differing $\mu^{84}\text{Sr}$. Many of the ureilites analysed fall in the depleted $\mu^{84}\text{Sr}$ region, with a large number of samples plotting well outside of the mean NC field (Figure 24).

Ureilite behaviour is, therefore, unlike almost any other NC sample analysed, as almost all other NC bulk meteorites lie within the mean NC field. The clinopyroxene and plagioclase mineral separates from DaG 319's matrix possess small $\mu^{84}\text{Sr}$ excesses consistent with most NC meteorites and materials, though the clinopyroxene value is somewhat indistinguishable from terrestrial values, within uncertainty. Both mineral separates could therefore be alternatively derived from other NC materials inherited by DaG 319, probably in situ on a UDB rather than being derived from ureilite materials. Nevertheless, as these two minerals plot on the ureilite MDFL (Figure 20) it is most likely that they are derived from ureilites. Based on the $\mu^{84}\text{Sr}$ - $\delta^{88}\text{Sr}$ data available here it is therefore probable that ureilites represent mixing between NC-like materials and an as

yet unidentified ^{84}Sr depleted reservoir. One material that could possibly represent this unidentified reservoir is SiC; these grains are thought to have four distinct isotopic profiles in Sr based on their solar origin-mainstream grains, X0 grains, X1 grains and X2 grains (Liu et al., 2015; Stephane et al., 2018). A combination of these grain types could be used to reproduce the range in $\mu^{84}\text{Sr}$ - $\delta^{88}\text{Sr}$ observed in both main group and polymict ureilites when mixed with NC and CC-like materials that would have populated the early protoplanetary disk around the time of UPB accretion (Desch et al., 2018).

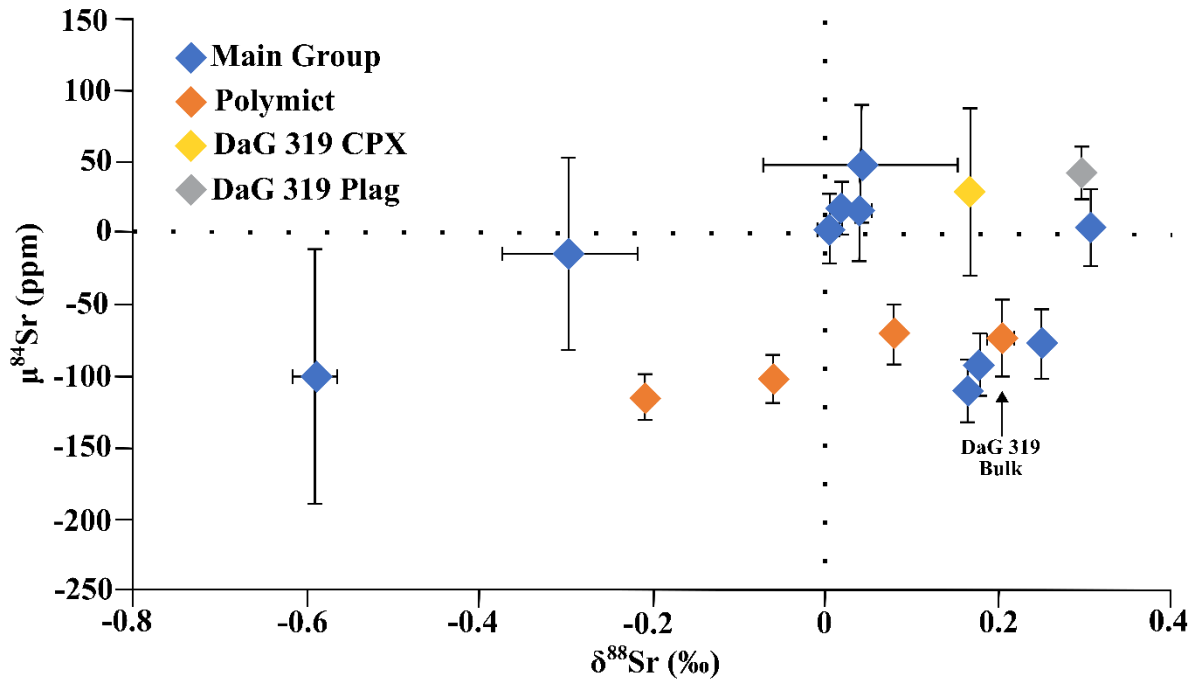


Figure 23- A plot of $\mu^{84}\text{Sr}$ against $\delta^{88}\text{Sr}$ for the main group and polymict ureilites analysed in this study. Measurements of clinopyroxene and plagioclase from DaG 319 are also included.

5.4.3 Stable Sr isotope variations

The stable strontium isotopic compositions of the ureilites analysed here are shown on a three-isotope plot (Figure 21), which informs on stable isotopic fractionation processes (e.g., magmatic and hydrothermal fluid processes on the UPB) operating during the UPBs lifetime and/or subsequent contamination on UDBs and/or the Earth. Ureilite data spans a greater $\delta^{88}\text{Sr}$ range (-0.59‰ to +0.38‰; Table 5) than that observed, thus far, for differentiated meteorites (-0.09‰ to +0.44‰; Charlier et al., 2017), bulk undifferentiated meteorites (+0.24 to +0.43‰; Charlier et al., 2017), and terrestrial materials (+0.134‰ to +0.446‰; Charlier et al., 2017). Average ureilite $\delta^{88}\text{Sr}$ compositions also tend to be much lighter (+0.011 ± 0.24‰) than terrestrial materials (+0.29 ± 0.07‰; Moynier et al., 2012; Charlier et al., 2012) and bulk differentiated meteorites (+0.30 ± 0.011‰; Charlier et al., 2017). Ureilite $\delta^{84}\text{Sr}$ values are typically lower than NC/terrestrial and CC materials for a given $\delta^{88}\text{Sr}$ value; consequently, the majority of ureilite samples lie on a distinct slope away from the terrestrial MDFL and the offset MDFL defined by the CAIs and CC meteorites (Figure 21). Three ureilite samples, however do not fall on this distinct line (NWA 2624, NWA 2082 and NWA 2703). These three ureilites instead plot between the terrestrial and ureilite MDFLs, suggesting they may have been contaminated either by chondritic materials on their UDB or by terrestrial materials post-impact on Earth, or that Sr of a

different nucleosynthetic origin is not uniformly mixed into all ureilite material. Of the two scenarios, terrestrial contamination is favoured as all three are recorded as finds in north-western Africa and would have been very susceptible to hot-dry desert weathering (Barrat et al., 2016). Due to the likely possibility that NWA 2624, NWA 2082 and NWA 2703 have experienced terrestrial contamination they are excluded from further discussion in this chapter in regard to their stable and radiogenic isotope data.

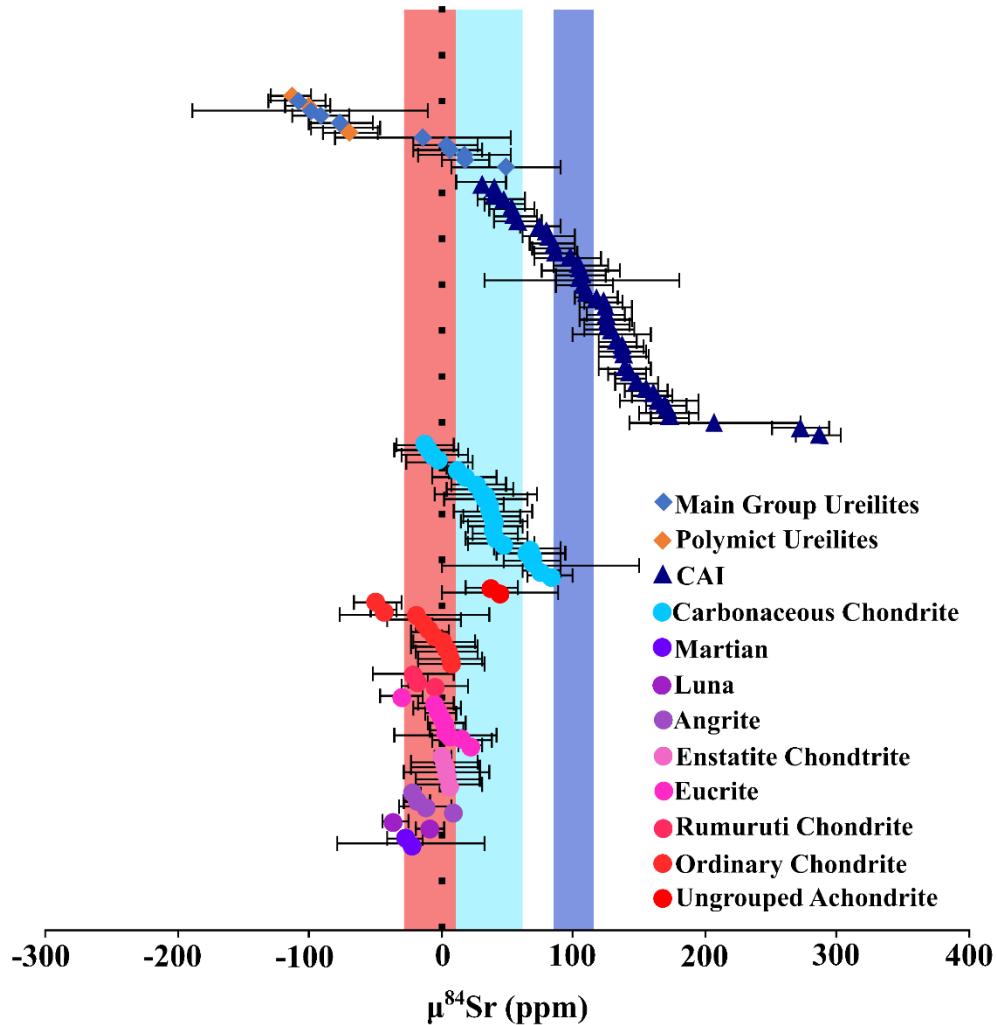


Figure 24- $\mu^{84}\text{Sr}$ data for ureilites, CAIs, NC and CC meteorites. None ureilite NC and CC meteorite data is obtained from previous studies (Charlier et al., 2017).

It is surprising that the ureilites appear to possess a distinct mixing line compared to the terrestrial/NC line as bulk meteorite data for other achondrites maps on to it extremely well (Charlier et al., 2017; Figure 21). There are three plausible explanations for the ureilites possessing their own MDFL. Firstly, the ureilite MDFL could represent a true NC/inner solar system MDFL and the current NC/terrestrial MDFL is the product of sampling bias in terrestrial samples which should represent a mixture between the CC and NC MDFLs based on how the two parts of the disk are believed to have sampled infalling material in the early solar system. This is plausible but highly unlikely due to how well NC chondrites and achondrites both plot on the terrestrial MDFL and their similar mean $\delta^{88}\text{Sr}$ and $\mu^{84}\text{Sr}$ compositions (Charlier et al., 2017). The other explanations for a unique ureilite MDFL rely on both magmatic processes being active on the UPB, namely fractional crystallisation and partial melting (e.g., Collinet and Grove, 2020), and that sampled ureilites are the product of magmatic mixing

between a NC-like and ^{84}Sr -poor reservoir. The effects of both fractional crystallisation and partial melting on ureilite Sr isotope compositions were modelled under a variety of conditions (Figure 25). Fractional crystallisation or melting can produce lighter ^{88}Sr values at given ^{84}Sr , however, these stable isotope variations can only yield a slope that varies following mass dependent fractionation of -0.878, not the slope of -1.26 observed here. Rather, partial melting modelling or fractional crystallisation combined with mixing with an ^{84}Sr depleted reservoir, might explain the observed ureilite ^{88}Sr - ^{84}Sr slope. The ureilites comprise two chemical components each with a distinct ^{84}Sr isotope signature, the first, silicate phases that preserve a typical terrestrial type ^{88}Sr - ^{84}Sr isotope composition, and the second, a refractory component with an ^{84}Sr deficit, such as presolar SiC. In Sr rich samples, minimally affected by partial melting, the terrestrial signature dominates. Partial melting or fractional crystallisation, however, can yield variations in ^{88}Sr and ^{84}Sr that correlate with Sr concentration, where samples with a light ^{88}Sr and ^{84}Sr isotope composition have a lower Sr. At these low Sr concentrations, that in the refractory SiC grains, with a low ^{84}Sr signature dominates.

This model is illustrated in Figure 25 below, which assumes that all refractory SiC grains have a Sr concentration of ~12 ppm (Amari et al., 1995). Each subclass of presolar SiC was modelled using its unique $\delta^{84/86}\text{Sr}$ and $\delta^{88/86}\text{Sr}$ as determined by direct measurements in previous studies (e.g., Stephane et al., 2018; Liu et al., 2015) with M-type $\delta^{84/86}\text{Sr} = -765\%$, $\delta^{88/86}\text{Sr} = -117.5\%$, X1-type $\delta^{84/86}\text{Sr} = -518\%$, $\delta^{88/86}\text{Sr} = +702\%$ and X2-type $\delta^{84/86}\text{Sr} = -485\%$, $\delta^{88/86}\text{Sr} = -457\%$. The model presented here is applicable to both a partial melting and fractional crystallisation scenario as the general observed trend could be produced by either process as partition coefficients will be the same in both scenarios assuming similar conditions across the UPB, only the direction of the Sr transition between liquid and solid may be reversed. In this scenario, it is assumed that the main solid phases present are olivine, pigeonite and minor augite and plagioclase (e.g., Mittlefehldt et al., 1998), with only the pyroxenes and plagioclase able to assert a significant control on Sr partitioning. The model also assumes that SiC does not breakdown during the partial melting of ureilite protolith materials. At the higher degrees of partial melting thought to occur on the UPB (e.g., Collinet and Grove, 2020), as primary Sr is lost to the melt, SiC grains will begin to dominate the isotopic signature of the restite (ureilites as they are observed today). When all major presolar SiC grain types are modelled, M- and X2-type grains provide the best fit to the ureilite data, which is logical considering that both grains possess significant ^{84}Sr and ^{88}Sr deficits compared to X1-type grains which possess relative ^{88}Sr enrichments (e.g., Stephane et al., 2018; Liu et al., 2015). The possible involvement of X2-type grains in ureilite Sr isotopic signatures complicates the interpretation of the data as these grains are also enriched in ^{86}Sr (Stephane et al., 2018), and, as previously stated, isotopic anomalies could lie in ^{86}Sr rather than ^{88}Sr . However, without further ureilite analysis and more extensive modelling it is not possible to distinguish between these possibilities, though based on terrestrial scenarios it is likely that the anomalies do indeed lie in ^{88}Sr (e.g., Amsellem et al., 2018).

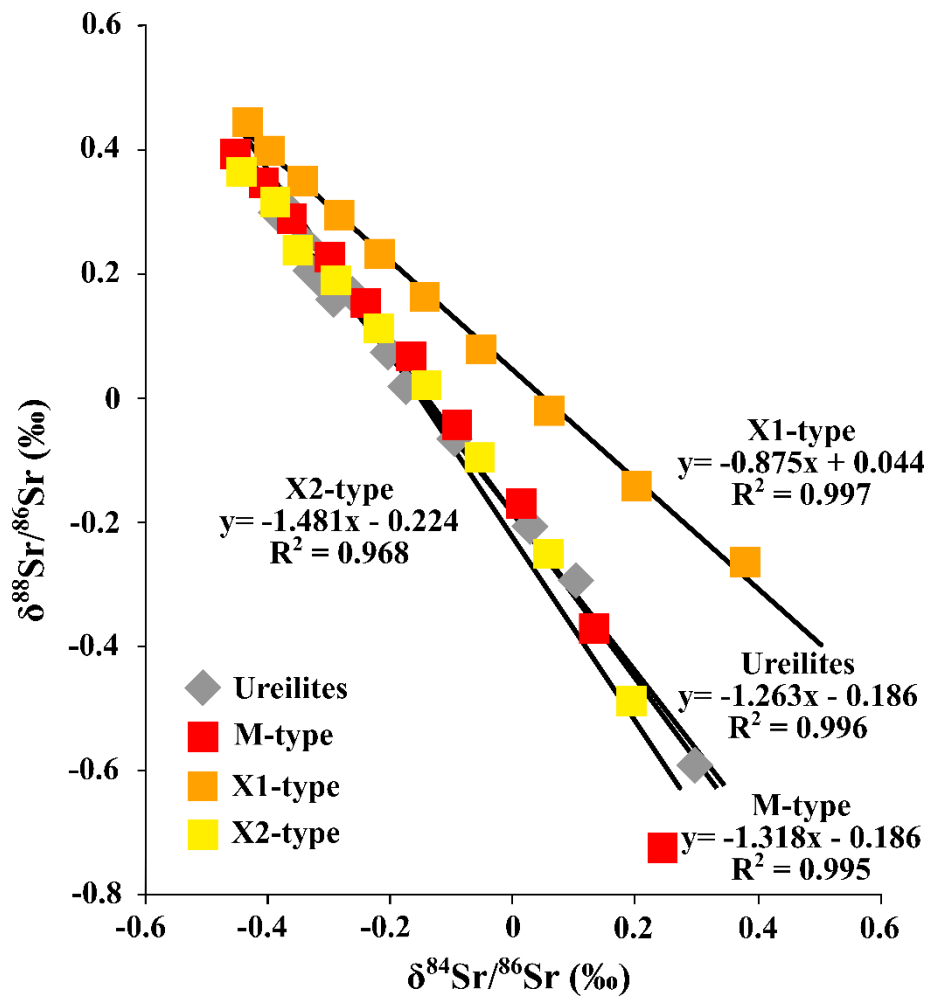


Figure 25- Mixing model for ureilites with the most common presolar SiC grain types. It is assumed that SiC grains are not melted during partial melting of material on the UPB.

5.4.4 Ureilite Rb-Sr isotope systematics

Most samples appear to possess a covariation between $^{87}\text{Rb}/^{86}\text{Sr}$ and $^{87}\text{Sr}/^{86}\text{Sr}$ (Figure 22), consistent with radiogenic ingrowth since the time of crystallisation for these samples and the samples all evolving from material with a similar initial $^{87}\text{Sr}/^{86}\text{Sr}$. Two samples deviate significantly from this correlation, NWA 2624 and EET 96042, possessing more radiogenic $^{87}\text{Sr}/^{86}\text{Sr}$ and higher than expected $^{87}\text{Rb}/^{86}\text{Sr}$ respectively. These outliers are likely caused by one of several Rb-Sr resetting events thought to have occurred on the UPB/UDBs (e.g., Goodrich et al., 1991; 1995), though, especially in the case of NWA 2624, the deviation may also be the product of terrestrial contamination. For the purposes of this discussion the polymict samples are considered separately to the main group ureilites as they are likely not representative of ureilites as a whole because of the possibility that they may sample non-ureilitic materials. The Rb-Sr age given by the main group ureilites analysed in this study, excluding NWA 2624 and EET 96042 as outliers and NWA 2082 and NWA 2703 as materials that are potentially terrestrially contaminated, give an age of approximately 345 Myr (Figure 26). The age derived from these samples is extremely young considering the Mn-Cr ages calculated for the UPB ($\sim 0.6 \pm 1.5$ Myr; Zhu et al., 2020), however is similar to the proposed age of a UDB resetting event based on Sm-Nd dating (~ 340 Myr; Goodrich et al., 1995). The younger age calculated for the UPB could also be the

result of post-crystallisation equilibration of the Rb-Sr system, e.g., elemental lattice diffusion, or by terrestrial contamination as a result of weathering on Earth surface but both of these scenarios are much less likely, especially as terrestrial weathering would be unlikely to give correlation between different samples. In any case, given the Mn-Cr and Hf-W ages of the UPB (Zhu et al., 2020; Budde et al., 2015; Hilton and Walker, 2020), the observed $^{87}\text{Rb}/^{86}\text{Sr}$ - $^{87}\text{Sr}/^{86}\text{Sr}$ covariations are likely indicative of an open system process having affected the $^{87}\text{Rb}/^{86}\text{Sr}$ system such as low temperature metamorphism or hydrothermal alteration.

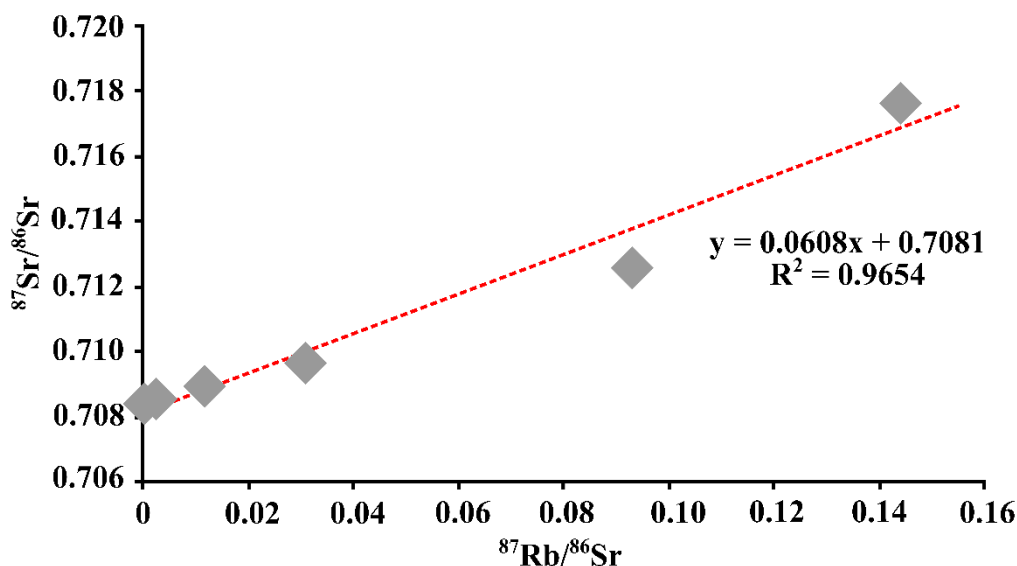


Figure 26- Rb-Sr errorchron for the main group ureilites analysed in this study. Obvious outliers and samples believed to be potentially terrestrially contaminated have been omitted.

As there is clear evidence for open system processes having affected the Rb-Sr systematics of these samples and ureilites in general (e.g., Goodrich et al., 1995), it is prudent to consider the effect that these processes may have had on ^{84}Sr . Comparison of $^{87}\text{Sr}/^{86}\text{Sr}$ with $\mu^{84}\text{Sr}$ suggests that there is no systematic covariation in these samples (Figure 27), unlike the CAIs discussed in chapter 4. The lack of covariation between $^{87}\text{Sr}/^{86}\text{Sr}$ and $\mu^{84}\text{Sr}$ suggests that open-system processes have not systematically affected $\mu^{84}\text{Sr}$ values, although it is not possible to rule out some degree of perturbation of the ^{84}Sr values especially if these processes involved terrestrial Sr; though if perturbed by terrestrial Sr it would be expected that the ureilites might possess smaller ^{84}Sr deficits or excesses and more radiogenic $^{87}\text{Sr}/^{86}\text{Sr}$ (e.g., Charlier et al., 2017; Amsellem et al., 2018). Comparison of $\mu^{84}\text{Sr}$ with Sr and Rb concentrations appears to reinforce this interpretation as many samples with low Sr concentrations, which would be more susceptible to change via contamination/mixing/alteration, appear to possess $\mu^{84}\text{Sr}$ values closer to ~ 0 (relative to NBS 987, taken as representative of the terrestrial $\mu^{84}\text{Sr}$ value). In order to further investigate the possibility of open system behaviour, we consider the variability in the abundance of Rb and Sr relative to an immobile element, in this case Th (Figure 28).

Both main group and polymict ureilites display no significant correlation between Rb/Th and Sr/Th, with Th unlikely to dominate the two ratios as Th concentrations are relatively constant compared to Rb and Sr in the ureilites. Overall, the samples suggest that Rb-Sr distributions are generally decoupled barring a single outlier which appears to have gained unequal amounts of Rb and Sr (NWA 2082) and two outliers which appear to have gained substantial amounts of Sr relative to Rb (Hajmah and Dhofar 979). NWA 2082 appears to covary

with NWA 2624 and NWA 2703 suggesting that they were all affected by the same open system process, likely terrestrial contamination via weathering on impacting Earth based on their stable Sr chemistry (Figure 21). The deviations seen for Hajmah and Dhofar 979 are slightly harder to explain, especially as they possess both lower Rb/Th and high Sr/Th ratios relative to the other main group and polymict ureilites. A similar pattern emerges between the samples when observing Nd/Th data against Sr/Th, indicating that the deviations seen in Hajmah and Dhofar 979 are likely the product of a systematic difference that predates the Rb-Sr resetting event identified by the sample errorchron (Figure 26). Based on the isotopic and trace element evidence already discussed, it is likely this difference is a product of the magmatic processes active on the UPB likely either smelting or variable degrees of partial melting.

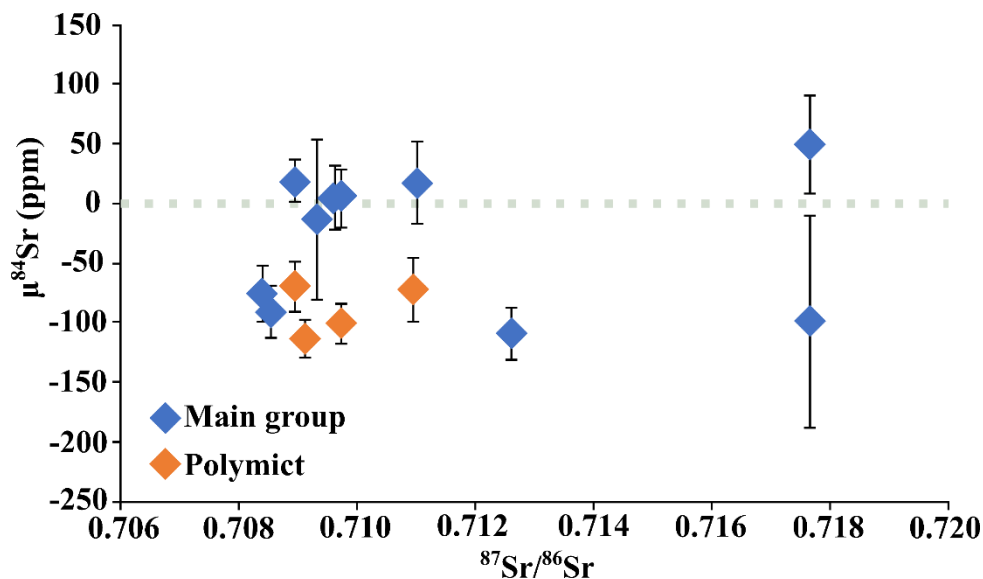


Figure 27- $\mu^{84}\text{Sr}$ vs $^{87}\text{Sr}/^{86}\text{Sr}$ for main group and polymict ureilites analysed in this study. Main group ureilites appear to have a wider range in $^{87}\text{Sr}/^{86}\text{Sr}$ and $\mu^{84}\text{Sr}$ compared to the polymict ureilites.

5.4.5 Mineralogical controls on Sr isotope compositions in ureilites

As discussed in chapter 5.1.1 ureilites consist primarily of olivine and pigeonite, with minor augite, orthopyroxene, C-phases (e.g., diamond and graphite), accessory minerals and sulfides (e.g., Barrat et al., 2015; Goodrich et al., 2004; Warren et al., 2006). Feldspars are typically absent from main group ureilites but are commonly found in polymict ureilites, either in regolith matrix as a single mineral or in feldspathic-plagioclase bearing clasts, which are believed to represent near-surface or deep materials from the UPB not typically sampled by main group ureilites (e.g., Cohen et al., 2004). Clinopyroxene, pigeonite and plagioclase are the major silicate phases present that are likely to act as major Sr hosts. Plagioclase and clinopyroxene were also separated from DaG 319 as part of this study and measured for their $\mu^{84}\text{Sr}$. Both plagioclase and clinopyroxene from DaG 319 appear to possess opposing anomalies compared to the bulk meteorite, with both minerals displaying positive ^{84}Sr excesses within the uncertainty of $\mu^{84}\text{Sr} = 0$. However, as noted previously these excesses are not clearly resolved from terrestrial and typical NC signatures and this should be taken into account when discussing them in conjunction with the ureilite whole rock data. However, despite not being clearly resolved from terrestrial materials and possessing ^{84}Sr excesses, both the plagioclase and clinopyroxene mineral data plots firmly on the ureilite MDFL (Figure 21), indicating that there are no substantial

heterogeneities among these silicate phases. The presence of plagioclase may account for some of the more ^{84}Sr enriched ureilites that appear to be unaffected by terrestrial weathering, however most main group ureilites possess relatively large ^{84}Sr depletions (Figure 20) and almost zero plagioclase (Prinz et al., 1987). Therefore, another phase must be responsible for hosting ^{84}Sr anomalies in bulk ureilites, however any suitable phase would have to possess a large ^{84}Sr deficit in order to exert a strong enough control over bulk ureilite Sr chemistry. There are no clear correlations between $\mu^{84}\text{Sr}$ for bulk ureilites and bulk pigeonite, at least for main group ureilites (Figure 29, however polymict ureilite pigeonites appear to correlate with bulk rock ^{84}Sr).

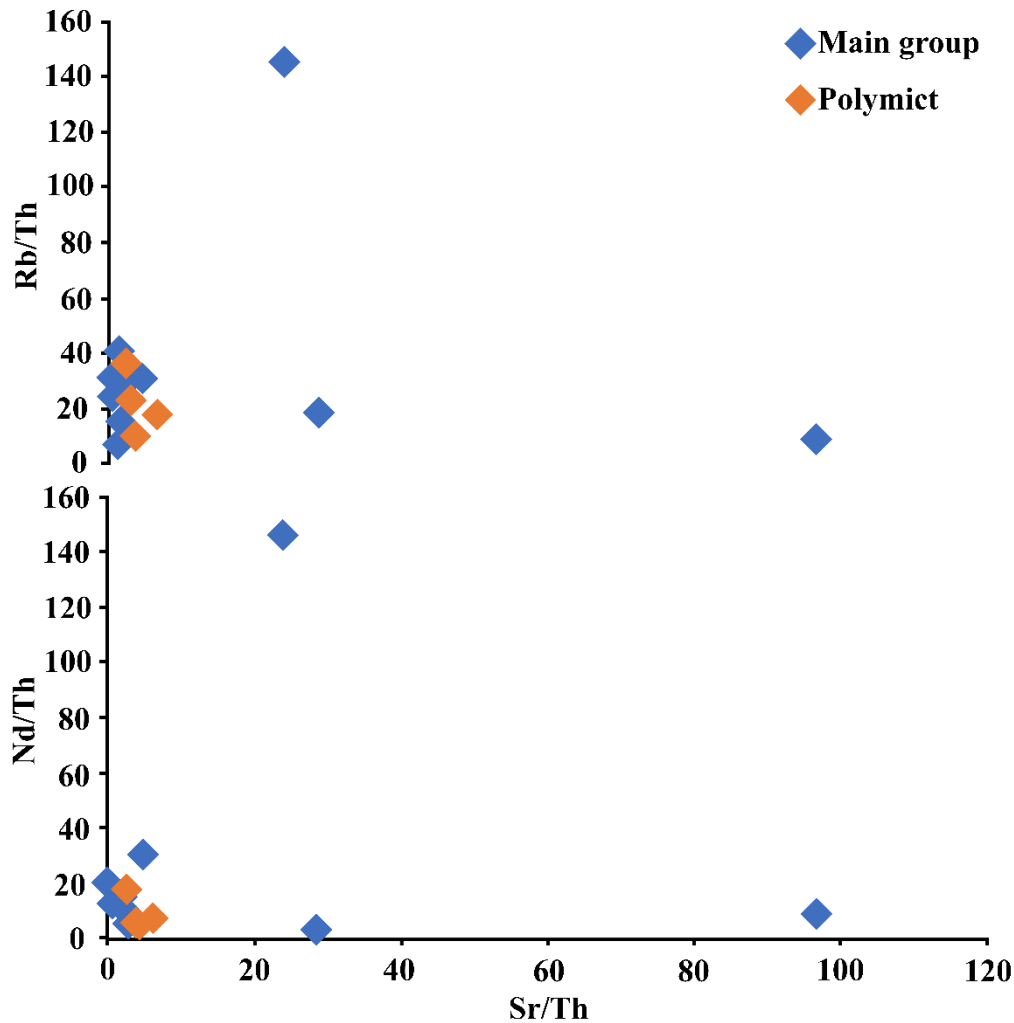


Figure 28- Plots of Nd/Th versus Sr/Th and Rb/Th versus Sr/Th for all the ureilites analysed in this study. Samples that deviate from the ureilite MDFL also possess higher Nd/Th and Rb/Th than their main group counterparts. Data is normalised to CI chondrites (Palme and Beer, 1993). Uncertainties for all data points are smaller than symbol size.

These patterns can be explained by two possibilities (i) the lack of correlation can be explain by pigeonite vs olivine abundances in the main group ureilites, which are likely more heterogenous than polymict ureilites (ii) Sr must be housed in a minor phase that is common to both main group and polymict ureilites that is more likely to be sampled in bulk polymict than main group samples. With the present dataset it is difficult to establish which of these two possibilities is true, however (i) is probably more likely though exact mineral abundances in these ureilites are poorly recorded in the literature. However, the clinopyroxene analysed in this study from DaG 319 show no resolvable ^{84}Sr difference from other NC materials (Figure 29), therefore, clinopyroxene seems unlikely to be the only Sr sink in the ureilites as otherwise many samples would not show

an $\mu^{84}\text{Sr}$ deficit. If (ii) were true then potential phases would include graphite, interstitial silicates, chromite, native metals and metal sulfides; the most likely of these minor phases that could house Sr would likely reside in the interstitial silicates, which comprise up to <10% of ureilite petrography, are less likely to be representatively sampled in a bulk main group measurement and are known to contain a mixture of Sr bearing minerals, e.g., low-Ca pyroxenes, augite and Si-Al-alkali glass (Mittlefehldt et al., 1998). The low-Ca pyroxene assemblage could be of particular interest as these pyroxenes crystallised later than the pigeonite phenocrysts and should be present in both polymict and main group samples but are more likely to be sampled in polymict ureilites. These low-Ca pyroxenes are known to have higher Mg# and lower X/Mg ratios (where X= Mn, Cr, Na, Ti or Al) than the pigeonites that make up the bulk of ureilites (Goodrich et al., 1987b), therefore it is possible that their Sr chemistries may also differ to the major clinopyroxene phases analysed in this study.

5.4.6 s- or p-process origin for $\mu^{84}\text{Sr}$ distributions in ureilites

The $\mu^{84}\text{Sr}$ values obtained for ureilites in this study (Figure 19) can be most simply considered to represent an excess in s-process Sr isotopes (^{86}Sr , ^{87}Sr and ^{88}Sr) leading to a relative deficit in ^{84}Sr for a given $\delta^{86}\text{Sr}$ or $\delta^{88}\text{Sr}$ value in three isotope space. The deviation of $\delta^{84}\text{Sr}$ and $\delta^{88}\text{Sr}$ from the terrestrial MDFL in three isotope space is also consistent with this scenario (Figure 21). The question remains however as to whether the ^{84}Sr distributions in ureilites simply arise from a p-process deficit relative to p-processes excesses as seen in other early solar system materials e.g., CAIs (see chapter 4), or whether there are variations in s-/r-process ^{88}Sr that influence the conventional $^{86}\text{Sr}/^{88}\text{Sr}$ ratio (0.1194; Nier, 1938) used for internal normalisation. The possibility that significant variations in s-/r-process ^{88}Sr cannot be uniquely addressed here as in order to properly discriminate between these alternatives the pre-magmatic process carrier of the nucleosynthetic anomalies in the ureilites must be found, or samples must be measured that possesses extremely low $^{87}\text{Rb}/^{86}\text{Sr}$ ratios that were unaffected by later Rb-Sr resetting events. In the latter case, such samples would record close to the initial $^{87}\text{Sr}/^{86}\text{Sr}$ ratio (requiring minimal age correction) in order to test the conformity of the double spike-derived $^{87}\text{Sr}/^{86}\text{Sr}$ data to a mass-dependent fractionation line in $^{87}\text{Sr}/^{86}\text{Sr}$ - $\delta^{88}\text{Sr}$ space; however, our Rb concentration data is not precise enough for such an approach.

However, the latter two scenarios for the origin of the ^{84}Sr distribution in ureilites seem less likely due to the pre-existing strong evidence for s-process excesses in some NC meteorites. For examples, existing Mo isotope data for NC meteorites has established an s-process mixing line between endmembers with a distinct isotopic compositions- one with an s-process deficit (CAI-like) and the other with s-process excess (NC-like) (e.g., Spitzer et al., 2020). The ureilites are believed to lie on this NC s-process mixing line alongside other NC achondrites (Spitzer et al., 2020). There is also evidence for s-process enrichment in the early inner solar system based on the Nd isotope variations in OC and EC meteorites (Burkhardt et al., 2016; Bouvier and Boyet, 2016; Frossard et al., 2021) suggesting that s-process excesses are common to both NC chondrites and achondrites. For ureilites specifically, there is also evidence for s-process isotope excesses in Os, with ^{186}Os excesses reported in several ureilites (Goedris et al., 2015). One ureilite with a previously reported ^{186}Os excess

(DaG 319, +62.8 ppm; Goedris et al., 2015) was also measured in this study, where it was found to have a $\mu^{84}\text{Sr}$ deficit of -72.2 ± 26.6 ppm, which can also be ascribed to a Sr s-process excess.

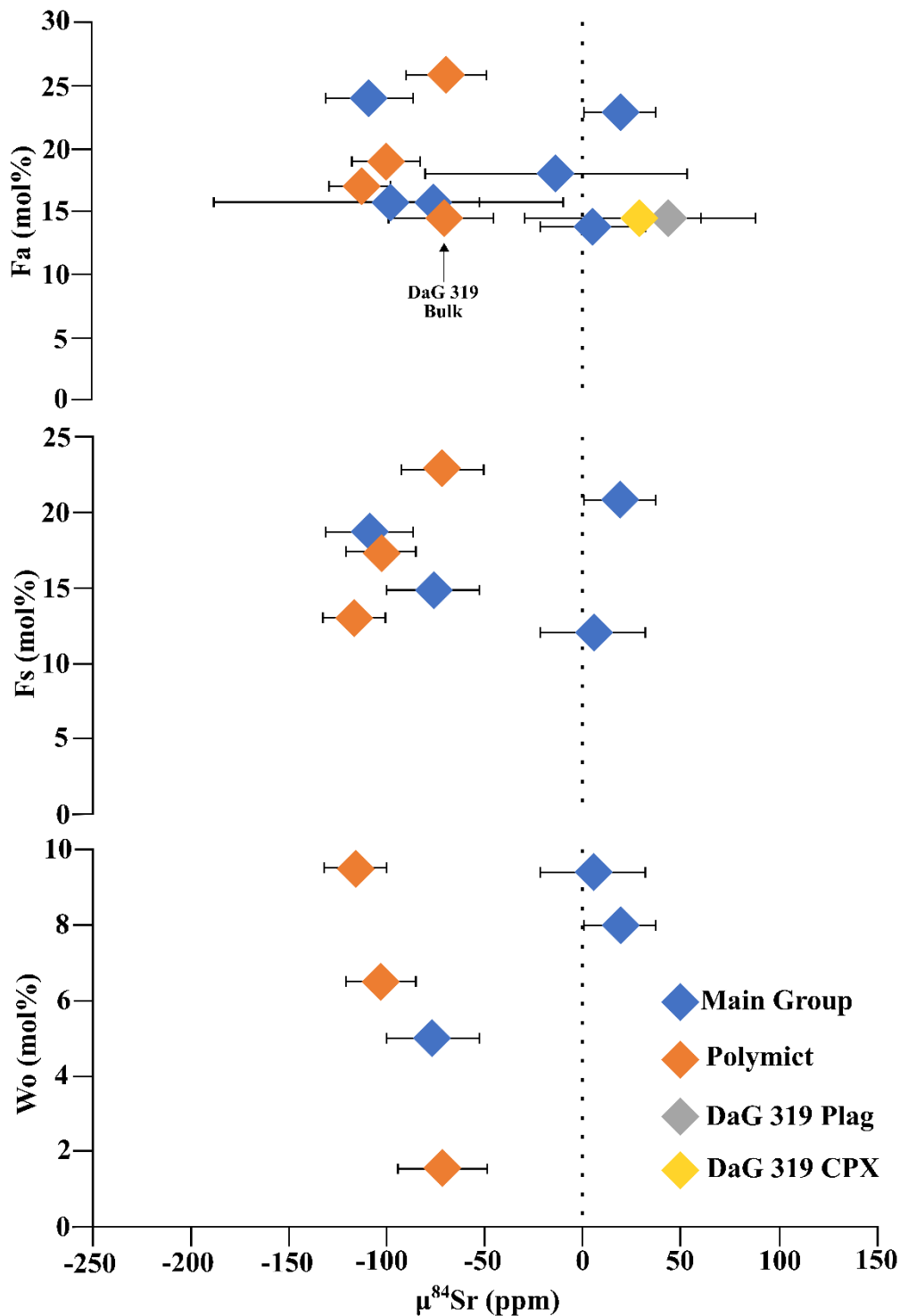


Figure 29- Mineral chemistries plotted against $\mu^{84}\text{Sr}$ for the main minerals present in ureilite mineral assemblages (olivine and clinopyroxene (mostly pigeonite)).

5.4.7 An updated model of the UPB and early protoplanetary disk dynamics

One of the main aims of this study was to update current models for the dynamics of the early protoplanetary disk through improving upon existing models of the lifetime of the UPB. Based on the Sr isotope data obtained for the ureilites analysed here, it is clear that the ureilites are unique, in that, unlike all other NC-meteorites

studied to date (e.g., Charlier et al., 2017), they possess an MDFL in $\delta^{84}\text{Sr}$ - $\delta^{88}\text{Sr}$ space that is distinct from both the terrestrial and CC MDFLs (Figure 21). The unique Sr isotope compositions implied are remarkable, as this can only arise if the UPB accreted pre-solar materials as yet unsampled and/or if the UPB experienced processes thus far unobserved for the rest of the early disk. These unique stable isotope variations are consistent with their $\mu^{84}\text{Sr}$ values, which preserve resolvable ^{84}Sr deficits (Figure 24). Assuming that the cause of these isotope anomalies is the result of ureilite-SiC post-processing mixing, as argued in chapter 5.4.3, then it is interesting to speculate on the cause for the UPB to be enriched in s-process depleted SiC.

One possible explanation is that the extremely s-process depleted presolar SiC proposed here is analogous to the s-process depleted inclusion-like material proposed as one of the three building blocks of the NC-CC isotope dichotomy (Spitzer et al., 2020; Burkhardt et al., 2019; Charlier et al., 2021). Its selective presence in ureilites versus other NC-meteorites may be the result of a preservation bias in the UPB given its position relative to proto-Jupiter and the timing of its accretion as large amounts of material infalling into the disk at this time will have accreted here against the semi-impermeable inner-outer solar system pressure barrier (e.g., Desch et al., 2019a) and may have been accreted into the UPB before mostly being destroyed via thermal processing (Fukai and Yokoyama, 2020). The destruction of the majority of s-processes depleted presolar SiC via thermal processing around the time of UPB accretion would also explain why there is no extensive evidence for these carriers in other NC-meteorite parent bodies, as based on model ages and Mn-Cr dating the UPB is believed to have accreted before the other early formed NC-parent bodies (Mn-Cr: $\sim 0.6 \pm 1.5$ Myr; Zhu et al., 2020; Figure 30), e.g., the HED parent body (Hf-W: ~ 1 Myr; Touboul et al., 2015). If the timing of the destruction of the majority of these s-processes depleted presolar SiC grains is correct, then it can also be speculated that the infall of this material to the disk is restricted to a poorly defined period spanning the onset of CAI condensation to the formation of proto-Jupiter and its associated pressure barrier, i.e., within the first 1 Myr of CAI condensation (e.g., Kruijer et al., 2017; Nanne et al., 2020).

Based on the Sr isotope and trace element systematics observed for the suite of ureilites analysed, it is clear that current models of the UPB should also be updated, in particular to explain the ureilites distinctive Sr isotope composition. The explanation for the ureilites unique Sr isotope chemistry compared to other NC meteorites could possibly result solely from the magmatic processes active on the UPB, however based on the data gathered here and the way in which NWA 2082, NWA 2624 and NWA 2703 lie between the ureilite and terrestrial-NC MDFL it is likely that concentration of SiC grains pre-processing could also exert a significant influence on ureilite Sr chemistry. If the UPB accreted heterogeneously and is considered to have been stratified based on its Mg and Fe chemistry (e.g., Rai et al., 2020) then it is probable that the UPB also accreted SiC grains non-uniformly, resulting in the existence of SiC-rich and SiC-poor domains on the UPB; subsequent magmatic processing of these differently enriched domains could then produce the range of trace element and REE data that currently exists for the ureilites (e.g., this study; Barrat et al., 2016; Bischoff et al., 2014). Alternatively, different magmatic processes operating on the UPB may have interacted variably with SiC resulting in suites of ureilites with both complete and incomplete mixing of the two isotopically distinct

reservoirs. The ureilites analysed here mostly possess REE profiles that are relatively similar to those found in harzburgites and other restite-like terrestrial lithologies, with enrichments in LREE and HREE (e.g., Lesnov, 2010; Tilhac et al., 2021; Figure 18). These harzburgite-like REE profiles have a significant implication for previous studies as ureilites previously analysed that were dismissed as being altered by terrestrial weathering may have in fact been the product of magmatic processes active on the UPB that were similar to some of those that form these ultramafic terrestrial rocks in terrestrial settings. When considering the effect these terrestrial-like magmatic processes may have had on other aspects of ureilite geochemistry, it is possible that alongside ‘smelting’ (Goodrich et al., 2007; Greenwood et al., 2017) they exert a significant control on the O isotope behaviour observed in the ureilites (Figure 17). Assuming this to be the case, then the ureilites O isotope signatures may in fact be the product of variable magmatic processing rather than a primary signature inherited from disk materials as is believed to be the case with most chondrites.

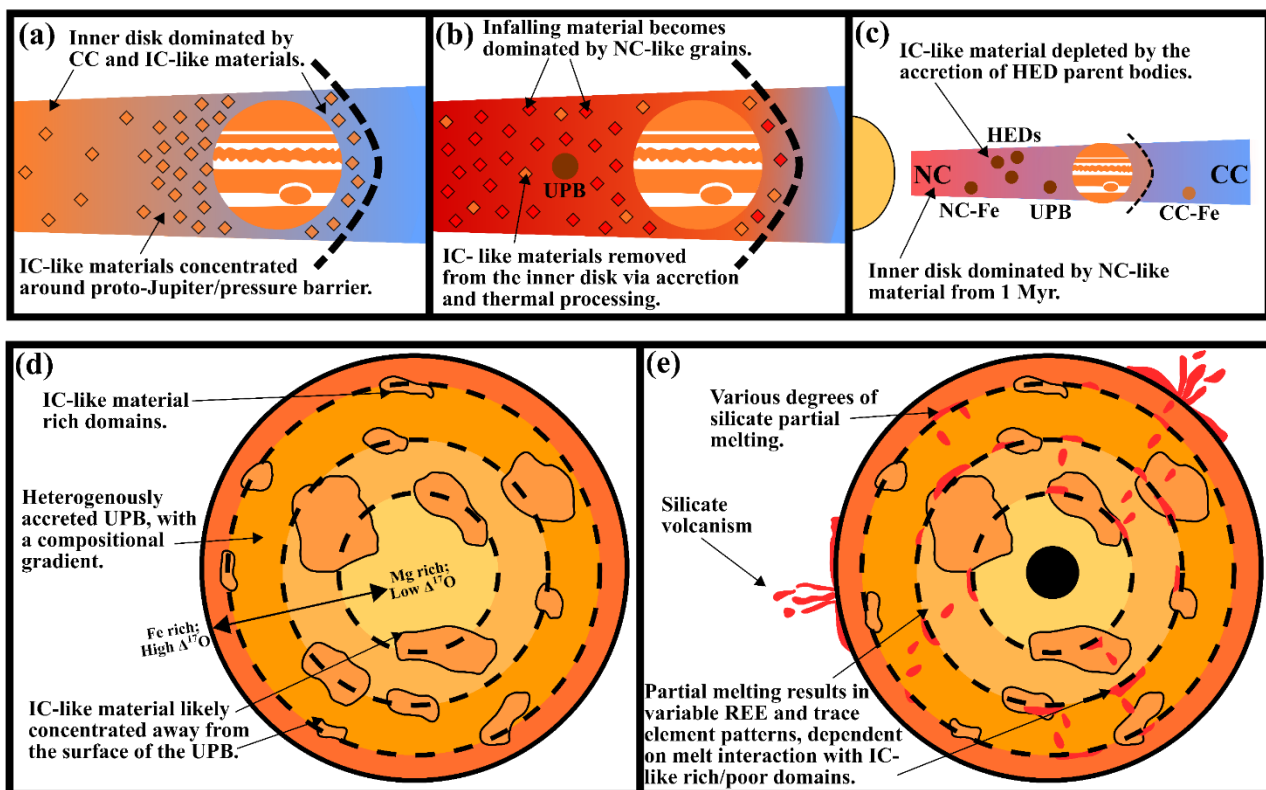


Figure 30- A schematic figure detailing proposed updates to pre-existing models of the early protoplanetary disk and the evolution of the UPB. (a) Some point after CAI condensation the nature of the material infalling into the disk must have changed to reflect IC-like material (Burkhardt et al., 2019), with the inner disk dominated by a mixture of Inclusion-like Chondritic component (IC-like) and CAI-like materials. The formation of proto-Jupiter and its associated pressure barrier concentrates IC-like material on the inner disk side of the barrier, preventing it from completely homogenising in the outer solar system. (b) Infalling material is now dominated by NC-like material and IC-like material is consumed in the disk by a combination of accretion into early formed planetesimals, e.g., the UPB, and thermal processing of the disk (e.g., Fukai and Yokoyama, 2020). (c) NC-like material dominates the inner disk and IC-like materials in the inner disk are fully depleted. All newly formed planetesimals, e.g., HEDs, OCs, ECs, have NC-like compositions and fail to record IC-like signatures for the majority of isotopic systems. (d) The UPB accretes but the planetesimal itself is heterogeneous with a Mg-Fe gradient from the surface to the core and a mixture of IC-like material-rich and -poor domains. The majority of IC-like rich domains would likely be located away from the surface of the planetesimal. (e) Active magmatism begins on the UPB. The interaction of partial melting with chemically heterogeneous zones of the UPB produce a mixture of magmas with variable REE and trace element

5.5 Conclusions

The Sr isotopic data obtained here for main group and polymict ureilites coupled with Rb-Sr, REE and trace element analyses offers new perspectives on the complex history of the early protoplanetary disk and the evolution of the UPB. The ureilites analysed here possess a range of REE and trace element profiles that more closely resemble harzburgites and terrestrial restites (e.g., Lesnov, 2010; Figure 18) than previously analysed ureilites (Barrat et al., 2017; Guan and Crozaz, 2000), with LREE- and HREE-enrichment and mild MREE depletion. Given the Sr isotopic data for ureilites here in conjunction with elemental data, it is argued that these profiles are primary signatures inherited from either the UPB and/or UDBs and do not represent terrestrial contamination of ureilite samples as proposed by previous studies. Previously obtained LREE-depleted ureilite profiles (Barrat et al., 2016) are likely also a primary feature of the UPB and/or UDBs, with the variation in REE systematics being controlled by a combination of heterogeneity in the UPB, active magmatic processes on the UPB and variable metasomatism on the UPB and/or UDBs.

This study presents the first comprehensive Sr isotope data for ureilites S. These results demonstrate that Sr behaviour in ureilites is unique compared to almost all other meteorites analysed to date. The total range in $\delta^{88}\text{Sr}$ is $\sim 1.0\%$ (-0.59% to $+0.38\%$); over this range, many of the analysed ureilites show a substantial and resolvable deficit in $\mu^{84}\text{Sr}$, regardless of any mass-dependent fractionation they have experienced. The majority of the ureilite data obtained here clearly falls in the depleted $\mu^{84}\text{Sr}$ region, with a large number of samples plotting well outside of the mean NC field (Figure 24). Across both main group and polymict ureilites heavier $\delta^{88}\text{Sr}$ signatures are generally accompanied by $\mu^{84}\text{Sr}$ excess, though there is no significant correlation between the two (Figure 23). Both polymict and main group ureilites appear to be the product of isotopic reservoir mixing, made evident by magmatic processes occurring on the UPB (e.g., fractional crystallisation and partial melting), however polymict ureilites are also likely to be the product of multiple reservoirs owing to the fact the clasts and regolith materials related to much later formed meteorites often make up a significant proportion of finds. It is likely that the main mixing reservoirs for the ureilites is NC-like material and as yet unidentified material depleted in ^{84}Sr and s-process isotopes. Based on the Sr systematics of individual mineral separates analysed in one ureilite, the two most major silicates that concentrate Sr, plagioclase and clinopyroxene, can be dismissed as carriers of low ^{84}Sr as they possess $\mu^{84}\text{Sr}$ values that are indistinguishable from those of NC and terrestrial materials (Figure 29). One potential candidate for this missing endmember is presolar SiC, specifically mainstream- (m)-type and X1-type grains based on simple reservoir modelling (Figure 25).

The case for the presence of presolar SiC in ureilites is strengthened when considering the variations in $\delta^{84/86}\text{Sr}$ versus $\delta^{88/86}\text{Sr}$ isotope space that ureilites appear to possess (Figure 21). The ureilites and their constituent minerals span a greater $\delta^{88}\text{Sr}$ range (-0.59% to $+0.38\%$; Table 5) than that observed, thus far, for differentiated meteorites (-0.09% to $+0.44\%$; Charlier et al., 2017), bulk undifferentiated meteorites ($+0.24$ to $+0.43\%$; Charlier et al., 2017), and terrestrial materials ($+0.134\%$ to $+0.446\%$; Charlier et al., 2017). Average ureilite $\delta^{88}\text{Sr}$ compositions also tend to be much lighter ($+0.011 \pm 0.023\%$) than terrestrial materials ($+0.29 \pm 0.07\%$;

Moynier et al., 2012; Charlier et al., 2012) and bulk differentiated meteorites ($+0.30 \pm 0.011\%$; Charlier et al., 2017). The ureilite MDFL lies on a much steeper slope than both the NC/terrestrial MDFL and the MDFLs defined by the CAIs and CC meteorites, which is consistent with mixing in ureilites between NC like material and presolar SiC as a result of partial melting and/or fractional crystallisation on the UPB. The three samples that do not fall on the ureilite MDFL (NWA 2624, NWA 2082 and NWA 2703) either represent contamination (either by chondritic or terrestrial materials) or, more likely, indicate that ureilite-SiC reservoir mixing was not uniform across the UPB. However, further ureilite analysis and more extensive modelling is needed in order to determine the exact process(es) responsible for the deviation of the ureilite MDFL from the NC-terrestrial MDFL, especially as the Rb-Sr systematics of the ureilites are indicative of open system processes having affected most specimens on either the UPB or UBDs (Figure 26 ; Goodrich et al., 1991; 1995). However, while this behaviour may have affected trace elements it is fairly clear that isotopic and REE profiles of the ureilites remain primary features of the UPB/UBDs (Figures 27 and 28).

In summary, the $\mu^{84}\text{Sr}$ deficits observed for many ureilites in this study (Figure 19) can be most simply considered to reflect an excess in s-process Sr isotopes (^{86}Sr , ^{87}Sr and ^{88}Sr) leading to a consequent shift in $\delta^{84}\text{Sr}$ for a given $\delta^{88}\text{Sr}$ value in three isotope space. The question remains however as to whether the ^{84}Sr distributions in ureilites simply arise from a p-process deficit relative to p-processes excesses as seen in other early solar system materials e.g., CAIs (see chapter 4), or whether there are variations in s-/r-process ^{88}Sr that influence the conventional $^{86}\text{Sr}/^{88}\text{Sr}$ ratio (0.1194; Nier, 1938) used for internal normalisation. The possibility that significant variations in s-/r-process ^{88}Sr cannot be uniquely addressed here as in order to properly discriminate between these alternatives as our Rb concentration data is not precise enough. However, due to strong, pre-existing evidence for s-process excesses in other elements, e.g., Mo and Os, in NC meteorites (Spitzer et al., 2020; Burkhardt et al., 2016; Bouvier and Boyet, 2016; Goedris et al., 2015) it seems likely that the ureilites ^{84}Sr deficits are the product of s-process isotope excesses. Given the findings of this study pre-existing models for the early proto-planetary disk should be updated. Specifically, infall models for the disk need to reflect the addition and elimination of inclusion-like materials (Burkhardt et al., 2019; Fukai and Yokoyama, 2020) between CAI condensation and the accretion of early formed planetesimals after the accretion of the UPB. Models detailing the evolution of the UPB should also be updated to reflect the accretionary, magmatic and geochemical processes required in order to establish the ureilites unique MDFL in $\delta^{84/86}\text{Sr}$ versus $\delta^{88/86}\text{Sr}$ isotope space.

6. Summary

This study aimed to resolve one or two of the gaps in our current understanding regarding the evolution of the inner (NC) and outer (CC) solar system reservoirs and the evolution of early formed planetesimals in the inner disk. This was achieved through the analysis of differently textured CAIs and other materials from the chondritic (CV) meteorite Allende and the analysis of the ureilites (for which there were no Sr measurements prior to this work) using the Sr double-spike method. This study reports high precision double-spike ^{84}Sr and ^{88}Sr data alongside REE and trace element data for a suite of CAIs, ureilites and other materials. A multi-isotope approach was used to improve on pre-existing models for the development of the early protoplanetary disk (<1 Myr post-CAI condensation), the separation of the NC and CC reservoirs and the geochemical evolution of the UPB.

Our high precision isotopic Sr data for fine- and coarse-grained Allende CAIs coupled with Rb-Sr and trace element analyses offers a new perspective on the complex history of Allende CAIs. All fine-grained CAIs analysed here (excluding CAI30) possess group II REE patterns while coarse-grained CAIs possess group I, V, or III REE patterns (Figure 6). Across both textural types, all CAIs analysed possess elevated nucleosynthetic $\mu^{84}\text{Sr}$ values with an average of $+141 \pm 375\text{ppm}$ (2 s.d., $n = 12$), though coarse- and fine-grained CAIs have slightly different $\mu^{84}\text{Sr}$ anomalies, defining average values of $+192 \pm 236\text{ppm}$ (2 s.d., $n = 7$), and $+68 \pm 43\text{ppm}$ (2 s.d., $n = 5$), respectively. The $\mu^{84}\text{Sr}$ values obtained here correlate within error to those previously obtained for carbonaceous chondrites (e.g., Charlier et al., 2017), however the CAIs of this study possess slightly higher textural averages than previously recorded in Allende CAIs. Complementary Rb-Sr data for the CAIs analysed (Figure 9), suggests that the fine-grained CAIs analysed here have been affected by open-system alteration post-condensation. The post-condensation open-system alteration observed in the analysed CAIs is likely represents either mixing between the fine-grained CAIs and another early solar system material that possess lower $\mu^{84}\text{Sr}$ excesses or deficits i.e., chondrules (Paton et al., 2013), or open-system aqueous alteration as indicated by their Rb-Sr chemistry and the absence of a strong correlation between Sr and Nd.

The double-spike stable Sr CAI data yields an MDFL that is offset with respect to the NC-terrestrial equilibrium MDFL in three-isotope space ($\delta^{88/86}\text{Sr}$ versus $\delta^{84/86}\text{Sr}$) but is not concordant with the previously obtained CAI MDFL (Charlier et al., 2019), showing a significant degree of scatter, likely a product of the presumed aqueous alteration of most of the fine-grained CAIs analysed here. Fine-grained CAIs are asymmetrically distributed towards light $\delta^{88}\text{Sr}$ values, it is therefore concluded that the stable Sr isotopic compositions in the fine-grained CAIs analysed here primarily reflect kinetic isotope effects that occurred during condensation, with minimal influence from partial evaporation and/or recondensation post initial formation. Our coarse-grained inclusions do not show the general clustering of $\delta^{88}\text{Sr}$ values reported by previous studies (Charlier et al., 2019), instead displaying a trend towards lighter $\delta^{88}\text{Sr}$ at high Sr concentrations, reflecting either a condensation path from a less supersaturated parent gas than the for fine-

grained CAIs or possibly the result of post-condensation processes that also possess kinetic controls, such as remelting or susceptibility to aqueous alteration for CAIs with low Sr concentrations. As in previous studies, our data alone is unable to categorically distinguish between p-process anomalies in ^{84}Sr versus r-, and weak and main s-process variability in ^{88}Sr , however previous studies suggest that anomalies likely reside in ^{84}Sr and we support this hypothesis.

The new isotopic Sr data obtained by this study for ureilites coupled with Rb-Sr, REE and trace element analyses offers an additional perspective on both the development of the early protoplanetary disk and the evolution of the UPB. Unlike most previous studies (Barrat et al., 2017; Guan and Crozaz, 2000), the ureilites analysed here possess a range of REE and trace element profiles that more closely resemble harzburgites and terrestrial restites (e.g., Lesnov, 2010; Figure 18). Coupled with the Sr isotopic data also obtained, it is argued that these elemental profiles are primary signatures inherited from either the UPB and/or UDBs and do not represent terrestrial contamination of ureilite samples as proposed by previous studies (Barrat et al., 2016). It is proposed that the UPB likely was able to produce materials with a variety of REE profiles via active magmatic processes, e.g., partial melting and fractional crystallisation, and variable metasomatism on the UPB and/or UDBs.

The Sr chemistry of the ureilites is unique compared to almost all other meteorites analysed to date. The total range in $\delta^{88}\text{Sr}$ is $\sim 1.0\%$ (-0.59% to $+0.38\%$) and over this range, many of the ureilites are resolvably offset from $\mu^{84}\text{Sr} = 0$, regardless of any mass-dependent fractionation they have experienced. These ureilite data fall in the depleted $\mu^{84}\text{Sr}$ region, well outside of the mean NC field (Figure 24). To date no other analysed meteorite group has been found to possess ^{84}Sr deficits as large as those recorded for the majority of ureilites (e.g., Charlier et al., 2017). Both polymict and main group ureilites appear to be the product of isotopic reservoir mixing, likely resulting from magmatic processes occurring on the UPB (e.g., fractional crystallisation and partial melting). Polymict ureilites should be considered more carefully, as their chemistry is potentially representative of multiple reservoirs, owing to the fact that xenoliths of much later formed meteorites often make up a significant proportion of finds. However, the polymict ureilites analysed here are dominated by s-process Sr deficits suggesting that these later formed xenoliths do not exert a significant control on overall Sr chemistry. The main mixing reservoirs for the ureilites is likely NC-like material and an as yet unidentified material enriched in s-process Sr isotopes, probably IC-like material (e.g., Burkhardt et al., 2019). Based on the Sr systematics of individual mineral separates analysed in ureilites, plagioclase and clinopyroxene, can be dismissed as the main carriers of the $\mu^{84}\text{Sr}$ as they possess either ^{84}Sr excesses or are unresolvable from NC and terrestrial ^{84}Sr signatures (Figure 29).

The $\mu^{84}\text{Sr}$ values obtained for ureilites in this study (Figure 19) can be most simply considered to represent an excess in s-process Sr isotopes (^{86}Sr , ^{87}Sr and ^{88}Sr) leading to a relative offset in $\delta^{84}\text{Sr}$ for a given $\delta^{88}\text{Sr}$ value in three isotope space. The question remains however as to whether the ^{84}Sr distributions in ureilites simply arise from a p-process deficit relative to p-processes excesses as seen in other early solar system materials e.g.,

CAIs (Chapter 4; Figure 31), or whether there are variations in s-/r-process ^{88}Sr that influence the conventional $^{86}\text{Sr}/^{88}\text{Sr}$ ratio (0.1194; Nier, 1938) used for internal normalisation. As for the CAIs analysed here, the possibility that significant variations in s-/r-process ^{88}Sr cannot be uniquely addressed by this study as our Rb concentration data is not precise enough to properly discriminate between these alternatives. However, strong evidence in the ureilites and other NC meteorites exists for s-process excesses in other elements, e.g., Mo and Os, (Spitzer et al., 2020; Burkhardt et al., 2016; Bouvier and Boyet, 2016; Goedris et al., 2015), and therefore it seems likely that the ^{84}Sr deficits observed here are the product of s-process isotope excesses.

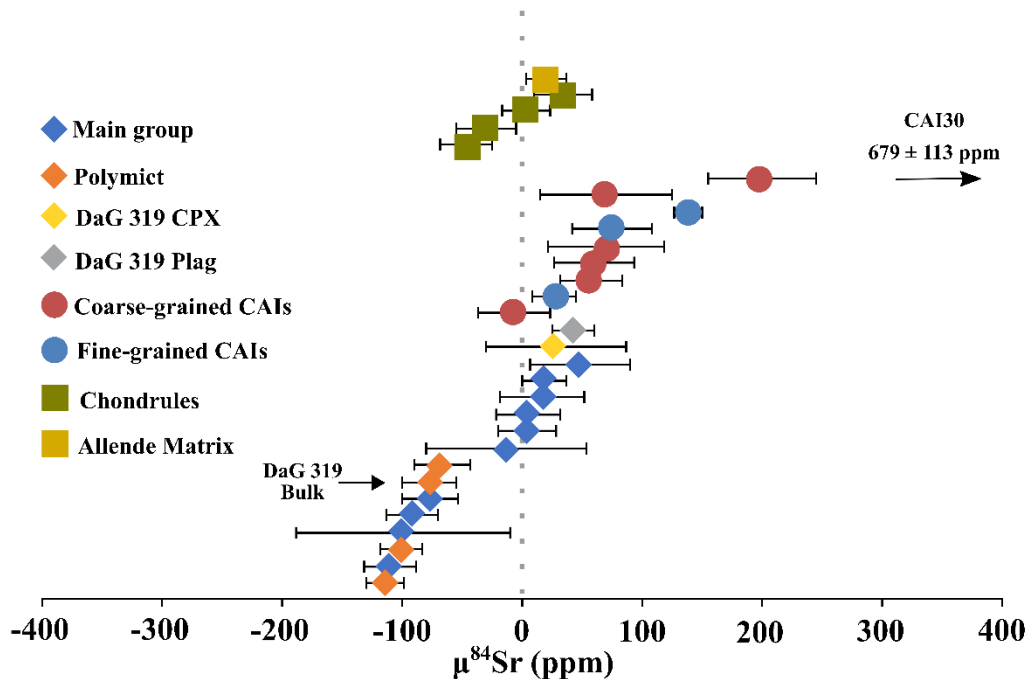


Figure 31- All ureilite, CAI and meteorite component data measured in this study. A majority of Ureilites analysed possess $\mu^{84}\text{Sr}$ deficits while almost all CAIs possess $\mu^{84}\text{Sr}$ excesses.

The ureilites and their plagioclase and clinopyroxene mineral separates span a greater $\delta^{88}\text{Sr}$ range (-0.59‰ to +0.38‰; Table 5) than that observed, thus far, for differentiated meteorites (-0.09‰ to +0.44‰; Charlier et al., 2017), bulk undifferentiated meteorites (+0.24 to +0.43‰; Charlier et al., 2017), and terrestrial materials (+0.134‰ to +0.446‰; Charlier et al., 2017). Average ureilite $\delta^{88}\text{Sr}$ compositions also tend to be much lighter (+0.011 ± 0.24‰) than terrestrial materials (+0.29 ± 0.07‰; Moynier et al., 2012; Charlier et al., 2012) and bulk differentiated meteorites (+0.30 ± 0.011‰; Charlier et al., 2017). The ureilite MDFL lies on a much steeper slope than both the NC/terrestrial MDFL and the MDFLs defined by the CAIs and CC meteorites, which is indicative of the reservoir mixing between ureilites and an unknown reservoir, likely IC-like material (e.g., Burkhardt et al., 2019). Based on simple reservoir modelling in $\delta^{84/86}\text{Sr}$ versus $\delta^{88/86}\text{Sr}$ isotope space (Figure 25) and their presumed abundance in the inner protoplanetary disk around the time of UPB accretion (e.g., Stephane et al., 2018; Desch et al., 2018) presolar SiC, specifically mainstream- (m)-type and X1-type grains, are invoked as a potentially suitable reservoir material for the IC-like component observed in the ureilites analysed. The three samples that do not fall on the ureilite MDFL (NWA 2624, NWA 2082 and NWA 2703) either represent contamination (either by chondritic or terrestrial materials) or, more likely, indicate that ureilite-SiC reservoir mixing was non-uniform/incomplete across the UPB. Further analysis and more

extensive modelling is needed in order to determine the exact process(es) responsible for the unique ureilite MDFL and the Rb-Sr systematics of the ureilites, which are indicative of open system processes being active on the UPB and/or UBDs (Figure 26 ; Goodrich et al., 1991; 1995). However, while this behaviour may have affected trace elements it is fairly clear that isotopic and REE profiles of the ureilites remain primary features of the UPB/UBDs (Figures 27 and 28).

The Sr isotope and elemental data presented here for the CAIs and ureilites significantly affects pre-existing models of the early proto-planetary disk. Modelling of the infall of material into the protoplanetary disk especially needs to be re-examined to account for the affects and timing of the addition and elimination of IC-like materials (Burkhardt et al., 2019; Fukai and Yokoyama, 2020) between the onset of CAI condensation and the accretion of early formed planetesimals after the accretion of the UPB. As in all early disk models, it is evident that proto-Jupiter and its associated pressure barrier between the inner and outer disk exert a significant influence on the development of the NC and CC reservoirs (e.g., Nanne et al., 2020) and, based on this study, further extensive Sr isotope analysis of NC-meteorite groups (e.g., ECs, OCs and NC-Fe meteorites) may be able to reveal the exact nature of this influence. This study also reinforces the hypothesis that the UPB accreted heterogeneously and possessed distinctive isotopic reservoirs (Rai et al., 2020). The ureilites unique MDFL in in $\delta^{84/86}\text{Sr}$ versus $\delta^{88/86}\text{Sr}$ isotope (Figure 32) space coupled with Rb-Sr and REE data indicate that complex open system and magmatic processes were active on the UPB that must be comparable to those currently active on Earth.

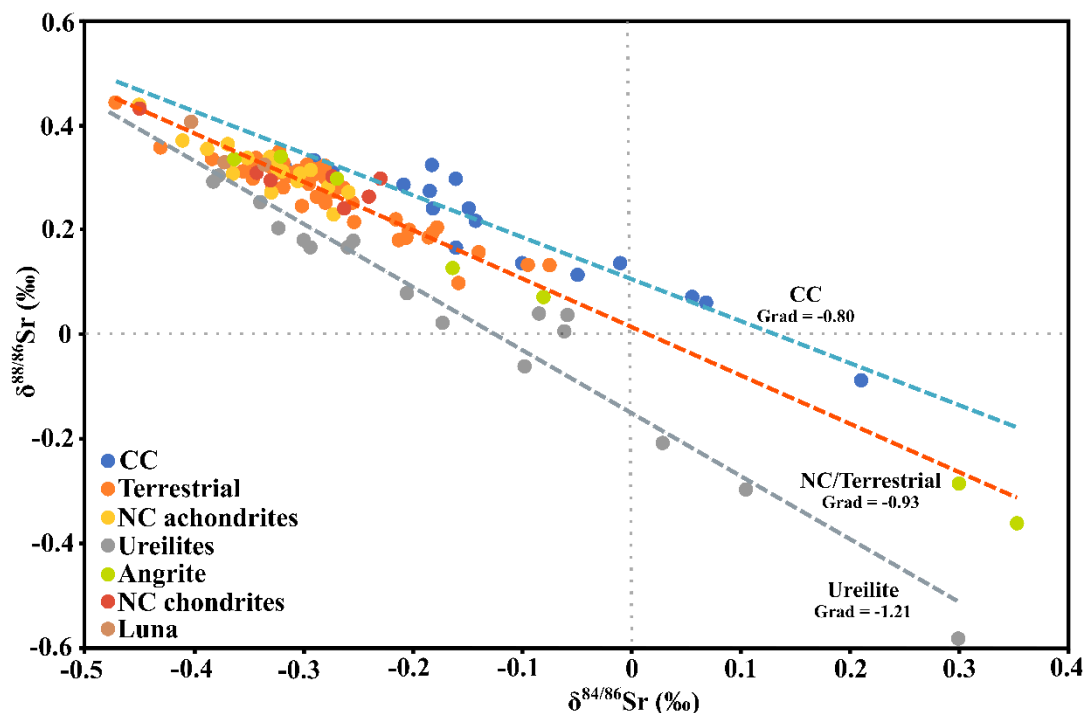


Figure 32- $\delta^{88/86}\text{Sr}$ vs $\delta^{84/86}\text{Sr}$ plot for ureilites, NC and CC materials (Charlier et al., 2017). Ureilites lie on a significantly distinct correlation line from other inner solar system and terrestrial materials. Three ureilites (NWA 2082, NWA 2624 and NWA 2703) deviate significantly from this line and are positioned between the NC/terrestrial line and the ureilite line suggesting the possibility of mixing between the two trends.

7. References

- Alexander, C.M.D., Howard, K.T., Bowden, R. and Fogel, M.L., 2013. The classification of CM and CR chondrites using bulk H, C and N abundances and isotopic compositions. *Geochimica et Cosmochimica Acta*, 123, pp.244-260.
- Amari, S., Hoppe, P., Zinner, E. and Lewis, R.S., 1995. Trace-element concentrations in single circumstellar silicon carbide grains from the Murchison meteorite. *Meteoritics*, 30(6), pp.679-693.
- Amari, S., 2020, March. The Origin of Ureilites: A Noble-Gas Perspective. In 51st Annual Lunar and Planetary Science Conference (No. 2326, p. 1716).
- Amsellem, E., Moynier, F., Day, J.M., Moreira, M., Puchtel, I.S. and Teng, F.Z., 2018. The stable strontium isotopic composition of ocean island basalts, mid-ocean ridge basalts, and komatiites. *Chemical Geology*, 483, pp.595-602.
- Asplund, M., Lambert, D.L., Kipper, T., Pollacco, D. and Shetrone, M.D., 1998. The rapid evolution of the born-again giant Sakurai's object. arXiv preprint astro-ph/9811208.
- Barrat, J.A., Rouxel, O., Wang, K., Moynier, F., Yamaguchi, A., Bischoff, A. and Langlade, J., 2015. Early stages of core segregation recorded by Fe isotopes in an asteroidal mantle. *Earth and Planetary Science Letters*, 419, pp.93-100.
- Barrat, J.A., Sansjofre, P., Yamaguchi, A., Greenwood, R.C. and Gillet, P., 2017. Carbon isotopic variation in ureilites: Evidence for an early, volatile-rich Inner Solar System. *Earth and Planetary Science Letters*, 478, pp.143-149.
- Bekaert, D.V., Auro, M., Shollenberger, Q.R., Liu, M.C., Marschall, H., Burton, K.W., Jacobsen, B., Brennecka, G.A., MacPherson, G.J., von Mutius, R. and Sarafian, A., 2021. Fossil records of early solar irradiation and cosmolocalization of the CAI factory: A reappraisal. *Science advances*, 7(40), p.eabg8329.
- Berkley, J.L. and Jones, J.H., 1982. Primary igneous carbon in ureilites: Petrological implications. *Journal of Geophysical Research: Solid Earth*, 87(S01), pp.A353-A364.
- Berkley, J.L., Taylor, G.J., Keil, K., Harlow, G.E. and Prinz, M., 1980. The nature and origin of ureilites. *Geochimica et Cosmochimica Acta*, 44(10), pp.1579-1597.

- Bermingham, K.R., Gussone, N., Mezger, K. and Krause, J., 2018. Origins of mass-dependent and mass-independent Ca isotope variations in meteoritic components and meteorites. *Geochimica et cosmochimica acta*, 226, pp.206-223.
- Bischoff, A., Horstmann, M., Barrat, J.A., Chaussidon, M., Pack, A., Herwartz, D., Ward, D., Vollmer, C. and Decker, S., 2014. Trachyandesitic volcanism in the early Solar System. *Proceedings of the National Academy of Sciences*, 111(35), pp.12689-12692.
- Bisterzo, S., Travaglio, C., Gallino, R., Wiescher, M. and Käppeler, F., 2014. Galactic chemical evolution and solar s-process abundances: Dependence on the ^{13}C -pocket structure. *The Astrophysical Journal*, 787(1), p.10.
- Blackburn, T., Alexander, C.M.D., Carlson, R. and Elkins-Tanton, L.T., 2017. The accretion and impact history of the ordinary chondrite parent bodies. *Geochimica et Cosmochimica Acta*, 200, pp.201-217.
- Boley, A.C., Morris, M.A. and Desch, S.J., 2013. High-temperature processing of solids through solar nebular bow shocks: 3D radiation hydrodynamics simulations with particles. *The Astrophysical Journal*, 776(2), p.101.
- Böhm, F., Eisenhauer, A., Tang, J., Dietzel, M., Krabbenhöft, A., Kiskakürek, B. and Horn, C., 2012. Strontium isotope fractionation of planktic foraminifera and inorganic calcite. *Geochimica et Cosmochimica Acta*, 93, pp.300-314.
- Brasser, R. and Mojzsis, S.J., 2020. The partitioning of the inner and outer Solar System by a structured protoplanetary disk. *Nature Astronomy*, 4(5), pp.492-499.
- Braukmüller, N., Wombacher, F., Hezel, D.C., Escoube, R. and Münker, C., 2018. The chemical composition of carbonaceous chondrites: Implications for volatile element depletion, complementarity and alteration. *Geochimica et Cosmochimica Acta*, 239, pp.17-48.
- Brennecka, G.A., Burkhardt, C., Budde, G., Kruijjer, T.S., Nimmo, F. and Kleine, T., 2020. Astronomical context of Solar System formation from molybdenum isotopes in meteorite inclusions. *Science*, 370(6518), pp.837-840.
- Bridgestock, L.J., Williams, H., Rehkämper, M., Larner, F., Giscard, M.D., Hammond, S., Coles, B., Andreasen, R., Wood, B.J., Theis, K.J. and Smith, C.L., 2014. Unlocking the zinc isotope systematics of iron meteorites. *Earth and Planetary Science Letters*, 400, pp.153-164.
- Budde, G., Burkhardt, C., Brennecka, G.A., Fischer-Gödde, M., Kruijjer, T.S. and Kleine, T., 2016. Molybdenum isotopic evidence for the origin of chondrules and a distinct genetic heritage of carbonaceous and non-carbonaceous meteorites. *Earth and Planetary Science Letters*, 454, pp.293-303.

Burkhardt, C., Dauphas, N., Hans, U., Bourdon, B. and Kleine, T., 2019. Elemental and isotopic variability in solar system materials by mixing and processing of primordial disk reservoirs. *Geochimica et Cosmochimica Acta*, 261, pp.145-170.

Charlier, B.L., Ginibre, C., Morgan, D., Nowell, G.M., Pearson, D.G., Davidson, J.P. and Ottley, C.J., 2006. Methods for the microsampling and high-precision analysis of strontium and rubidium isotopes at single crystal scale for petrological and geochronological applications. *Chemical Geology*, 232(3-4), pp.114-133.

Charlier, B.L.A., Nowell, G.M., Parkinson, I.J., Kelley, S.P., Pearson, D.G. and Burton, K.W., 2012. High temperature strontium stable isotope behaviour in the early solar system and planetary bodies. *Earth and Planetary Science Letters*, 329, pp.31-40.

Charlier, B.L.A., Parkinson, I.J., Burton, K.W., Grady, M.M., Wilson, C.J.N. and Smith, E.G.C., 2017. Stable strontium isotopic heterogeneity in the solar system from double-spike data. *Geochemical perspectives letters.*, 4, pp.35-40.

Charlier, B.L.A., Tissot, F.L.H., Dauphas, N. and Wilson, C.J.N., 2019. Nucleosynthetic, radiogenic and stable strontium isotopic variations in fine- and coarse-grained refractory inclusions from Allende. *Geochimica et Cosmochimica Acta*, 265, pp.413-430.

Clayton, D.D. and Nittler, L.R., 2004. Astrophysics with presolar stardust. *Annu. Rev. Astron. Astrophys.*, 42, pp.39-78.

Clayton, R.N. and Mayeda, T.K., 1996. Oxygen isotope studies of achondrites. *Geochimica et Cosmochimica Acta*, 60(11), pp.1999-2017.

Clayton, R.N., Onuma, N., Grossman, L. and Mayeda, T.K., 1977. Distribution of the pre-solar component in Allende and other carbonaceous chondrites. *Earth and Planetary Science Letters*, 34(2), pp.209-224.

Cohen, B.A., Goodrich, C.A. and Keil, K., 2004. Feldspathic clast populations in polymict ureilites: Stalking the missing basalts from the ureilite parent body. *Geochimica et Cosmochimica Acta*, 68(20), pp.4249-4266.

Collinet, M. and Grove, T.L., 2020. Incremental melting in the ureilite parent body: Initial composition, melting temperatures, and melt compositions. *Meteoritics & Planetary Science*, 55(4), pp.832-856.

Connelly, J.N., Bizzarro, M., Krot, A.N., Nordlund, Å., Wielandt, D. and Ivanova, M.A., 2012. The absolute chronology and thermal processing of solids in the solar protoplanetary disk. *Science*, 338(6107), pp.651-655.

- Dauphas, N. and Schauble, E.A., 2016. Mass fractionation laws, mass-independent effects, and isotopic anomalies. *Annual Review of Earth and Planetary Sciences*, 44, pp.709-783.
- Davis, A.M., Zhang, J., Greber, N.D., Hu, J., Tissot, F.L. and Dauphas, N., 2018. Titanium isotopes and rare earth patterns in CAIs: Evidence for thermal processing and gas-dust decoupling in the protoplanetary disk. *Geochimica et cosmochimica acta*, 221, pp.275-295.
- Debret, B., Reekie, C.D.J., Mattioli, N., Savov, I., Beunon, H., Ménez, B. and Williams, H.M., 2020. Redox transfer at subduction zones: insights from Fe isotopes in the Mariana forearc. *Geochemical Perspectives Letters*, 12, pp.46-51.
- Defouilloy, C., Cartigny, P., Assayag, N., Moynier, F. and Barrat, J.A., 2016. High-precision sulfur isotope composition of enstatite meteorites and implications of the formation and evolution of their parent bodies. *Geochimica et Cosmochimica Acta*, 172, pp.393-409.
- Desch, S., O'Rourke, J., Schaefer, L., Schrader, D. and Sharp, T., 2019, September. 15 Eunomia and collisional family as the source of ureilites. In *EPSC-DPS Joint Meeting 2019 (Vol. 2019, pp. EPSC-DPS2019)*.
- Desch, S.J., Kalyaan, A. and Alexander, C.M.D., 2018. The effect of Jupiter's formation on the distribution of refractory elements and inclusions in meteorites. *The Astrophysical Journal Supplement Series*, 238(1), p.11.
- Drake, M.J., 2001. Presidential address: presented 2000 August 28, Chicago, Illinois, USA the eucrite/Vesta story. *Meteoritics & Planetary Science*, 36(4), pp.501-513.
- Dunn, T.L., Gross, J., Ivanova, M.A., Runyon, S.E. and Bruck, A.M., 2016. Magnetite in the unequilibrated CK chondrites: Implications for metamorphism and new insights into the relationship between the CV and CK chondrites. *Meteoritics & Planetary Science*, 51(9), pp.1701-1720.
- Ebel, D.S. and Grossman, L., 2000. Condensation in dust-enriched systems. *Geochimica et Cosmochimica Acta*, 64(2), pp.339-366.
- Farquhar, J., Jackson, T.L. and Thiemens, M.H., 2000. A ^{33}S enrichment in ureilite meteorites: evidence for a nebular sulfur component. *Geochimica et Cosmochimica Acta*, 64(10), pp.1819-1825.
- Frank, D.R., Zolensky, M.E. and Le, L., 2014. Olivine in terminal particles of Stardust aerogel tracks and analogous grains in chondrite matrix. *Geochimica et Cosmochimica Acta*, 142, pp.240-259.

Frossard, P., Guo, Z., Spencer, M., Boyet, M. and Bouvier, A., 2021. Evidence from achondrites for a temporal change in Nd nucleosynthetic anomalies within the first 1.5 million years of the inner solar system formation. *Earth and Planetary Science Letters*, 566, p.116968.

Fukai, R. and Yokoyama, T., 2019. Nucleosynthetic Sr–Nd isotope correlations in chondrites: Evidence for nebular thermal processing and dust transportation in the early Solar System. *The Astrophysical Journal*, 879(2), p.79.

Gerber, S., Burkhardt, C., Budde, G., Metzler, K. and Kleine, T., 2017. Mixing and transport of dust in the early solar nebula as inferred from titanium isotope variations among chondrules. *The Astrophysical Journal Letters*, 841(1), p.L17.

Goderis, S., Brandon, A.D., Mayer, B. and Humayun, M., 2015. s-Process Os isotope enrichment in ureilites by planetary processing. *Earth and Planetary Science Letters*, 431, pp.110-118.

Goodrich, C.A. and Desch, S.J., 2019, July. Exogenous Metal in Ureilites. In 82nd Annual Meeting of The Meteoritical Society (Vol. 82, No. 2157, p. 6094).

Goodrich, C.A., 1992. Ureilites: A critical review. *Meteoritics*, 27(4), pp.327-352.

Goodrich, C.A., Hartmann, W.K., O'Brien, D.P., Weidenschilling, S.J., Wilson, L., Michel, P. and Jutzi, M., 2015. Origin and history of ureilitic material in the solar system: The view from asteroid 2008 TC 3 and the Almahata Sitta meteorite. *Meteoritics & planetary science*, 50(4), pp.782-809.

Goodrich, C.A., Scott, E.R. and Fioretti, A.M., 2004. Ureilitic breccias: clues to the petrologic structure and impact disruption of the ureilite parent asteroid. *Geochemistry*, 64(4), pp.283-327.

Gray, C., Papanastassiou, D. and Wasserburg, G.J., 1973. The identification of early condensates from the solar nebula. *Icarus*, 20(2), pp.213-239.

Greenwood, R.C., Barrat, J.A., Scott, E.R., Haack, H., Buchanan, P.C., Franchi, I.A., Yamaguchi, A., Johnson, D., Bevan, A.W. and Burbine, T.H., 2015. Geochemistry and oxygen isotope composition of main-group pallasites and olivine-rich clasts in mesosiderites: Implications for the “Great Dunite Shortage” and HED-mesosiderite connection. *Geochimica et Cosmochimica Acta*, 169, pp.115-136.

Greenwood, R.C., Burbine, T.H., Miller, M.F. and Franchi, I.A., 2017. Melting and differentiation of early-formed asteroids: The perspective from high precision oxygen isotope studies. *Geochemistry*, 77(1), pp.1-43.

Guan, Y. and Crozaz, G., 2000. Light rare earth element enrichments in ureilites: a detailed ion microprobe study. *Meteoritics & Planetary Science*, 35(1), pp.131-144.

Hans, U., 2013. High-precision strontium isotope measurements on meteorites: implications for the origin and timing of volatile depletion in the inner solar system (Doctoral dissertation, ETH Zurich).

Haugbølle, T., Weber, P., Wielandt, D.P., Benítez-Llambay, P., Bizzarro, M., Gressel, O. and Pessah, M.E., 2019. Probing the protosolar disk using dust filtering at gaps in the early solar system. *The Astronomical Journal*, 158(2), p.55.

Henshall, T., Cook, D.L., Garçon, M. and Schönbächler, M., 2018. High-precision strontium isotope analysis of geological samples by thermal ionisation mass spectrometry. *Chemical Geology*, 482, pp.113-120.

Hilton, C.D. and Walker, R.J., 2020. New implications for the origin of the IAB main group iron meteorites and the isotopic evolution of the noncarbonaceous (NC) reservoir. *Earth and planetary science letters*, 540, p.116248.

Hilton, C.D., Bermingham, K.R., Walker, R.J. and McCoy, T.J., 2019. Genetics, crystallization sequence, and age of the South Byron Trio iron meteorites: New insights to carbonaceous chondrite (CC) type parent bodies. *Geochimica et cosmochimica acta*, 251, pp.217-228.

Hu, J.Y., Dauphas, N., Tissot, F.L.H., Yokochi, R., Ireland, T.J., Zhang, Z., Davis, A.M., Ciesla, F.J., Grossman, L., Charlier, B.L.A. and Roskosz, M., 2021. Heating events in the nascent solar system recorded by rare earth element isotopic fractionation in refractory inclusions. *Science advances*, 7(2), p.eabc2962.

Huang, S., Farkaš, J., Yu, G., Petaev, M.I. and Jacobsen, S.B., 2012. Calcium isotopic ratios and rare earth element abundances in refractory inclusions from the Allende CV3 chondrite. *Geochimica et Cosmochimica Acta*, 77, pp.252-265.

Humayun, M. and Weiss, B.P., 2011, March. A common parent body for Eagle Station pallasites and CV chondrites. In 42nd Annual Lunar and Planetary Science Conference (No. 1608, p. 1507).

Huyskens, M.H., Sanborn, M.E., Yin, Q.Z., Amelin, Y. and Koefoed, P., 2019, March. Chronology of carbonaceous achondrites from the outer solar system. In 50th Annual Lunar and Planetary Science Conference (No. 2132, p. 2736).

Ireland, T.R. and Fegley Jr, B., 2000. The solar system's earliest chemistry: Systematics of refractory inclusions. *International Geology Review*, 42(10), pp.865-894.

- Jambon, A., Boudouma, O., Fonteilles, M., Guillou, C.L., Badia, D. and Barrat, J.A., 2008. Petrology and mineralogy of the angrite Northwest Africa 1670. *Meteoritics & Planetary Science*, 43(11), pp.1783-1795.
- Kaminski, E., Limare, A., Kenda, B. and Chaussidon, M., 2020. Early accretion of planetesimals unraveled by the thermal evolution of the parent bodies of magmatic iron meteorites. *Earth and Planetary Science Letters*, 548, p.116469.
- Keil, K. and McCoy, T.J., 2018. Acapulcoite-lodranite meteorites: Ultramafic asteroidal partial melt residues. *Geochemistry*, 78(2), pp.153-203.
- Keil, K., 2010. Enstatite achondrite meteorites (aubrites) and the histories of their asteroidal parent bodies. *Geochemistry*, 70(4), pp.295-317.
- King, A.J., Phillips, K.J.H., Strekopytov, S., Vita-Finzi, C. and Russell, S.S., 2020. Terrestrial modification of the Ivuna meteorite and a reassessment of the chemical composition of the CI type specimen. *Geochimica et Cosmochimica Acta*, 268, pp.73-89.
- Kita, N.T., Nagahara, H., Togashi, S. and Morishita, Y., 2000. A short duration of chondrule formation in the solar nebula: Evidence from ^{26}Al in Semarkona ferromagnesian chondrules. *Geochimica et Cosmochimica Acta*, 64(22), pp.3913-3922.
- Kita, N.T., Yin, Q.Z., MacPherson, G.J., Ushikubo, T., Jacobsen, B., Nagashima, K., Kurahashi, E., Krot, A.N. and Jacobsen, S.B., 2013. ^{26}Al - ^{26}Mg isotope systematics of the first solids in the early solar system. *Meteoritics & Planetary Science*, 48(8), pp.1383-1400.
- Klaver, M., Lewis, J., Parkinson, I.J., Elburg, M.A., Vroon, P.Z., Kelley, K.A. and Elliott, T., 2020. Sr isotopes in arcs revisited: tracking slab dehydration using $\delta^{88}\text{Sr}/^{86}\text{Sr}$ and $^{87}\text{Sr}/^{86}\text{Sr}$ systematics of arc lavas. *Geochimica et Cosmochimica Acta*, 288, pp.101-119.
- Kleine, T., Budde, G., Burkhardt, C., Kruijjer, T.S., Worsham, E.A., Morbidelli, A. and Nimmo, F., 2020. The non-carbonaceous–carbonaceous meteorite dichotomy. *Space Science Reviews*, 216(4), pp.1-27.
- Klessen, R.S., Glover, S.C.O., Clark, P.C., Greif, T.H. and Bromm, V., 2011, October. Modeling the Effects of Turbulence in Zero-and Low-metallicity Star Formation. In 5th International Conference of Numerical Modeling of Space Plasma Flows (ASTRONUM 2010) (Vol. 444, p. 42).

Kööp, L., Nakashima, D., Heck, P.R., Kita, N.T., Tenner, T.J., Krot, A.N., Nagashima, K., Park, C. and Davis, A.M., 2016. New constraints on the relationship between ^{26}Al and oxygen, calcium, and titanium isotopic variation in the early Solar System from a multielement isotopic study of spinel-hibonite inclusions. *Geochimica et Cosmochimica Acta*, 184, pp.151-172.

Krot, A.N., Amelin, Y., Cassen, P. and Meibom, A., 2005. Young chondrules in CB chondrites from a giant impact in the early Solar System. *Nature*, 436(7053), pp.989-992.

Krot, A.N., Petaev, M.I., Russell, S.S., Itoh, S., Fagan, T.J., Yurimoto, H., Chizmadia, L., Weisberg, M.K., Komatsu, M., Ulyanov, A.A. and Keil, K., 2004. Amoeboid olivine aggregates and related objects in carbonaceous chondrites: records of nebular and asteroid processes. *Geochemistry*, 64(3), pp.185-239.

Krot, A.N., Scott, E.R. and Zolensky, M.E., 1995. Mineralogical and chemical modification of components in CV3 chondrites: Nebular or asteroidal processing?. *Meteoritics*, 30(6), pp.748-775.

Kruijer, T.S., Burkhardt, C., Budde, G. and Kleine, T., 2017. Age of Jupiter inferred from the distinct genetics and formation times of meteorites. *Proceedings of the National Academy of Sciences*, 114(26), pp.6712-6716.

Kruijer, T.S., Touboul, M., Fischer-Gödde, M., Bermingham, K.R., Walker, R.J. and Kleine, T., 2014. Protracted core formation and rapid accretion of protoplanets. *Science*, 344(6188), pp.1150-1154.

Langendam, A.D., Tomkins, A.G., Evans, K.A., Wilson, N.C., MacRae, C.M., Stephen, N.R. and Torpy, A., 2021. CHOS gas/fluid-induced reduction in ureilites. *Meteoritics & Planetary Science*, 56(11), pp.2062-2082.

Leshin, L.A., Rubin, A.E. and McKeegan, K.D., 1997. The oxygen isotopic composition of olivine and pyroxene from CI chondrites. *Geochimica et Cosmochimica Acta*, 61(4), pp.835-845.

Lesnov, F.P., 2010. Rare earth elements in ultramafic and mafic rocks and their minerals. CRC.

Lichtenberg, T., Golabek, G.J., Dullemond, C.P., Schönbächler, M., Gerya, T.V. and Meyer, M.R., 2018. Impact splash chondrule formation during planetesimal recycling. *Icarus*, 302, pp.27-43.

Lin, Y., Gyngard, F. and Zinner, E., 2010. Isotopic analysis of supernova SiC and Si₃N₄ grains from the Qingzhen (EH3) chondrite. *The Astrophysical Journal*, 709(2), p.1157.

Liu, N., Savina, M.R., Gallino, R., Davis, A.M., Bisterzo, S., Gyngard, F., Käppeler, F., Cristallo, S., Dauphas, N., Pellin, M.J. and Dillmann, I., 2015. Correlated strontium and barium isotopic compositions of acid-cleaned single mainstream silicon carbides from Murchison. *The Astrophysical Journal*, 803(1), p.12.

Liu, N., Stephan, T., Cristallo, S., Gallino, R., Boehnke, P., Nittler, L.R., Alexander, C.M.D., Davis, A.M., Trappitsch, R., Pellin, M.J. and Dillmann, I., 2019. Presolar silicon carbide grains of types Y and Z: Their molybdenum isotopic compositions and stellar origins. *The Astrophysical Journal*, 881(1), p.28.

Lodders, K. and Palme, H., 2009. Solar system elemental abundances in 2009. *Meteoritics and Planetary Science Supplement*, 72, p.5154.

Lodders, K., 2003. Solar system abundances and condensation temperatures of the elements. *The Astrophysical Journal*, 591(2), p.1220.

Lucas, M.P., Dygert, N., Ren, J., Hesse, M.A., Miller, N.R. and McSween, H.Y., 2020. Evidence for early fragmentation-reassembly of ordinary chondrite (H, L, and LL) parent bodies from REE-in-two-pyroxene thermometry. *Geochimica et Cosmochimica Acta*, 290, pp.366-390.

Lugaro, M., Herwig, F., Lattanzio, J.C., Gallino, R. and Straniero, O., 2003. s-process nucleosynthesis in asymptotic giant branch stars: A test for stellar evolution. *The astrophysical journal*, 586(2), p.1305.

Lugaro, M., Karakas, A.I., Petó, M. and Plachy, E., 2018. Do meteoritic silicon carbide grains originate from asymptotic giant branch stars of super-solar metallicity?. *Geochimica et Cosmochimica Acta*, 221, pp.6-20.

Ma, C., Beckett, J.R. and Rossman, G.R., 2014. Allendeite (Sc₄Zr₃O₁₂) and hexamolybdenum (Mo, Ru, Fe), two new minerals from an ultrarefractory inclusion from the Allende meteorite. *American Mineralogist*, 99(4), pp.654-666.

MacPherson, G.J., Bullock, E.S., Tenner, T.J., Nakashima, D., Kita, N.T., Ivanova, M.A., Krot, A.N., Petaev, M.I. and Jacobsen, S.B., 2017. High precision Al–Mg systematics of forsterite-bearing Type B CAIs from CV3 chondrites. *Geochimica et Cosmochimica Acta*, 201, pp.65-82.

MacPherson, G.J., Kita, N.T., Ushikubo, T., Bullock, E.S. and Davis, A.M., 2012. Well-resolved variations in the formation ages for Ca–Al-rich inclusions in the early Solar System. *Earth and Planetary Science Letters*, 331, pp.43-54.

MacPherson, G.J., Simon, S.B., Davis, A.M., Grossman, L. and Krot, A.N., 2005, December. Calcium-aluminum-rich inclusions: Major unanswered questions. In *Chondrites and the protoplanetary disk* (Vol. 341, p. 225).

- Mann, C.R., Boley, A.C. and Morris, M.A., 2016. Planetary embryo bow shocks as a mechanism for chondrule formation. *The Astrophysical Journal*, 818(2), p.103.
- McSween Jr, H.Y., 1977. On the nature and origin of isolated olivine grains in carbonaceous chondrites. *Geochimica et Cosmochimica Acta*, 41(3), pp.411-418.
- Mendybaev, R.A., Kamibayashi, M., Teng, F.Z., Savage, P.S., Georg, R.B., Richter, F.M. and Tachibana, S., 2021. Experiments quantifying elemental and isotopic fractionations during evaporation of CAI-like melts in low-pressure hydrogen and in vacuum: Constraints on thermal processing of CAIs in the protoplanetary disk. *Geochimica et Cosmochimica Acta*, 292, pp.557-576.
- Mittlefehldt, D.W. and McCoy, T.J., 2014. Achondrites and irons: Products of magmatism on strongly heated asteroids. *35 Seasons of US Antarctic Meteorites (1976-2010): A Pictorial Guide To The Collection*, 68, p.79.
- Mittlefehldt, D.W., Killgore, M. and Lee, M.T., 2002. Petrology and geochemistry of D'Orbigny, geochemistry of Sahara 99555, and the origin of angrites. *Meteoritics & Planetary Science*, 37(3), pp.345-369.
- Mittlefehldt, D.W., McCoy, T.J., Goodrich, C.A. and Kracher, A., 1998. Non-chondritic meteorites from asteroidal bodies. *Reviews in Mineralogy and Geochemistry*.
- Morbidelli, A., Bitsch, B., Crida, A., Gounelle, M., Guillot, T., Jacobson, S., Johansen, A., Lambrechts, M. and Lega, E., 2016. Fossilized condensation lines in the Solar System protoplanetary disk. *Icarus*, 267, pp.368-376.
- Morlok, A., Bischoff, A., Stephan, T., Floss, C., Zinner, E. and Jessberger, E.K., 2006. Brecciation and chemical heterogeneities of CI chondrites. *Geochimica et Cosmochimica Acta*, 70(21), pp.5371-5394.
- Morris, M.A. and Desch, S.J., 2010. Thermal histories of chondrules in solar nebula shocks. *The Astrophysical Journal*, 722(2), p.1474.
- Moynier, F., Day, J.M., Okui, W., Yokoyama, T., Bouvier, A., Walker, R.J. and Podosek, F.A., 2012. Planetary-scale strontium isotopic heterogeneity and the age of volatile depletion of early Solar System materials. *The Astrophysical Journal*, 758(1), p.45.
- Myojo, K., Yokoyama, T., Okabayashi, S., Wakaki, S., Sugiura, N. and Iwamori, H., 2018. The origin and evolution of nucleosynthetic Sr isotope variability in calcium and aluminum-rich refractory inclusions. *The Astrophysical Journal*, 853(1), p.48.

- Nanne, J.A., Nimmo, F., Cuzzi, J.N. and Kleine, T., 2019. Origin of the non-carbonaceous–carbonaceous meteorite dichotomy. *Earth and Planetary Science Letters*, 511, pp.44-54.
- Nestola, F., Goodrich, C.A., Morana, M., Barbaro, A., Jakubek, R.S., Christ, O., Brenker, F.E., Domeneghetti, M.C., Dalconi, M.C., Alvaro, M. and Fioretti, A.M., 2020. Impact shock origin of diamonds in ureilite meteorites. *Proceedings of the National Academy of Sciences*, 117(41), pp.25310-25318.
- Neuland, M.B., Mezger, K., Riedo, A., Tulej, M. and Wurz, P., 2021. The chemical composition and homogeneity of the Allende matrix. *Planetary and space science*, 204, p.105251.
- Neuvonen, K.J., Ohlson, B., Papunen, H., Häkli, T.A. and Ramdohr, P., 1972. The Haverö ureilite. *Meteoritics*, 7(4), pp.514-531.
- Nier, A.O., 1938. The isotopic constitution of strontium, barium, bismuth, thallium and mercury. *Physical Review*, 54(4), p.275.
- Nittler, L.R., Alexander, C.M.O.D., Patzer, A. and Verrier-Paoletti, M.J., 2021. Presolar stardust in highly pristine CM chondrites Asuka 12169 and Asuka 12236. *Meteoritics & Planetary Science*, 56(2), pp.260-276.
- Niu, Y., 2004. Bulk-rock major and trace element compositions of abyssal peridotites: implications for mantle melting, melt extraction and post-melting processes beneath mid-ocean ridges. *Journal of Petrology*, 45(12), pp.2423-2458.
- O'Brien, D.P., Izidoro, A., Jacobson, S.A., Raymond, S.N. and Rubie, D.C., 2018. The delivery of water during terrestrial planet formation. *Space Science Reviews*, 214(1), pp.1-24.
- Olsen, M.B., Wielandt, D., Schiller, M., Van Kooten, E.M. and Bizzarro, M., 2016. Magnesium and ⁵⁴Cr isotope compositions of carbonaceous chondrite chondrules—Insights into early disk processes. *Geochimica et cosmochimica acta*, 191, pp.118-138.
- Palme H., and Beer H., 1993. Abundances of the elements in the solar system. In *Landolt-Boörnstein, Group VI: Astronomy and Astrophysics: Instruments; Methods; Solar System* (ed. H. H. Voigt). Springer, Berlin, vol. 3(a), pp. 196–221.
- Palme, H., Lodders, K. and Jones, A., 2014. Solar system abundances of the elements. *Planets, Asteroids, Comets and The Solar System, Volume 2 of Treatise on Geochemistry (Second Edition)*. Edited by Andrew M. Davis. Elsevier, 2014., p. 15-36, 2.

- Papanastassiou, D.A. and Wasserburg, G.J., 1968. Initial strontium isotopic abundances and the resolution of small time differences in the formation of planetary objects. *Earth and Planetary Science Letters*, 5, pp.361-376.
- Park, C., Nagashima, K., Krot, A.N., Huss, G.R., Davis, A.M. and Bizzarro, M., 2017. Calcium-aluminum-rich inclusions with fractionation and unidentified nuclear effects (FUN CAIs): II. Heterogeneities of magnesium isotopes and ^{26}Al in the early Solar System inferred from in situ high-precision magnesium-isotope measurements. *Geochimica et Cosmochimica Acta*, 201, pp.6-24.
- Patchett, P.J., 1980. Sr isotopic fractionation in Allende chondrules: a reflection of solar nebular processes. *Earth and Planetary Science Letters*, 50(1), pp.181-188.
- Patchett, P.J., 1980. Sr isotopic fractionation in Ca–Al inclusions from the Allende meteorite. *Nature*, 283(5746), pp.438-441.
- Paton, C., Schiller, M. and Bizzarro, M., 2013. Identification of an ^{84}Sr -depleted carrier in primitive meteorites and implications for thermal processing in the solar protoplanetary disk. *The Astrophysical Journal Letters*, 763(2), p.L40.
- Piccoli, F., Hermann, J., Pettke, T., Connolly, J.A.D., Kempf, E.D. and Vieira Duarte, J.F., 2019. Subducting serpentinites release reduced, not oxidized, aqueous fluids. *Scientific Reports*, 9(1), pp.1-7.
- Pignatale, F.C., Gonzalez, J.F., Bourdon, B. and Fitoussi, C., 2019. Size and density sorting of dust grains in SPH simulations of protoplanetary discs–II. Fragmentation. *Monthly Notices of the Royal Astronomical Society*, 490(3), pp.4428-4446.
- Pignatari, M., Gallino, R., Heil, M., Wiescher, M., Käppeler, F., Herwig, F. and Bisterzo, S., 2010. The weak s-process in massive stars and its dependence on the neutron capture cross sections. *The Astrophysical Journal*, 710(2), p.1557.
- Poole, G.M., Rehkämper, M., Coles, B.J., Goldberg, T. and Smith, C.L., 2017. Nucleosynthetic molybdenum isotope anomalies in iron meteorites–new evidence for thermal processing of solar nebula material. *Earth and Planetary Science Letters*, 473, pp.215-226.
- Pravdivtseva, O.V., Krot, A.N., Hohenberg, C.M., Meshik, A.P., Weisberg, M.K. and Keil, K., 2003. The I-Xe record of alteration in the Allende CV chondrite. *Geochimica et Cosmochimica Acta*, 67(24), pp.5011-5026.

Prinz, M., Weisberg, M.K. and Nehru, C.E., 1988. Gunlock, a new type 3 ordinary chondrite with a golfball-sized chondrule. *Meteoritics*, 23, p.297.

Prinz, M., Weisberg, M.K., Nehru, C.E. and Delaney, J.S., 1987, March. EET 83309, a polymict ureilite: Recognition of a new group. In *Lunar and Planetary Science Conference (Vol. 18)*.

Rai, N., Downes, H. and Smith, C., 2020. Ureilite meteorites provide a new model of early planetesimal formation and destruction. *Geochemical Perspectives Letters*, 14, pp.20-25.

Rankenburg, K., Brandon, A.D. and Humayun, M., 2007. Osmium isotope systematics of ureilites. *Geochimica et Cosmochimica Acta*, 71(9), pp.2402-2413.

Rauscher, T., Heger, A., Hoffman, R.D. and Woosley, S.E., 2002. Nucleosynthesis in massive stars with improved nuclear and stellar physics. *The Astrophysical Journal*, 576(1), p.323.

Rotenberg, E., Davis, D.W., Amelin, Y., Ghosh, S. and Bergquist, B.A., 2012. Determination of the decay-constant of ^{87}Rb by laboratory accumulation of ^{87}Sr . *Geochimica et Cosmochimica Acta*, 85, pp.41-57.

Ruzicka, A., 2014. Silicate-bearing iron meteorites and their implications for the evolution of asteroidal parent bodies. *Geochemistry*, 74(1), pp.3-48.

Sahijpal, S., Goswami, J.N. and Davis, A.M., 2000. K, Mg, Ti and Ca isotopic compositions and refractory trace element abundances in hibonites from CM and CV meteorites: Implications for early solar system processes. *Geochimica et Cosmochimica Acta*, 64(11), pp.1989-2005.

Saji, N.S., Wielandt, D., Holst, J.C. and Bizzarro, M., 2020. Solar system Nd isotope heterogeneity: Insights into nucleosynthetic components and protoplanetary disk evolution. *Geochimica et Cosmochimica Acta*, 281, pp.135-148.

Sanborn, M.E., Wimpenny, J., Williams, C.D., Yamakawa, A., Amelin, Y., Irving, A.J. and Yin, Q.Z., 2019. Carbonaceous achondrites Northwest Africa 6704/6693: Milestones for early Solar System chronology and genealogy. *Geochimica et Cosmochimica Acta*, 245, pp.577-596.

Schrader, D.L., Nagashima, K., Davidson, J., McCoy, T.J., Oglione, R.C. and Fu, R.R., 2020. Outward migration of chondrule fragments in the early Solar System: O-isotopic evidence for rocky material crossing the Jupiter Gap?. *Geochimica et Cosmochimica Acta*, 282, pp.133-155.

Schrader, D.L., Nagashima, K., Krot, A.N., Oglione, R.C., Yin, Q.Z., Amelin, Y., Stirling, C.H. and Kaltenbach, A., 2017. Distribution of ^{26}Al in the CR chondrite chondrule-forming region of the protoplanetary disk. *Geochimica et Cosmochimica Acta*, 201, pp.275-302.

Scott, E.R., Greenwood, R.C., Franchi, I.A. and Sanders, I.S., 2009. Oxygen isotopic constraints on the origin and parent bodies of eucrites, diogenites, and howardites. *Geochimica et Cosmochimica Acta*, 73(19), pp.5835-5853.

Scott, E.R. and Krot, A.N., 2005. Thermal processing of silicate dust in the solar nebula: clues from primitive chondrite matrices. *The Astrophysical Journal*, 623(1), p.571.

Scott, E.R.D. and Krot, A.N., 2014. Chondrites and their components. *Meteorites and cosmochemical processes*, 1, pp.65-137.

Shollenberger, Q.R., Wittke, A., Render, J., Mane, P., Schuth, S., Weyer, S., Gussone, N., Wadhwa, M. and Brennecka, G.A., 2019. Combined mass-dependent and nucleosynthetic isotope variations in refractory inclusions and their mineral separates to determine their original Fe isotope compositions. *Geochimica et cosmochimica acta*, 263, pp.215-234.

Simon, J.I. and DePaolo, D.J., 2010. Stable calcium isotopic composition of meteorites and rocky planets. *Earth and Planetary Science Letters*, 289(3-4), pp.457-466.

Simon, J.I., Jordan, M.K., Tappa, M.J., Schauble, E.A., Kohl, I.E. and Young, E.D., 2017. Calcium and titanium isotope fractionation in refractory inclusions: Tracers of condensation and inheritance in the early solar protoplanetary disk. *Earth and Planetary Science Letters*, 472, pp.277-288.

Singletary, S.J. and Grove, T.L., 2003. Early petrologic processes on the ureilite parent body. *Meteoritics & Planetary Science*, 38(1), pp.95-108.

Spitzer, F., Burkhardt, C., Budde, G., Kruijer, T.S., Morbidelli, A. and Kleine, T., 2020. Isotopic evolution of the inner solar system inferred from molybdenum isotopes in meteorites. *The Astrophysical Journal Letters*, 898(1), p.L2.

Stephan, T., Trappitsch, R., Davis, A.M., Pellin, M.J., Rost, D., Savina, M.R., Jadhav, M., Kelly, C.H., Gyngard, F., Hoppe, P. and Dauphas, N., 2018. Strontium and barium isotopes in presolar silicon carbide grains measured with CHILI—Two types of X grains. *Geochimica et Cosmochimica Acta*, 221, pp.109-126.

Sugiura, N. and Fujiya, W., 2014. Correlated accretion ages and $\epsilon^{54}\text{Cr}$ of meteorite parent bodies and the evolution of the solar nebula. *Meteoritics & Planetary Science*, 49(5), pp.772-787.

Takeda, H., 1987. Mineralogy of Antarctic ureilites and a working hypothesis for their origin and evolution. *Earth and Planetary Science Letters*, 81(4), pp.358-370.

Tang, H. and Dauphas, N., 2012. Abundance, distribution, and origin of ^{60}Fe in the solar protoplanetary disk. *Earth and Planetary Science Letters*, 359, pp.248-263.

Tang, H., Liu, M.C., McKeegan, K.D., Tissot, F.L. and Dauphas, N., 2017. In situ isotopic studies of the U-depleted Allende CAI Curious Marie: Pre-accretionary alteration and the co-existence of ^{26}Al and ^{36}Cl in the early solar nebula. *Geochimica et Cosmochimica Acta*, 207, pp.1-18.

Tenner, T.J., Nakashima, D., Ushikubo, T., Tomioka, N., Kimura, M., Weisberg, M.K. and Kita, N.T., 2019. Extended chondrule formation intervals in distinct physicochemical environments: Evidence from Al-Mg isotope systematics of CR chondrite chondrules with unaltered plagioclase. *Geochimica et cosmochimica acta*, 260, pp.133-160.

Tilhac, R., Morishita, T., Hanaue, N., Tamura, A. and Guotana, J.M., 2021. Systematic LREE enrichment of mantle harzburgites: The petrogenesis of San Carlos xenoliths revisited. *Lithos*, 396, p.106195.

Touboul, M., Sprung, P., Aciego, S.M., Bourdon, B. and Kleine, T., 2015. Hf-W chronology of the eucrite parent body. *Geochimica et Cosmochimica Acta*, 156, pp.106-121.

Travaglio, C., Rauscher, T., Heger, A., Pignatari, M. and West, C., 2018. Role of core-collapse supernovae in explaining solar system abundances of p nuclides. *The Astrophysical Journal*, 854(1), p.18.

Trinquier, A., Elliott, T., Ulfbeck, D., Coath, C., Krot, A.N. and Bizzarro, M., 2009. Origin of nucleosynthetic isotope heterogeneity in the solar protoplanetary disk. *Science*, 324(5925), pp.374-376.

Wadhwa, M., 2008. Redox conditions on small bodies, the Moon and Mars. *Reviews in Mineralogy and Geochemistry*, 68(1), pp.493-510.

Walsh, K.J., Morbidelli, A., Raymond, S.N., O'Brien, D.P. and Mandell, A.M., 2011. A low mass for Mars from Jupiter's early gas-driven migration. *Nature*, 475(7355), pp.206-209.

Wänke, H., Baddenhausen, H., Spettel, B., Teschke, F., Quijano-Rico, M., Dreibus, G. and Palme, H., 1972. The chemistry of Haverö ureilite. *Meteoritics*, 7(4), pp.579-590.

- Warren, P.H., 2011. Stable-isotopic anomalies and the accretionary assemblage of the Earth and Mars: A subordinate role for carbonaceous chondrites. *Earth and Planetary Science Letters*, 311(1-2), pp.93-100.
- Wasson, J.T., Isa, J. and Rubin, A.E., 2013. Compositional and petrographic similarities of CV and CK chondrites: A single group with variations in textures and volatile concentrations attributable to impact heating, crushing and oxidation. *Geochimica et Cosmochimica Acta*, 108, pp.45-62.
- Weber, P., Benítez-Llambay, P., Gressel, O., Krapp, L. and Pessah, M.E., 2018. Characterizing the variable dust permeability of planet-induced gaps. *The Astrophysical Journal*, 854(2), p.153.
- Wei, G., Ma, J., Liu, Y., Xie, L., Lu, W., Deng, W., Ren, Z., Zeng, T. and Yang, Y., 2013. Seasonal changes in the radiogenic and stable strontium isotopic composition of Xijiang River water: Implications for chemical weathering. *Chemical Geology*, 343, pp.67-75.
- Weisberg, M.K., McCoy, T.J. and Krot, A.N., 2006. Systematics and evaluation of meteorite classification. *Meteorites and the early solar system II*, 19, pp.19-52.
- Widanagamage, I.H., Griffith, E.M., Singer, D.M., Scher, H.D., Buckley, W.P. and Senko, J.M., 2015. Controls on stable Sr-isotope fractionation in continental barite. *Chemical Geology*, 411, pp.215-227.
- Williams, C.D., Sanborn, M.E., Defouilloy, C., Yin, Q.Z., Kita, N.T., Ebel, D.S., Yamakawa, A. and Yamashita, K., 2020. Chondrules reveal large-scale outward transport of inner Solar System materials in the protoplanetary disk. *Proceedings of the National Academy of Sciences*, 117(38), pp.23426-23435.
- Wilson, L. and Goodrich, C.A., 2016, March. The Formation Time and Thermal History of the Ureilite Parent Body. In 47th Annual Lunar and Planetary Science Conference (No. 1903, p. 1557).
- Young, E.D., Galy, A. and Nagahara, H., 2002. Kinetic and equilibrium mass-dependent isotope fractionation laws in nature and their geochemical and cosmochemical significance. *Geochimica et Cosmochimica Acta*, 66(6), pp.1095-1104.
- Yurimoto, H. and Wasson, J.T., 2002. Extremely rapid cooling of a carbonaceous-chondrite chondrule containing very ^{16}O -rich olivine and a ^{26}Mg -excess. *Geochimica et Cosmochimica Acta*, 66(24), pp.4355-4363.
- Yurimoto, H., Krot, A.N., Choi, B.G., Aléon, J., Kunihiro, T. and Brearley, A.J., 2008. Oxygen isotopes of chondritic components. *Reviews in mineralogy and geochemistry*, 68(1), pp.141-186.

Zhu, K., Moynier, F., Schiller, M., Becker, H., Barrat, J.A. and Bizzarro, M., 2021. Tracing the origin and core formation of the enstatite achondrite parent bodies using Cr isotopes. *Geochimica et Cosmochimica Acta*, 308, pp.256-272.

Zhu, K., Moynier, F., Schiller, M., Wielandt, D., Larsen, K.K., van Kooten, E.M., Barrat, J.A. and Bizzarro, M., 2020. Chromium isotopic constraints on the origin of the ureilite parent body. *The Astrophysical Journal*, 888(2), p.126.